REPORT DOCUMENTATION PAGE	AFRL-SR-AR-TR-04-

0090

The public reporting burden for this collection of information is estimated to average 1 hour per response, i gathering and maintaining the data needed, and completing and reviewing the collection of information. Send c information, including suggestions for reducing the burden, to Department of Defense, Washington Headquart 1215 Jefferson Davis Highway, Suite 1204, Arlington, VA 22202-4302. Respondents should be aware that penalty for failing to comply with a collection of information if it does not display a currently valid OMB control number.
PLEASE DO NOT RETURN YOUR FORM TO THE ABOVE ADDRESS.

1. REPORT DATE *(DD-MM-YYYY)* 06-10-2003	2. REPORT TYPE Final Technical Report	3. DATES COVERED *(From - To)* 1-7-2000 to 30-6-2003
4. TITLE AND SUBTITLE ACTIVE CONTROL OF INTEGRATED INLET/COMPRESSION SYSTEMS		5a. CONTRACT NUMBER F49620-00-C-0035
		5b. GRANT NUMBER
		5c. PROGRAM ELEMENT NUMBER
6. AUTHOR(S) Paduano, J. P. Principal Investigator Ahsun, U., Braddom, S., Brear, M.J., Bryanston-Cross, P.J., Colonius, T., Drela, M., Dunkley, P., Guenette, G.R., Luers, A.S., MacMartin, D.G., Mangus, J.F., McElwain, B.D., Merchant, A., Murray, R.M., Philhower, J.S., Skeen, A.J., Suzuki, T., Timmerman, B.H., Verma, A., Warfield, Z.		5d. PROJECT NUMBER
		5e. TASK NUMBER
		5f. WORK UNIT NUMBER
7. PERFORMING ORGANIZATION NAME(S) AND ADDRESS(ES) Massachusetts Institute of Technology Gas Turbine Laboratory, 31-213 77 Massachusetts Avenue Cambridge, MA 02139-4307		8. PERFORMING ORGANIZATION REPORT NUMBER
9. SPONSORING/MONITORING AGENCY NAME(S) AND ADDRESS(ES) AFOSR 4015 Wilson Boulevard, Room 713 Arlington, VA 22203-1954		10. SPONSOR/MONITOR'S ACRONYM(S)
		11. SPONSOR/MONITOR'S REPORT NUMBER(S)

12. DISTRIBUTION/AVAILABILITY STATEMENT

DISTRIBUTION STATEMENT "A"
APPROVED FOR PUBLIC RELEASE, DISTRIBUTION UNLIMITED
DARPA CASE# 44156, CLEARED DEC. 3, 2003

13. SUPPLEMENTARY NOTES

14. ABSTRACT

This report describes the work done during the period between July 1, 2000 and June 30, 2003 on two topics: active control of separation and distortion in high subsonic supersonic inlets, and active control of inlet unstart in supersonic inlets. The report is divided into a summary, which highlights the major accomplishments of the program, and a set of papers describing the technical details.

15. SUBJECT TERMS
active control, high subsonic supersonic inlets, transonic inlet flow control, supersonic unstart control

16. SECURITY CLASSIFICATION OF:			17. LIMITATION OF ABSTRACT	18. NUMBER OF PAGES	19a. NAME OF RESPONSIBLE PERSON James D. Paduano
a. REPORT	b. ABSTRACT	c. THIS PAGE		116	19b. TELEPHONE NUMBER *(Include area code)* 617-253-6047

Standard Form 298 (Rev. 8/98)
Prescribed by ANSI Std. Z39.18

20040213 031

Gas Turbine Laboratory
Department of Aeronautics and Astronautics
Massachusetts Institute of Technology
Cambridge, MA 02139

FINAL TECHNICAL REPORT

Contract #F49620-00-C-0035

entitled

ACTIVE CONTROL OF INTEGRATED INLET/COMPRESSION SYSTEMS

submitted to

AFOSR
4015 Wilson Boulevard
Room 713
Arlington, VA 22203-1954

Attn: Dr. Thomas J. Beutner

PRINCIPAL
INVESTIGATOR: James D. Paduano
                   Principal Research Engineer, Gas Turbine Laboratory
                   Department of Aeronautics & Astronautics
                   Tel: 617-253-6047; FAX: 617-253-6666
                   email: jdpaduan@mit.edu

PERIOD OF
INVESTIGATION: July 1, 2000 - June 30, 2003

October 6, 2003

Final Technical Report
ACTIVE CONTROL OF INTEGRATED INLET/COMPRESSION SYSTEMS

This report describes the work done during the period between July 1, 2000 and June 30, 2003 on two topics: active control of separation and distortion in high subsonic supersonic inlets, and active control of inlet unstart in supersonic inlets. The report is divided into a summary, which highlights the major accomplishments of the program, and a set of papers describing the technical details.

SUMMARY OF ACCOMPLISHMENTS

During the three-year period since program inception, the MIT / Caltech / Northrop Grumman / NASA Glenn team has achieved many substantial research and demonstration successes. Some of the highlights that we will discuss here are:

Transonic Inlet Flow Control:

1. First ever reattachment of a separating diffuser flow at Mach numbers exceeding 0.8, against a severe pressure gradient, using only 2% of the overall inlet flow;

2. Development and exposition of a seminal first-principles model of flow separation in a duct, validated in detail using DNS computations;

3. Experimental demonstration of feed-forward control of separation-induced unsteadiness, measured at its source and subsequently controlled at the Aerodynamic Interface Plane (AIP);

4. Development of the world's first ruggedized hot-film sensors, and validation of these against military specifications, to make sensing separation feasible in military inlets.

5. System-level elucidation of the impact of active inlet control on the weight and cost of future UCAV vehicles; and

6. Development and experimental validation of design rules for the geometry and placement of injectors for flow reattachment in diffusers.

7. Conceptualization and preliminary design of a full-scale (100 lb/sec) *combined inlet-compressor* national test facility, to be installed at NASA Glenn.

Supersonic Unstart Control:

1. Design of a near-isentropic supersonic inlet, optimized to balance boundary layer and shock losses and to take advantage of enhanced stability through active control;

2. Creation of a dynamic simulation and control environment that marries control system development tools with advanced computational tools;

3. Systematic design studies incorporating shock dynamics, atmospheric effects, inlet dynamics, and control system design to accurately determine the methods and benefits of active control; and

4. Design and partial construction of a supersonic test facility for demonstrating active inlet control, including:

   a. Inlet and flow path mechanical design, including traverse system to create area variation for restart and to set the operating point;

   b. Actuator design, including detailed supersonic bleed aerodynamics, prime movers, mechanical systems, and flow paths;

   c. Sensor choice and placement using dynamic simulation;

   d. Real-time fast-prototyping control development and implementation tools;

   e. Real-time shock-tracking visualization system;

   f. Supersonic test facility modifications, upgrades, instrumentation, and testing.

The remainder of this document is focused on providing enough detail to convince the reader that the above list does not represent idle claims, but rather real, substantial achievements with sufficient hardware, documentation, drawings, computer programs, design information, and engineering contacts to be repeated and/or carried forward. Eight research papers and several theses were written. No overlap of topics or content exists in the research papers, making them a concise review of the research results. These papers are attached and used as reference material for the rest of this report. Further results are provided in theses reference here and available on request.

TRANSONIC INLET FLOW CONTROL

1. Flow Reattachment Results

There have been and are various programs focused on flow control in diffusers with serpentine shapes. The distinguishing features of the experiments performed at MIT are the Mach number at the separation point (approximately 0.8; Mach numbers elsewhere in the duct exceed this); and the fact that due to the severe pressure gradient in the diffuser, the flow actually experiences separation, as evidenced by oil flow visualization experiments.

Flow reattachment itself has been the subject of numerous studies. However, the MIT experiment falls into a rarified class when one considers the Mach number of the 'free stream' flow (between .7 and .9), the 3D nature of the flow experiment (the inlet duct used was designed for Northrop's Air Force UCAV entry), and the severity of the pressure gradient. We chose to combine a 'Coanda' injector developed at NASA Glenn (based on previous joint research with MIT) with pulsed injection similar to that employed at UTRC for high Mach number airfoils. Flow reattachment results after optimization are shown in Figure 1; 2% of the main inlet flow recovered 60% of the loss introduced by the separation, and industrial distortion parameters such as DC60 and DCPC were substantially reduced (see report [1]). Our goal for continued research is to reduce the flow requirement to 1%, and to increase the energy efficiency of the actuation system. These two improvements will make inlet flow reattachment viable.

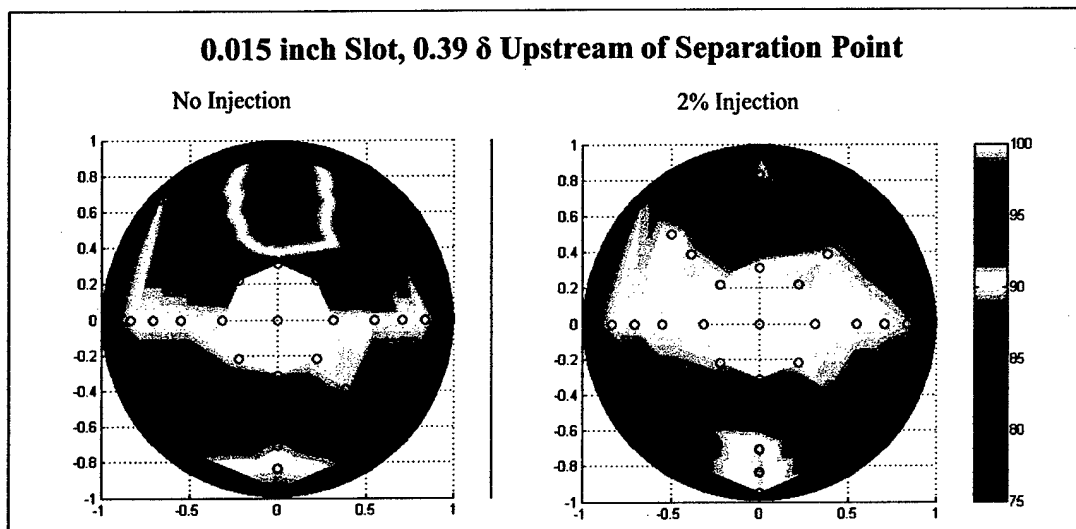**0.015 inch Slot, 0.39 δ Upstream of Separation Point**

Figure 1 – Flow reattachment results, after trade-study based improvement
of actuator geometry. Flow condition is near design,
actuation is on the top only.

2. First-Principles Model of Flow Separation

Together with experimental design and demonstration based on the state of the art
in experimental flow control, we undertook to develop models that would allow both
fundamental studies, and design optimization using computational tools, of methods for
flow reattachment through active control. Before the developments under this program,
very little first-principals studies had been done to understand the underlying mechanisms
that determine vortex shedding strength, frequency, and evolution due to flow separation,
and the effects of flow control on such parameters. Thus the models developed here are
truly seminal in both their scope and their implications.

A model based on vorticity conservation in a duct was developed and validated
against CFD. Stated simply, the thickened boundary layer upstream of a separation point
convects vorticity into the control volume of the duct. This vorticity builds up at the
separation point due to reverse flow conditions there, and must eventually shed to
conserve overall vorticity in the system. The natural size and frequency of vortex
shedding can be determined from first principles. In addition the effect of inducing
higher frequency vortex shedding through active control was studied. Results are
validated against a DNS simulation of vortex separation, and are given in the attached
paper [2].

3. Feed-Forward Control Of Separation-Induced Unsteadiness Using AIP Actuators

Our original plan for active control of inlets was to combine control of separation
with control of distortion and unsteadiness at the compressor face. This combined
control promised to be more effective, could utilize the same actuators at both points of

3

application (separation point and compressor face), and capitalized on the benefits of feedback and feed-forward control to reduce the airflow requirements of the overall system. Our first steps toward this integrated approach were to perform control studies at the AIP and the separation point separately, with a view toward combining them in our full-scale demonstration (which was, however, subsequently cancelled).

At the AIP, two major demonstrations were achieved. First, we showed that there is high correlation between (1) unsteadiness measured at the separation point using hot film sensors and (2) total pressure unsteady measurements at the AIP. This high correlation provides a mechanism for feed-forward control: if one measures events at or near the separation point, and feeds them forward to the AIP or compressor face, this advance information can be used to mitigate or cancel the incoming disturbances.

Such AIP pressure unsteadiness reduction was demonstrated in experiments conducted in the 1/6th scale transonic inlet facility operated in the MIT Gas Turbine Laboratory. Although this demonstration used AIP sensors directly instead of feed-forward information, it demonstrated the basic feasibility of the concept. The impact of the achieved levels of reduction on compressor stability and robustness was also studied and reported in the attached paper [3].

4. Development and Testing of Ruggedized Mil-Spec Hot-Film Sensors
In order to implement the feed-forward schemes described in the previous section in military vehicles, measurements must be available at the separation point in realistic flight environments. Military specifications exist for the percentage of flight hours that the engine must operate under specific abrasive sand conditions. Typical hot film sensors last a fraction of a second in the abrasion environments specified. Therefore there is a need for ruggedized hot-film sensors to provide feed-forward information in real environments.

Our solution to this problem is a hot-film sensor sputtered with Aluminum Oxide (Al_2O_3), whose hardness is lower only than that of diamond. The issues that have been addressed are the heat transfer properties of the hot-films substrate and the Al_2O_3 coating, the resulting sensitivity of the sensor, overall fabrication in a rugged package (see Figure 2), and testing in accordance with the Mil-Spec. Industrial grade quartz sand that met MIL-HBK-310 and MIL-STD-810F specifications was used. Large particles with sharp edges are required by these specifications, so the sand was not reused after each test. The test articles were secured flush to test surface with no obstruction to parallel flow of sand over the sensor. Sensor failure time was defined as the time during which the sensor resistance stayed within .05 ohm of it's pre-test value; failure always involved sudden large increases in resistance. Particle velocities were then computed and adjusted to match those in actual inlets. The sand concentrations used were much greater than operational concentrations to reduce the required test time. The sensors tested lasted an average of 570 equivalent flight hours, which is sufficient for real operations. Design details and further results of these tests are given in the Master's thesis of Captain Steven Braddom [4], who was supported by the Army to perform this research, and is now teaching at West Point.
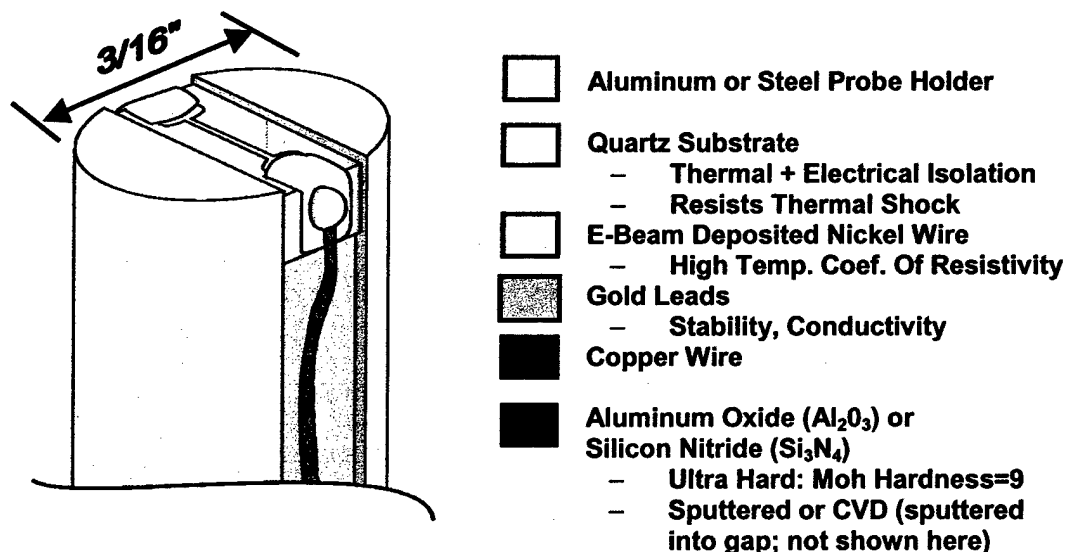
Aluminum or Steel Probe Holder

Quartz Substrate
- – Thermal + Electrical Isolation
- – Resists Thermal Shock

E-Beam Deposited Nickel Wire
- – High Temp. Coef. Of Resistivity

Gold Leads
- – Stability, Conductivity

Copper Wire

Aluminum Oxide (Al_2O_3) or Silicon Nitride (Si_3N_4)
- – Ultra Hard: Moh Hardness=9
- – Sputtered or CVD (sputtered into gap; not shown here)

Figure 2 – Ruggedized hot film sensor: designed, fabricated, and tested at MIT

5. System Studies of Impact on UCAV Cost and Weight

Northrop-Grumman provided technical support and consulting, extensive hardware for the inlet flow control experiments, and system-level studies of the impact of active flow control. The specific results of the system studies were reported in the Phase I report documentation, and in briefings to the program managers and technical monitors. A sizing study was conducted for a UCAV vehicle whose length was propulsion system-length driven, rather than driven by bomb bay size requirements. This vehicle was based on the Northrop-Grumman Air Force UCAV SEAD mission, using a New Generic Delta Planform with a smaller weapons bay than the original AF UCAV. A matrix of improvements was studied, which included inlet lengths (L/D 3.0, 2.5, 1.5), inlet recovery, and reduced required stall margin through active control.

The study concluded that a 13% TOGW reduction, and a 16% reduction in mission fuel could be gained through active control. These reductions would result in a life cycle cost reduction of over $200 M for the role the Air Force had defined for the UCAV at that time (i.e. in storage during much of their life). It was also concluded that the key to successful integration of active flow control in UCAVs is *careful integration* of the inlet and the compressor to take advantage of flow control. In other words, one cannot take advantage of flow control by simply adding it to an existing inlet; the inlet-compressor matching problem must be done with a view toward taking advantage of active control. This points to the importance of a national facility for studying inlet-compression systems in which active control has been incorporated. Such a facility does not currently exist.

5

6. Design Rules For The Injector Geometry And Placement

During the Phase II technical review, and in subsequent discussions with technical monitors, it was agreed that sub-scale experiments should be used not only to demonstrate the feasibility of flow reattachment in high-subsonic inlets, but also to establish design guidelines for the full-scale experiment. These design guidelines will help in determining the geometry, size and placement of injectors to be placed in full-scale devices.

Ten injector geometries were tested in the subscale experiment, forming a matrix of geometric design variations. The injectors were then tested over a range of inlet mass flows, as well as injector flows. The following design rules were established, and sufficiently reduce the risk to enable full scale testing [1, 5]:

(a)   The injector geometry should be tapering, and of sufficiently high radius of curvature that the flow does not choke internally. These guidelines have been verified in separate CFD studies at NASA Glenn.

(b)   To reduce the mass flow required by the injectors (i.e. increase the momentum ratio per unit mass flow), the injector slot width should be reduced to the point that the exit flow is near sonic at the maximum flow rate to be introduced. This value of slot width can be determined from the inlet conditions (pressure and temperature) and the desired mass flow from the injector. It appears from our tests that the maximum injection velocity must exceed the free stream velocity (in other words, it must be near sonic) for flow reattachment to be effective.

(c)   The angle between the injection slot and the separation point can be varied by up to 15 degrees without adversely impacting the performance of the injector. This means that the locations o f separation lines computed from CFD should be sufficiently accurate for placement of injectors.

(d)   The injectors should be placed about 0.5δ upstream of the separation point, where δ is the CFD-computed boundary layer thickness at the separation point.

(e)   Frequency of injection was found to improve the performance, up to the maximum available frequency of about 2-3 times the vortex shedding frequency.

Further detail on the results obtained and their interpretation is given in the attached report [1].

7. Full-scale Test Plan

A test plan, hardware layout, and assignation of primary responsibilities between Northrop-Grumman, NASA Glenn, and MIT, was developed for full-scale testing in a 100 lb/sec inlet/compressor facility. The planned test was to include a full scale serpentine inlet designed and built by Northrop-Grumman, an IAP rake, instrumentation,

data acquisition, and data reduction hardware and software to be provided by Northrop-Grumman, a full-scale transonic test compressor, compressor test facility, and design support to be supplied by NASA Glenn, and software and hardware (injectors, real-time computers, algorithms) for active control to be supplied by MIT. The facility planned would be unique in the world in its attempt to study *combined inlet-compressor* control, and to properly account for the interaction between these two components, which are usually treated separately by designers, during computational studies, and in validation experiments (even in aircraft procurement programs). The disparity between reality and the current AIP-driven approach to inlet-engine matching, and the associated out-dated requirements, often leads to inlet-engine matching problems late in aircraft procurement and re-engine programs.

SUPERSONIC UNSTART CONTROL

In parallel to the subsonic inlet studies described above, MIT launched a study to determine the potential benefits of active control of inlet unstart in supersonic inlets. The design regime for the inlets of interest was 60,000 ft cruise at Mach 2.2, consistent with Quiet Supersonic Platform (QSP) design concepts.

After an initial study during the Phase I effort (Fall 2000), and after one year of the Phase II effort concentrated primarily on subsonic inlet control, MIT was directed to begin more detailed study of the unstart control concept. This research effort continued for about one year before research funding was cut. As such, the results here are somewhat less complete than the subsonic results, which continued throughout the program (through students finishing theses, etc.). Nevertheless, substantial progress toward demonstration of inlet unstart control was made, sufficient to allow follow-on work at relatively low cost.

1. Design of a Near-Isentropic Supersonic Inlet

Tools for design of supersonic diffusion pathways were developed in the context of the aspirated compressor program. These tools are well suited to supersonic inlet design, because they accurately account for boundary layer growth, while capturing the shock behavior in a computationally efficient manner. For supersonic inlets, the challenge is to keep the length (i.e. the weight) of the inlet as low as possible, while diffusing slowly enough that the boundary layer remains healthy. If the boundary layer losses are too high, the benefits of near-isentropic compression (weak shocks) will be negligible. Likewise, if the bleed requirements to maintain near-isentropic compression are too high, the advantages will be lost. Design to balance these complex trades requires an efficient design tool that allows multiple design trials to be attempted in a short time period.

By reducing the requirement for robustness to atmospheric and compressor-born disturbances, we remove one of the many constraints on inlet design. With this constraint removed, a reasonable length inlet can be designed that has 96% pressure recovery, using two-dimensional bleeds of about 4% [6]. The boundary layer in the inlet is extremely thin compared to conventional inlets, so that boundary layer stability is not an issue. This is because weakening the shocks reduces some of the 'stress' on the boundary layers; less boundary layer growth occurs across a weak shock.

The result of this part of the research is an inlet that has very good boundary layer properties, low losses, and moderate bleed requirements. However, this inlet design can only be realized in practice through the introduction of active control to prevent unstart. Unstart control was the focus of the rest of the research program, as described below.

2. Integrated Dynamic Simulation And Control Environment

MIT's tools for efficient inlet design also provided the infrastructure for unsteady simulation of the inlet with disturbances and control. In [6], an efficient unsteady Euler
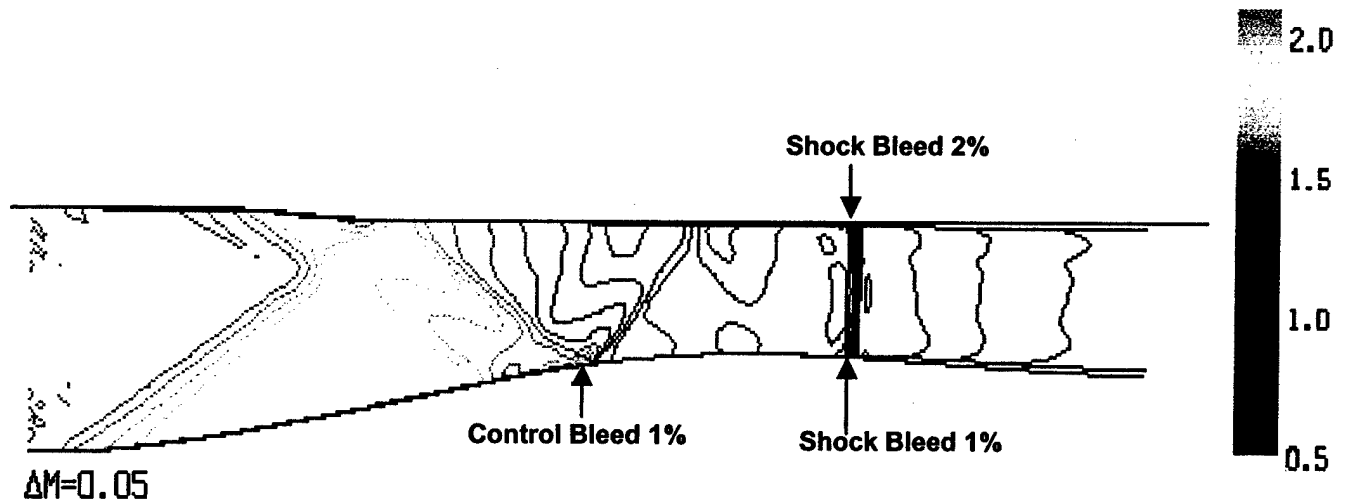
8 ·

Figure 3 – Near-isentropic supersonic inlet design. Note incorporation of bleeds and boundary layers in the design, and the very weak shock strengths throughout.

simulation of inlets is described. This unique tool allows a control engineer to interact with a CFD inlet from Simulink, which is the state-of-the-art in nonlinear simulation and control system design. Using this environment, we were able to perform system identification studies, actuator placement analysis, low order model development and validation, and control system design and verification.

3. Atmospheric Flight Control System Design Studies

Systematic design studies incorporating shock dynamics, atmospheric effects, inlet dynamics, and control system design to accurately determine the methods and benefits of active control were undertaken using the simulation described in the previous section. Reference [6] (attached) provides the details; here some of the main results are briefly described.

One important early realization was that if the Mach number at the throat of a supersonic inlet drops below one, a new shock can form at the throat and blow out the front of the inlet. Thus stabilization of the shock alone is not sufficient to insure good unstart properties; in this scenario the main shock does not move significantly until the system has unstarted. Based on this realization, a control system architecture incorporating feedforward control was developed; essentially disturbances measured upstream of the throat are counteracted by disturbances launched upstream of the inlet throat.

For shock position maintenance, a new low-order nonlinear model was developed. This model is an extension of classical results in the area of transmission and reflection of modes across shock waves. The model elucidates important properties of shocks from the perspective of dynamics and control. Reference [7] (attached) provides details of this model.

9

Once a control system architecture was developed and a design was implemented into the computational model, a careful consideration of the atmospheric gust effects was undertaken. The control system design study and atmospheric results are summarized in [6] (attached) and detailed in [8]. Significant reduction in the response to gusts was demonstrated.

4. Experimental System Design and Partial Construction

Testing of the inlet control design concept requires a test facility that is unique in several ways. Obviously, high-response actuation and sensing, which is usually not present in inlets, must be introduced into the test article. Because the required actuation bandwidth goes up as the test article size is reduced, the test article must be sufficiently large. In order to appropriately test the control system, exogenous disturbances must be generated; in other words pseudo-gusts must be generated in the test facility. As with any inlet test facility, a mechanism for starting and restarting the inlet must be put into place; in our case the system must be suitable for many unstarts, since testing near the stability boundary is the goal. Finally, high-response flow visualization is desirable to provide a diagnostic of the unsteady behavior.

Design and initial construction of the test facility was completed before the program was terminated. Figures 4 and 5 shows a cross-section of the test article in place and associated CFD through-flow; Figure 6 shows the traverse system design; this design allows both gross changes in throat area (for restarting an unstarted inlet) and fine control over operating condition through a piezo-stack actuated nozzle plate. This nozzle plate also serves as a high-frequency downstream disturbance generator. Besides overall mechanical design of the inlet flow path and traverse system, the following items were also accomplished

- Supersonic test facility modifications, upgrades, instrumentation, and testing. The MIT 8" by 8" test facility was modified for testing inlets by introducing a higher capacity heat exchanger and instrumentation to monitor flow loop operation. The optical windows were enlarged to allow the whole test article to be views, and the nozzle blocks were moved to a new location to lengthen the test section.

- Since upstream bleeds were chosen for the feed-forward actuation, a supersonic bleed slot was designed. This is essentially another supersonic diffuser design, because the slot is must efficiently decelerate the flow. The challenge is to minimize the shock losses, appropriately account for a boundary layer that is thick relative to the diffuser, and to provide high frequency modulation of the quantity of bleed. Figure 5 shows the CFD results for the bleed slot; the lower profile of this picture is the moving portion of the actuator.

- Matlab/Simulink's facility for generating real-time implementations of control systems designed in Simulink was chosen for the control system implementation. A so-called 'XPC' implementation of the control laws described in the previous section was implemented and tested, verifying that the control laws could be implemented at a sampling rate of 250Hz.
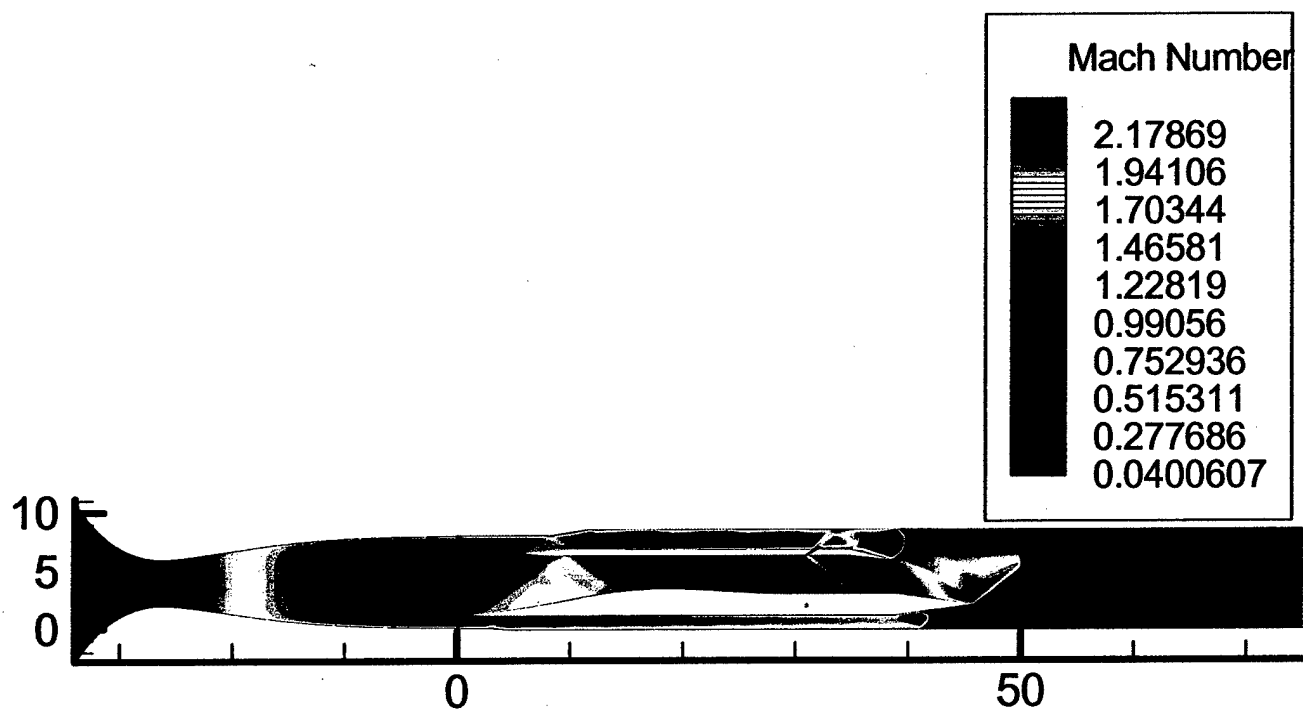
10

Figure 4 – 2D RANS simulations verifying that supersonic through-flow could be achieved for the planned test article installation

- Through collaboration with flow visualization experts at Warwick University, a real-time shock-tracking capability was incorporated into the facility. To create this capability, a shadowgraph system was set up and focused onto a CCD camera array. The image was then transmitted to a host computer via FireWire and processed in real time using custom image processing software. The shock is detected and tracked in real time at a frequency of over 900 Hz. The output of the shock tracking software can be fed back digitally or through an analog output. In addition, triggered data acquisition and real-time shadowgraph monitoring were built into the software.

The shock tracking was tested and verified using a pulsed injector to generate a moving shock. See Figure 7; a description of the optical system and the results of the validation tests are given in Reference [9] (attached).

11

2.50e+00
2.38e+00
2.25e+00
2.12e+00
2.00e+00
1.88e+00
1.75e+00
1.62e+00
1.50e+00
1.38e+00
1.25e+00
1.12e+00
1.00e+00
8.75e-01
7.50e-01
6.25e-01
5.00e-01
3.75e-01
2.50e-01
1.25e-01
0.00e+00
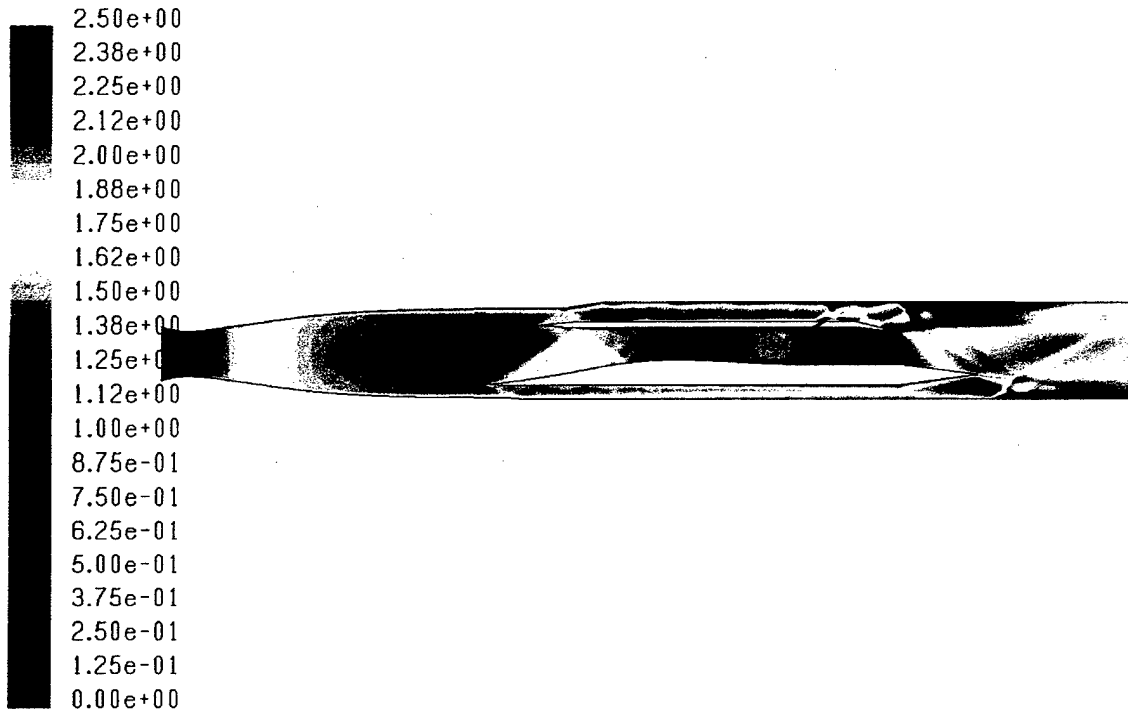
Figure 5 – RANS CFD analysis of upper plate bleed ports, verifying flow conditions both in the test article at design, and in the bypass ducts with bleeds
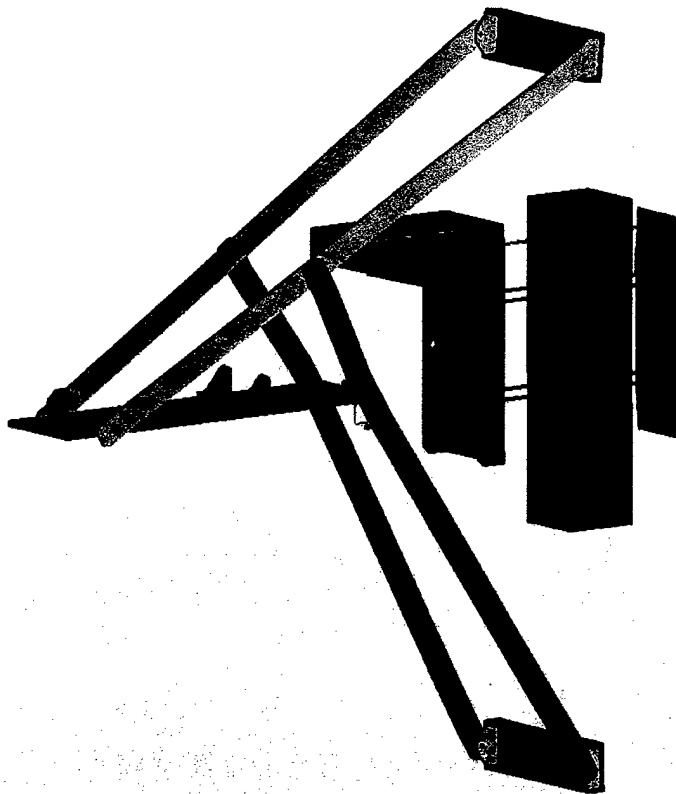
Figure 6 – Top Plate Traverser Mechanism. Blue box and upper plate (right) are inside test section; not shown on left are servos (screwjack and piezos, already purchased).
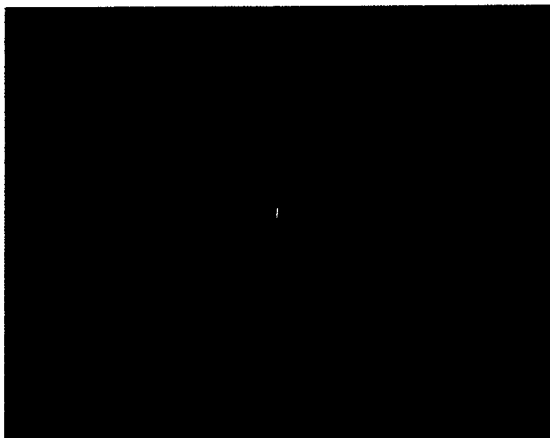
Figure 12: Spatial-temporal streak view of unstable oscillation
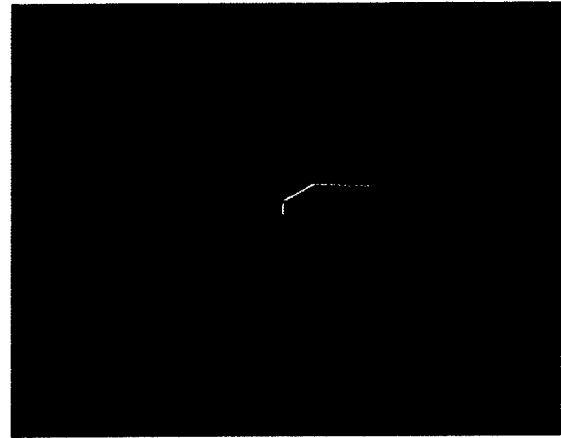
Figure 13: Still view of oscillating shock

Running the camera in tracking mode calculates the horizontal displacement of one part of the shock approximately 980 times a second. Figure 14 shows a typical position plot for a regularly oscillating shock, where the position was measured along the central axis of the nozzle. The amplitude of oscillation equates to 16 pixels, which is just under 2mm in real terms, and the FFT analysis presented in Figure 15 shows that it has a frequency of 76Hz.
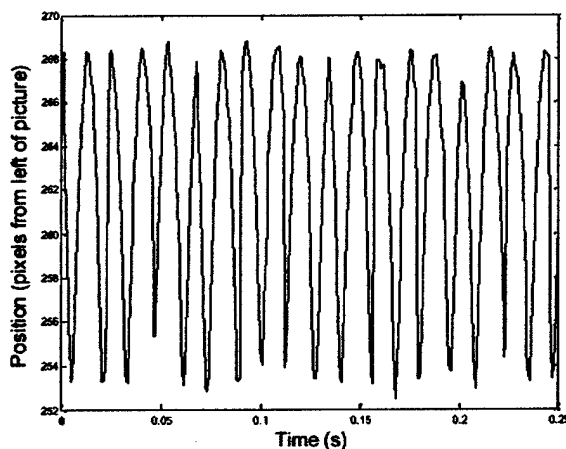
Figure 14: Position plot of oscillating shock wave
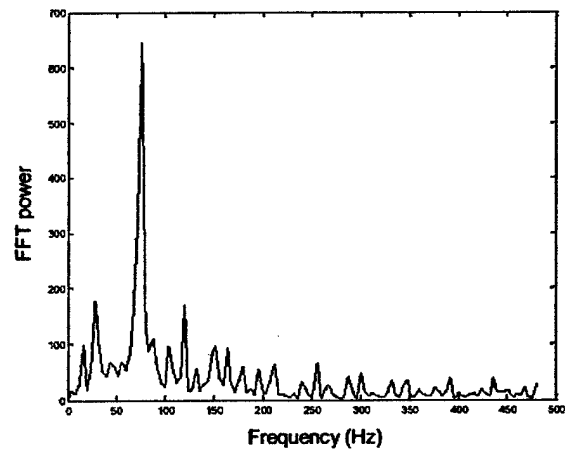
Figure 15: FFT of shock oscillation

Figure 7 – Excerpt from Reference [9] ,showing typical shock tracking results.

13

provided much of the equipment and instrumentation used for the subsonic inlet flow control studies; their generous support and valuable collaboration is very much appreciated.

DISCLAIMER

The views expressed in this document are solely those of the authors; they do not represent those of DARPA or AFOSR, who do not endorse them.

ATTACHED REPORTS AND REFERENCES

1. Luers, A. S., McElwain B. D., and Paduano, J. D., "Pulsed Injection Flow Control in a Separating Serpentine Diffuser," submitted to AIAA Journal. **(attached)**

2. Suzuki, T., and Colonius, T., "Large-Scale Unsteadiness In A Two-Dimensional Diffuser: Numerical Study Toward Active Separation Control," AIAA 2003-1138 41st Aerospace Sciences Meeting and Exhibit, Reno, January 6-9 2003. Fluid Dynamics Technical Committee Best Paper Award. **(attached)**

3. Warfield, Z., Paduano, J. D., and MacMartin, D. G., "Stall Margin Improvement Using Feedback Control To Mitigate Inlet Distortion Unsteadiness," Unpublished *(not cleared for release by DARPA)*; some results were presented at the AIAA Flow Control Conference, June 2002. **(attached)**

4. Braddom, Steve, "Design And Characterization Of Robust Hot Film Sensors For Tactical Aircraft Inlets" M.S. Thesis, Department of Aeronautics and Astronautics, June 2002. **(available on request)**

5. Luers, Andrew, "Flow Control Techniques In A Separating Serpentine Inlet: An Enabling Technology To Increase The Military Viability Of Unmanned Air Vehicles," M.S. Thesis, Department of Aeronautics and Astronautics, June 2003.. **(available on request)**

6. Ahsun, U., Merchant, A., Paduano, J.D., and Drela, M., "Design of an Actively Stabilized Near-Supersonic Inlet," AIAA Paper 2003-4096, 16th AIAA Computational Fluid Dynamics Conference, Orlando, June 23-26, 2003. **(attached)**

7. Ahsun, U., M.S. Thesis in progress, Department of Aeronautics and Astronautics, December 2003. **(preprint available on request)**

8. MacMartin, D.G., "Dynamics and Control of Shock Motion in a Near-Isentropic Inlet", AIAA 2002-2943, AIAA Flow Control Conference, St. Louis, June 2002. In press, *AIAA J. Aircraft*, (tentatively Nov.-Dec) 2003. **(attached)**

14

9. P.J. Bryanston-Cross, A.J. Skeen, B.H. Timmerman, P. Dunkley, J. Paduano, G.R. Guenette, Jr., "Low-cost digital visualization and high-speed tracking of supersonic shockwaves," SPIE Paper no: 5191-45, International Symposium on Optical Science and Technology: Conference on Optical Diagnostics for Fluids, Solids and Combustion, San Diego, August 3-8, 2003. **(attached)**

10. MacMartin, D.G., and Verma, A. and Murray, R.M. and Paduano, J.D., "Active Control of Integrated Inlet/Compression Systems: Initial Results", *ASME Fluids Engineering Division Summer Meeting,* New Orleans, May 2001. **(attached)**

11. Brear, M. J., Warfield, Z., Mangus, J. F., Braddom, S., Paduano, J. D., Philhower, J. S., "Flow Separation Within The Engine Inlet Of An Uninhabited Combat Air Vehicle (UCAV)", FEDSM2003-45579, Proceedings of FEDSM'03 4TH ASME/JSME Joint Fluids Engineering Conference Honolulu, Hawaii, USA, July 6– 11, 2003. **(attached)**

Pulsed Injection Flow Control in a Separating Serpentine Diffuser

Andrew S. Luers   Brian D. McElwain   James D. Paduano

Aeronautics and Astronautics
MIT

Abstract

A series of high subsonic flow experiments (Mach number ~0.65) were conducted in a serpentine diffuser in which flow separation occurs. Periodic injection was introduced near the separation point, using various Coanda-type injector geometries and various injection mass flows, to improve pressure recovery and mitigate distortion and unsteadiness at the Aerodynamic Interface Plane (AIP). Data was collected by way of 80 equal-area total pressure measurements covering the AIP as well as by static pressure taps placed at various locations around the diffuser. Results include total pressure maps, upper-quadrant pressure recovery, DC(60), and DPCP as functions of the governing parameters. For an injection mass flow of 2% of the inlet mass flow, the best injection configuration to date increases total pressure recovery in the upper quadrant (where separation effects are severe) from 93% to 97% (a 60% reduction in the losses) and significantly reduces DC(60) and DPCP over a range of mass flow conditions.

Introduction

New demands are being placed on military aircraft inlet designs, which require that they be S-shaped and have much shorter length-to-diameter ratios than ever before. These demands are typically in conflict with engine performance. If the inlet diffuses the flow too aggressively or the ductwork turns too sharply, flow separation will occur and result in pressure loss, distortion and unsteadiness at the compressor face. This in turn will result in decreased efficiency, reduced compressor stability, and reduced stall and surge margins. The trade off between inlet geometry and system performance is accentuated in unmanned combat air vehicles (UCAVs). The propulsion system length often sets the overall length of these vehicles, so there is a strong desire to reduce aircraft length (and thus cost) by making shorter more aggressive

1

inlets, while at the same time maintaining system performance. This obviously puts news demands on designers.

Flow control will likely be a facilitator for achieving more aggressive inlet designs while maintaining performance. This paper explores one component of an integrated inlet-compressor flow control system, namely periodic injection of mass flow near the flow separation point in the inlet. Such injection has the potential to mitigate flow separation and thereby improve pressure recovery, reduce distortion, and reduce unsteadiness at the compressor face.

A scaled Northrop-Grumman UCAV inlet design was used as the test article for these studies. It is a top-mounted, serpentine inlet with varying cross-sectional geometry. At moderate mass flows, separation occurs off the top surface and, to a lesser degree, the bottom surface. Pulsed injection was introduced near the point of flow separation through Coanda-type injectors, which take advantage of the Coanda effect to achieve near-wall injection. A parametric study was performed to find the geometric design parameters that improve flow characteristics while using as little injection mass flow as possible. The parameters studied were the unsteady momentum coefficient C_μ, the steady C_μ (the ratio of average injection momentum to inlet momentum), injector slot location relative to the separation point, and injection angle relative to the free-stream flow direction.

2

Nomenclature

AIP	Aerodynamic Interface Plane
C_μ	Unsteady momentum coefficient
Steady C_μ	Steady momentum coefficient
DC(60)	Circumferential distortion parameter
δ	Boundary-layer thickness
DPCP	Circumferential distortion intensity
h	Injection slot width
SLA	Stereolithography
UCAV	Unmanned Combat Air Vehicle
VG	Vortex Generator

Previous Work

Control of separation and secondary flows has been addressed in many studies. Most work has been conducted on external flows with low Mach numbers. Some of the primary methods employed have consisted of the use of steady and periodic injection of mass flow, acoustic pulses, and synthetic jets. In a review of some of these studies, Grenblatt and Wygnanski concluded that periodic excitation performed better than steady injection, allowing control with much lower input energy [1]. Synthetic jets (devices that alternate between injection and suction, with zero net mass flux) in particular have shown great potential. Amitay *et. al* hypothesized that periodic excitation can improve the separation behavior of serpentine inlets at high subsonic conditions as well [2]. While synthetic jets have been shown to be successful in low speed flows, there are few studies to indicate whether they can provide the

3

necessary control authority for high subsonic flows. An outstanding issue is the fact that for such injectors operating in high speed flows, the injected momentum is typically lower than the free stream momentum during most of the duty cycle [3].

Periodic excitation about a non-zero mean injection level, on the other hand, has an additional degree of freedom that allows mean momentum to be relatively high compared to the free stream. Recently, it was shown that periodic excitation via pulsed injection (with relatively high mean momentum) can reattach the flow and improve downstream pressure recovery for a high subsonic flow in a 2-D diffuser [3]. In this study mass flow was periodically injected at the separation point through a Coanda injector. The same method of separation control has been employed in the study presented here.

Alternate approaches to improving the flow quality in serpentine diffusers have concentrated on preventing 'lift-off' of longitudinal vortices. Vane and air-jet vortex generators (VGs) have been used to generate vortices that create boundary layer flows opposing those generated by the geometrically-induced secondary flow [4,5]. These approaches address inlets that are dominated by secondary flow vortex lift-off, rather than inlets with separation events induced by strong adverse pressure gradients.

The case studied in this paper is one of a gross separation in a high-subsonic diffusing inlet with variable geometry [6]. The goal is to improve pressure recovery and reduce distortion and unsteadiness by way of preventing the separation. This is done by periodically introducing mass flow from an axial (as opposed to cross-flow, often used for VGs) jet near the separation point and tangential to the inlet surface. This configuration and its intent is akin to leading-edge separation prevention such as that studied by [11].

4

Inlet Flow Physics

The inlet-diffuser that serves as the test article in this paper has varying geometry and a serpentine curvature. Because of the severity of the internal curvature, an adverse pressure gradient causes the flow to separate from the surface of the diffuser at some mass flow conditions. In previous studies the details of the structure of this separation were examined and are documented by Brear *et. al* [6].

Brear *et. al* clearly show how the CFD predictions shown in Figure 1, together with oil-flow visualization results in the experimental apparatus, elucidate the physical mechanism of the separation. Two large counter-rotating vortices form at the top of inlet in the reverse-flow region downstream of the separation line. The 3D morphology of the separated region (in contrast to typical 'separation bubbles' one sees in 2D diffusers) generates a longitudinal vortex pair that extends downstream, and is subsequently observed in the upper quadrant of the AIP. Brear *et. al* conclude that the separation results from a strong adverse pressure gradient, appears to be strongly unsteady, and may respond to free stream disturbances. The longitudinal vortices result from flow separation and are largely responsible for the poor pressure recovery and increased distortion and unsteadiness measured at the AIP. These vortices periodically form, shed, and convect downstream to the AIP. The characteristic frequency of this shedding has been studied in greater detail by Braddom [7] who has shown the shedding frequency to range from 650Hz to 900Hz for mass flows of 2.9-3.3 lb/s (these are the cruise mass flow conditions for the 1/6th scale inlet).

Although the Mach numbers in our experiments were similar to the design flight conditions, Reynolds numbers were not. However, Brear *et al.* argue that the effects seen in this inlet are not likely to be strongly dependent on Reynolds number. For instance, as mass flow

through the inlet is increased, the pressure recovery at the AIP is found to decrease. If Reynolds number effects dominated, we would expect the opposite trend: Reynolds number increases with increased mass flow, which typically results in reduced boundary layer thickness. This in turn would result in an increase, not a decrease, in pressure recovery. Thus we expect the trends and effects measured in the inlet to be consistent with the full-scale system. For a more detailed account of the inlet flow physics see references [6], [8] and [9].

Experimental Setup

All experiments were performed at the Gas Turbine Laboratory at MIT. The experimental test setup consisted of a varying-geometry serpentine diffuser, a De Laval air compressor to draw air through the diffuser, a mass flow throttle plug to control mass flow, an actuation system to introduce pulsed injection near the flow separation point, a data acquisition system, and nine interchangeable Coanda injectors of various widths, positions, and angles, through which the injection flow was introduced into the diffuser.

The inlet used in these studies is part of a Northrop-Grumman 1/6th scale UCAV model, shown in Figure 2. It was formed using a rapid prototyping stereolithography (SLA) procedure in which the parts were grown layer by layer in a resin bath. The inlet lip has been replaced with a bellmouth to condition the flow and simulate cruise flight conditions. Mass flow is delivered through the diffuser by way of an open system driven by a ~1 MW De Laval air compressor. The compressor inlet is fed by a 24-inch diameter pipe to which is mated a mass flow throttle plug. The throttle plug, which is used to set the mass flow through the diffuser, has a conical inner shape and a movable center bullet that is controlled by a stepper motor (see Figure 3). The throttle plug chokes the flow and the movable bullet sets the size of the choking area.

Actuation

The actuation system used for these experiments consisted of a rotary valve, capable of frequencies of over 2.5 kHz, a 100psi compressor, and various injectors through which the air was ultimately passed into the diffuser. A pressure regulator and flow meter with thermocouple were used to calculate the injection mass flow.

Nine different interchangeable Coanda injector blocks were designed and tested. The injectors were also made using SLA. Designing the injectors as removable blocks allowed for versatility in injector geometry and injector exit location relative to the separation line. The actuator sits on, and seals to, the injector and the injector sits flush with the diffuser's inner surface. Flow was introduced through the injectors in the down stream direction, tangential to the diffuser wall. The injectors were designed to enable examination of the effects of changes to three different parameters: slot width, slot position, and slot angle. Note that injection was only introduced on the top side of the inlet, where separation was most severe.

Table 1 describes each of the nine injectors. Slot angle is referenced to the spanwise direction, e.g. a slot angle of zero is perpendicular to the free stream. All slots were a total of 4 inches long; in the case of angled slots, a symmetric arrangement of two 2" slots was used; the slots were canted away from each other in a 'Chevron' configuration (see Figure 4).

Table 1 – Geometry of the Eight Injector Blocks Used in the Parametric Study

Injector	Slot Width (h)	Slot Position	Slot Angle
One	0.032"	@ Separation Line	0
Two	0.02"	@ Separation Line	0
Three	0.01"	@ Separation Line	0
Four	0.01"	0.19δ Upstream of Separation	0
Five	0.01"	0.58δ Upstream of Separation	0
Six	0.01"	0.19δ Upstream of Separation	6°
Seven	0.01"	0.19δ Upstream of Separation	12°
Eight	0.015"	0.39δ Upstream of Separation	0

Data Acquisition

Steady-state total pressure profiles were obtained with a rake consisting of 40 probes, mounted along eight radial rakes, each with five probes, positioned every 45°, complying with ARP 1420 guidelines [10]. The can was rotated 22.5 degrees during testing so that 80 points of data were taken, providing a finer resolution of the AIP. The probes were connected via flexible tubing to a 48 port Scanivalve (Scanco No.SSS 48CMK3) which was controlled by a Scanivalve Digital Interface Unit (Model No. SDIU MK5). The Scanivalve houses a 100-psid transducer. Additionally, static pressure taps were placed around the inlet entrance and around the AIP. These were also connected to the Scanivalve. A National Instruments LabView VI was created to collect data.

Baseline Results

Figure 5 shows the total pressure profile at the AIP for an inlet mass flow of 3.1 lb/s (corresponding to cruise conditions). As can be seen from the figure, there is a large distorted region in the top quadrant and a smaller distortion at the bottom. The area averaged total pressure recovery is 95.6%, where average pressure recovery is the measured total pressure at each probe location divided by the upstream total pressure averaged across all 80 probes.

$$\text{Pressure Recovery} = \frac{1}{n} \sum \frac{P_t}{P_\infty} \tag{1}$$

The area averaged total pressure recovery in the top quadrant, which contains the large distorted region, is 93.25%. Because flow control in the bottom of the inlet was not considered in the present studies, the pressure recoveries in this paper will be reported for the upper quadrant.

The exit slot for Injector One was located right at the point of flow separation, as determined by oil flow visualization results [6]. The slot was 0.032 inches wide and injected

8

flow parallel to the free stream flow direction. Pulsed air was introduced through the injector at a frequency of 2 kHz. This frequency was found to yield the best results for a broad range of geometric conditions, so it was not varied during the parametric study. Pressure recovery at the AIP was measured for increasing injection mass flows and upper-quadrant area averaged pressure recovery is plotted against injected mass flow in Figure 6.

Figure 6 shows that periodic separation point injection does improve pressure recovery, verifying the predictions of Amitay *et al.* and the 2-D studies of McElwain. However, the improvement obtained for low mass flows (1 or 2 percent) is relatively poor; improving this performance is the motivation for the parametric study presented next.

Parametric Study

A parametric study of injection designs was performed to explore the effects of (1) steady C_μ; (2) injection angle with respect to the free stream flow direction; and (3) stream-wise injection position, on the following performance parameters: pressure recovery, distortion, and unsteadiness. Pressure recovery was the initial metric by which the various injectors were judged, but as the ideal values of these parameters where determined, the improvements in inlet distortion, DC(60) and DPCP, were also studied. The frequency of injection was maintained at 2 kHz for all configurations.

Effect of Steady C_μ

The first parameter studied was steady C_μ. Steady C_μ is defined as the ratio of average injection momentum to the momentum of the separated region,

$$\text{Steady } C_\mu = \frac{\rho_i h l \bar{u}^2}{\rho A_s U_\infty^2} \qquad (2)$$

9

where ρ_i and ρ are the densities of the injected and free stream air respectively, h and l are the width and spanwise length of the injection slot, A_s is the area of the separated region, $\hat{u}$ is the mean injection velocity, and U_∞ is the freestream velocity.

For Injector One, steady C_μ is calculated and plotted against pressure recovery in Figure 7. From the figure it is clear that pressure recovery increases as the injection momentum increases. It is of course desirable to increase pressure recovery with minimum mass flow for the practical reason that in implementation this mass flow will likely be bled off of the engine. Therefore, to increase the injection momentum for lower mass flows, the injection slot width h was reduced. Since steady C_μ decreases linearly with h but increases as the square of $\hat{u}$ (equation 2), steady C_μ should increase with decreasing h, peaking at roughly the value of h that results in sonic flow at the jet exit for the target mass flow (here, 1-2% of the inlet flow).

Three different slot widths were designed and tested; see Injectors One, Two, and Three in Table 1. All other variables were held constant; all injection was introduced at the separation point, and parallel to the free stream flow through the inlet (zero slot angle). Data was taken for two different inlet mass flows (2.9 lb/s and 3.1 lb/s) and for a range of injection mass flows (from 1/2 % to 4% of inlet mass flow). Pressure recovery was calculated for each probe in the upper quadrant and then area averaged.

Figure 8 is a graph of the change in pressure recovery versus slot width for injection mass flows of 1% and 2% of total inlet mass flow, for both inlet mass flows. From this figure it can be seen that, of the three injectors, the 0.02-inch injector had the greatest effect on pressure recovery. A slot width of 0.01 inches provides some improvement over the 0.032-inch slot, however this improvement in pressure recovery was not as great as that from the 0.02-inch injector. From these trends, it appears that the optimum slot width is between 0.01 and 0.02

inches. Unfortunately because these slot widths are so small we were unable to measure the injection velocity and density, and are thus unable to provide reliable estimates for steady C_μ. Our conjecture is that steady C_μ rises as slot width decreases, up to a point at which boundary layer and perhaps shock losses begin to dominate the effect of accelerating the flow. At this point further reduction in the slot width does not increase steady C_μ, so the pressure recovery improvement levels off.

Effect of Streamwise Slot Position

The next parameter studied was slot position relative to the separation point. Previous studies have indicated that injecting upstream of the separation line may be superior to injecting at or downstream of the separation point. Thus, injectors Three, Four and Five were designed to determine the optimum position for injection. Again, all other variables were held constant; the width of the injection slot was 0.01 inches for each block and all the injectors ejected flow parallel to the inlet free stream flow.

The appropriate length scale by which to non-dimensionalize the slot position in this inlet is not obvious. Several length scales were considered, including the size of the separation region and the boundary layer thickness at the point of separation. It was decided that the boundary layer thickness is the most well-defined quantity and appropriately emphasizes the viscous effects on injector placement.

The boundary layer thickness at the separation point in the full-scale UCAV inlet was calculated by Northrop-Grumman using a 3D lifting-surface inflow correction method (see Figure 9) [12]. The velocity profiles of the model and full-scale inlet are assumed to be the same. The separation point in the full-scale inlet is at about 209 inches along the duct; thus from Figure 9, the boundary layer thickness δ is ~1.9 inches. To scale this value to our sub-scale

11

experiment, δ was first assumed to scale approximately like the Blasius solution for compressible flows over a flat plate, that is,

$$\delta_{full-scale} = \frac{0.37x}{Re_{full-scale}^{1/5}} \qquad (3)$$

The full-scale value was then adjusted to account for the differences in size and Reynolds number of the 1/6th scale inlet by dividing it by 6 and multiplying by the ratio of the full-scale Reynolds number at the separation point to the 1/6th scale Reynolds number at the separation point. Thus for the 1/6th scale inlet the boundary layer thickness was estimated as follows,

$$\delta_{1/6-scale} \cong \frac{\delta_{full-scale}}{6} \cdot \frac{Re_{full-scale}^{1/5}}{Re_{1/6-scale}^{1/5}} \qquad (4)$$

The full-scale Reynolds number at the separation point was calculated to be 6.45×10^7, and the Reynolds number in the 1/6th scale inlet was calculated to be 5.55×10^6. Thus the boundary layer in the 1/6th scale inlet was calculated to be ~0.517 inches. This number was used to non-dimensionalize the slot position.

Data was again collected for inlet mass flows of 2.9 lb/s and 3.1 lb/s. Upper quadrant pressure recovery was calculated and the change in pressure recovery vs. slot position is plotted in Figure 10. This figure shows that injecting upstream of the separation line substantially improves pressure recovery over injecting at the separation line. Injecting 2% inlet flow at the separation line improves pressure recovery by just over 1% for an inlet flow of 3.1 lb/s and by about 2% for an inlet flow of 2.9 lb/s. By comparison, injecting 2% inlet flow 0.19δ upstream improves pressure recovery by over 3% for an inlet flow of 3.1 lb/s and by over 3.5% for an inlet flow of 2.9 lb/s. In addition, the largest gains in pressure recovery from injecting upstream of the separation line are seen at low injection mass flows, which is a desirable characteristic.

12

Figure 10 shows that in many cases, 0.19δ gave the maximum improvement in pressure recovery. However, in some instances 0.58δ continued to improve pressure recovery, indicating that the ideal injection position probably lies somewhere between $0.19\text{-}0.58\delta$ upstream of the separation.

Effect of Injection Angle

The final parameter that was varied in our study was injection angle with respect to the free stream (see Figure 11). Injection angle was examined to try to determine the effects of injection on secondary flows. If secondary flows were the primary cause of total pressure loss in the inlet, then injecting at an angle to counter these flows might be expected to have a large effect on pressure recovery. Injectors Four, Six, and Seven were designed to study this possibility. Each has a slot width of 0.01 inches and each was placed 0.19δ upstream of the separation line. The angle of injection is measured with respect to the free stream flow direction in the inlet. Injector Four injects flow parallel to the freestream (zero angle), injector Six injects 6° away from the flow direction, and injector Seven injects 12° away from the flow direction.

Figure 12 shows the effects on pressure recovery of angled injection. It can be seen that injecting at zero degrees produces a greater gain in pressure recovery than injecting at any positive angle for most cases. However one would expect that if secondary flows were indeed the primary cause of distortion, injecting at an angle would be superior to injecting directly downstream, and alternatively, if secondary flows are not the primary cause of distortion, injecting at an angle would result in relatively small improvements in pressure recovery. In our studies, however, the performance of the angled injectors is quite good relative to most of the axial injectors and in some cases performed better. One simple conclusion that we might draw from this study is that results are relatively insensitive to injector angle; a useful result in highly

13

3-dimensional inlets whose separation line is either poorly known or changing as a function of operating condition. In other words, it appears that one can inject at an angle that is 5 to10 degrees different than the 'ideal' angle without incurring a large penalty. Injection position relative to the separation line appears to be more important.

Performance of an "Optimized" Injector

A final injection configuration was examined in attempt to take advantage of what was learned in the parametric study. Injector Block Eight had a slot width of 0.015 inches, injected flow parallel to the free stream, and was located 0.39δ upstream of the separation line.

As predicted, this configuration returned the greatest improvement in pressure recovery for any given injection mass flow. Figure 13 shows area averaged pressure recovery plotted against injection mass flow. This final configuration provided an improvement in pressure recovery of 3.75% for an injection mass flow of 2% of inlet flow at cruise conditions, a recovery of nearly 60% of the original loss. Figure 14 provides an illustration of what was achieved through the parametric study by comparing the pressure recoveries from Injector One to those of Injector Eight. Figure 15 compares the effect of original injector on the pressure profile to the best injector to date.

The improvement in distortion at the AIP resulting from this injection configuration was examined by way of DC(60) and the circumferential distortion intensity, DPCP. DC(60) is defined as

$$DC(60) = \frac{\overline{P_t}\big|_{360°} - \overline{P_t}\big|_{60°}}{\frac{1}{2}\rho\overline{c}_x^2} \qquad (5)$$

14

where c_x is the axial velocity, $\overline{P_t}\Big|_{360}$ is the average total pressure at the AIP, and $\overline{P_t}\Big|_{60}$ is the average total pressure over the worst 60 degrees of the AIP. Without injection the top 60 degrees of the AIP have the lowest pressure recovery; with injection, the top improves and the bottom 60 degrees become the worst. However, because the bottom was ignored, only the top 60 degrees were used in the calculation. DC(60) is plotted versus mass flow in Figure 16 for several inlet mass flows. Clearly injection significantly reduced distortion as measured by DC(60).

The circumferential distortion intensity, DPCP, is a numerical indication of the magnitude of the pressure distortion. The details of this parameter, as well as how it is calculated, can be found in the SAE ARP 1420 [10]. Figure 17 is a plot of DPCP for each ring of the total pressure can, where ring 1 is the innermost ring and ring 5 is the outermost ring, for three inlet mass flows. This figure shows that injection produces significant reductions in distortion intensity. Note that after injection the distortion in the lower half of the AIP is larger than the distortion at the top. According to ARP 1420 guidelines the larger distortion should be used in calculating DPCP, but again, because the bottom distortion was ignored for now, DPCP was calculated using only the upper distortion.

Summary and Conclusions

This paper presents the results of flow control experiments designed to improve the flow characteristics at the AIP in a high subsonic separating serpentine diffuser with a three-dimensional geometry. Specifically, periodic injection is used to reduce separation, and to prevent the formation of large vortices suspected of causing poor flow characteristics at the AIP. Pressure recovery and distortion, as well as DPCP and DC(60), were calculated with and without injection as the metrics for success. The effects of this type of injection on unsteadiness require further measurement and study. However, because the unsteadiness has been shown by Brear to

15

result from vortices that in turn result from separation, eliminating the separation should result in reducing the unsteadiness at the AIP.

Our results show that it is feasible to use small amounts of injected air to significantly enhance the flow properties in aggressive serpentine inlets. Adjustment of some of the geometric parameters of injection was the focus here. Several conclusions can be drawn from this study. As expected from low Mach number studies, high Mach number separating flows are more responsive to a given level of mass injection if that injection has high momentum ratio. However there is a threshold beyond which increasing the injection momentum by reducing slot width is difficult; slots that are too thin appear to be detrimental to pressure recovery per unit injected mass flow. Therefore reducing the slot width roughly to the point where the jet velocity is unity is a conjectured rule-of-thumb. Figure 8 indicates that there is a threshold momentum ratio below which very little effect is felt; this supports the notion that the injection velocity must exceed the free stream velocity to have significant effect. We also showed that injecting about 0.2δ upstream of the separation point is very desirable to reduce the mass flow required to reattach the flow. We found much less sensitivity to slot *angle* with respect to the separation line; this insensitivity should make it possible to use CFD-calculated separation locations in 3D inlets for flow control placement. The implications for this type of injection on secondary flows are not clear from our results.

Although the amount of mass flow required in our experiments was reasonably small, the overall flow control process was not efficient from an energy perspective. The reason is that we create pulsating flow using a valve that is choked over much if not all of the duty cycle. In such valves, simple compressible flow considerations lead one to estimate that perhaps 20% of the energy of the source fluid can be converted into kinetic energy; the remainder is lost across the

16

normal shock in the valve, through viscous mechanisms, or is simply never converted from enthalpy to velocity. After the flow enters the inlet itself, one might hope that the improvement in the kinetic energy at the AIP (i.e. the reduction in the separation/mixing losses) will be much greater than the energy of the injected flow. Crude measurements in our experiment indicate that this is probably the case; however the gain is not sufficient to make up for the energy lost in the valve.

There are various ways one might reduce the actuator losses, and thereby improve overall efficiency. One way is to induce resonance in a chamber upstream of the injection; this should reduce the mean mass flow required to achieve high peak injection velocity. Such an approach is practical, and its systematic study could help determine the relative importance of the mean vs. the peak momentum injection in high Mach number flows. Another approach would be simply to design a valve that operates unchoked over most of the duty cycle. This is a difficult approach to make practical since geometry is difficult to vary in a high-frequency valve, so mean mass flow is usually modulated using back pressure; under these conditions choking and unchoking of the valve over it's operating range would make for somewhat nonlinear valve behavior. On the other hand, a *fluidic* approach to flow injection modulation might both allow unchoked internal operation and reduce mechanical complexity.

Acknowledgements

References

[1] D. Greenblatt and I. J. Wygnanski, "The control of flow separation and by periodic excitation," *Progress in Aerospace Sciences*, vol. 36, pp. 487-545, 2000.

[2] Amitay, M., Pitt, D., Kibens, V., Parekh, D., and Glezer, A., "Control of Internal Flow Separation using Synthetic Jet Actuators," AIAA 2000-0903.

[3] McElwain, Brian D., 2002, "Unsteady Separation Point Injection for Pressure Recovery Improvement in High Subsonic Diffusers," M.S. Thesis, Massachusetts Institute of Technology.

[4] Hamstra, J.W., Miller, D.N., Truax, P.P.,Anderson, B.E., Wendt, B.J., October 2000, "Active Inlet Flow Control Technology Demonstration," The Aeronautical Journal, Vol. 104, No. 1040.

[5] Rabe, Angie, Olcmen, Semih, Anderson, Jason, Budisso, Ricardo, Ng, Wing, "A facility for Active Flow Control Research in Serpentine Inlets," 40th AIAA Aerospace Sciences Meeting and Exhibit, AIAA-2002-0510, Reno, NV, 2002.

[6] Brear, Michael J., Warfield, Zachary, Mangus, John F., Braddom, Cpt. Steve, Paduano, James D., Philhower, Jeffry S., "Flow Separation within the Engine Inlet of an Uninhabited Combat Air Vehicle (UCAV)," 4th ASME_JSME Joint Fluids Engineering Conference, Honolulu, Hawaii, 2003.

[7] Braddom, S., 2002, "Design and Characterization of Robust Hot Film Sensors for Tactical Aircraft Inlets," M.S. Thesis, Massachusetts Institute of Technology.

[8] Suzuki, T. and Colonius, T., "Large-scale unsteadiness in a two-dimensional diffuser: Numerical study toward active separation control," 41st AIAA Aerospace Sciences Meeting and Exhibit, AIAA-2003-1138, Reno, NV, 2003.

[9] MacMartin, D., Verma, A., Murray, R., Paduano, J., "Active Control of Integrated Inlet/Compression Systems: Initial Results," ASME Fluids Engineering Division Summer Meeting, FEDSM2001-18275, New Orleans, LA, 2001.

[10] SAE Committee S-16, "ARP-1420 – Gas turbine engine inlet flow distortion guidelines."

[11] Lorber, P., McCormick, D., Anderson, T., Wake, B., MacMartin, D., Pollack, M., Corke, T., Breur, K., "Rotorcraft Retreating Blade Stall Control," Fluids 2000 Conference and Exhibit, AIAA 2000-2475, Denver, CO, June, 2000.

[12] Mangus, John, personal correspondence.

Figure 1

Figure 2

Rotary Valve
Air Supply
AIP
Steady Total Pressure Can (40 Probes)
Variable, Calibrated Mass Flow Plug
Bellmouth Interface
Inlet Flow
Injector
Diffuser
To De Laval Compressor

Figure 3

Figure 4

21

Figure 5

Figure 6

Figure 7

Figure 8

23

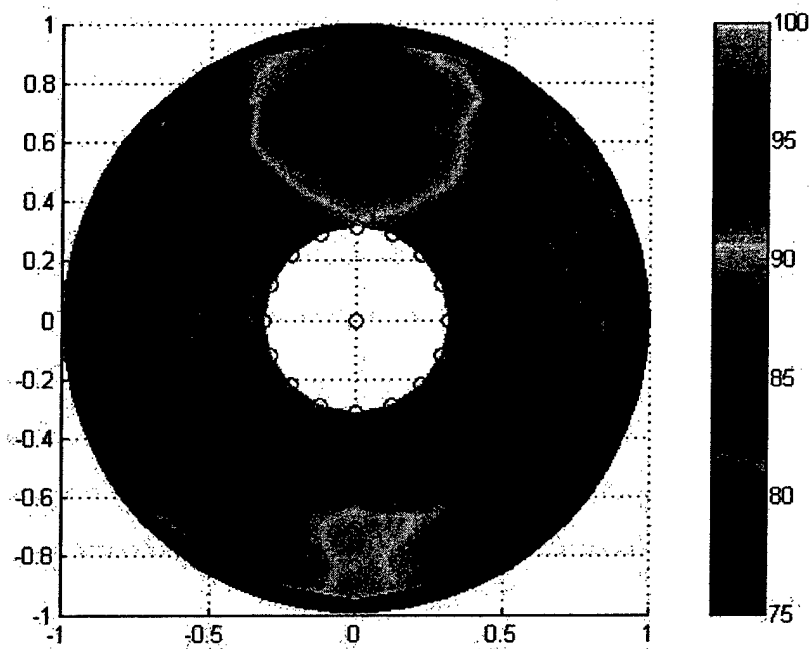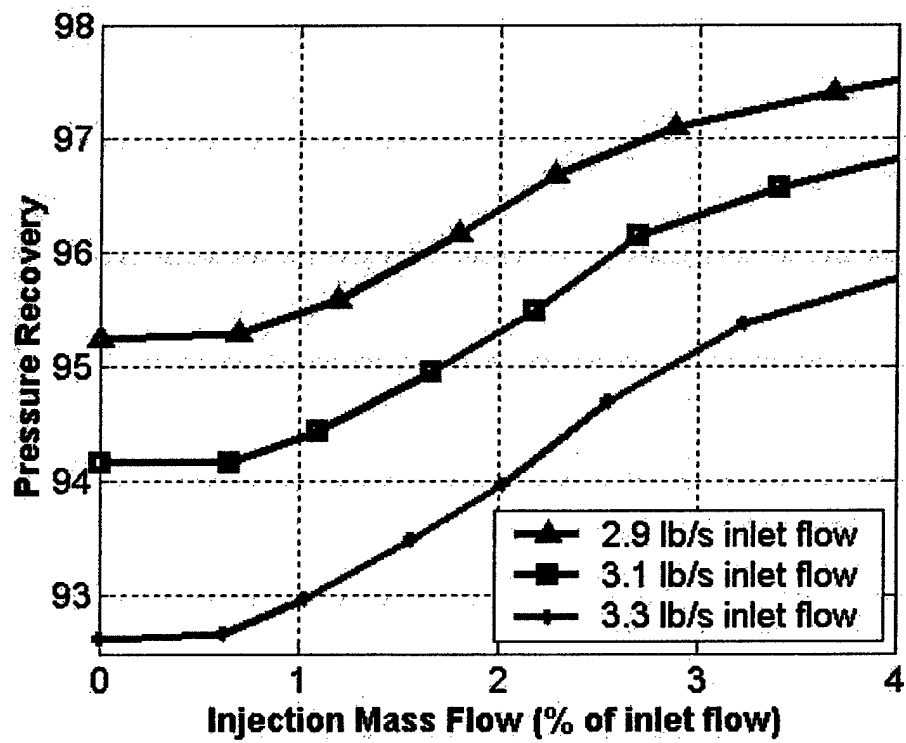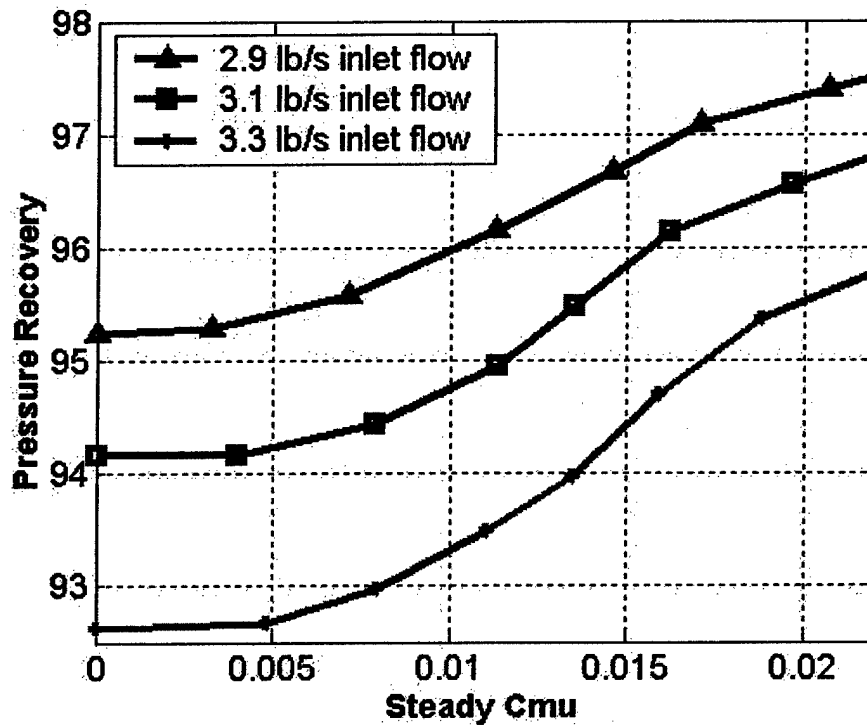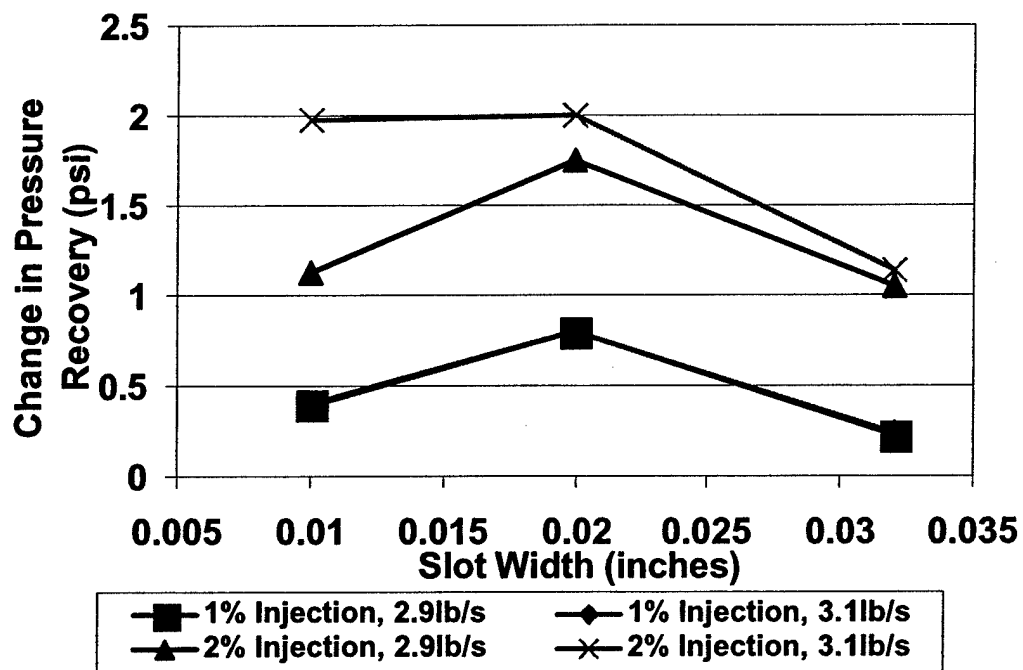## UCAV LSIM Boundary Layer Thickness
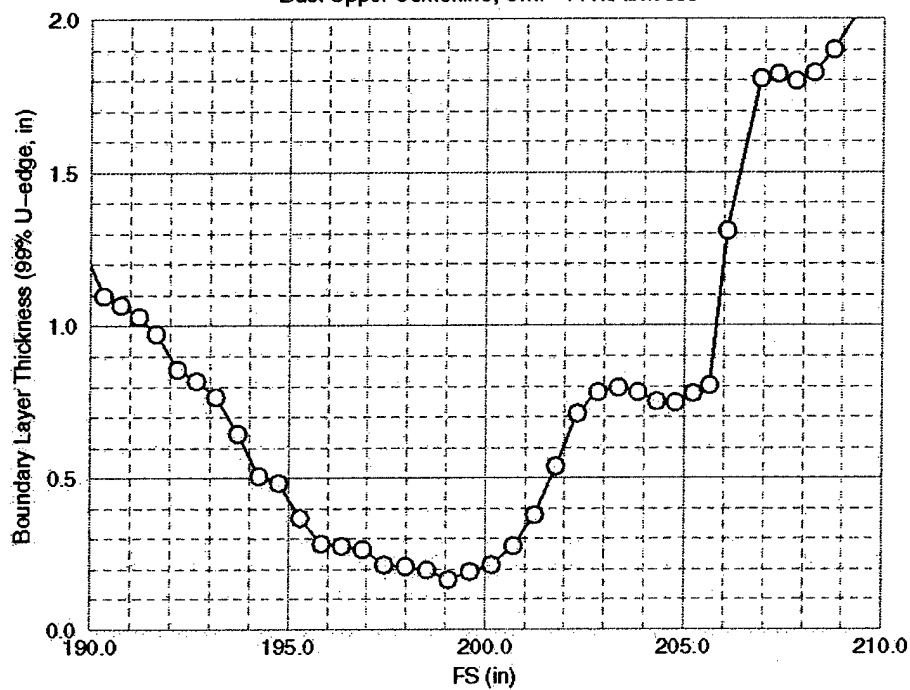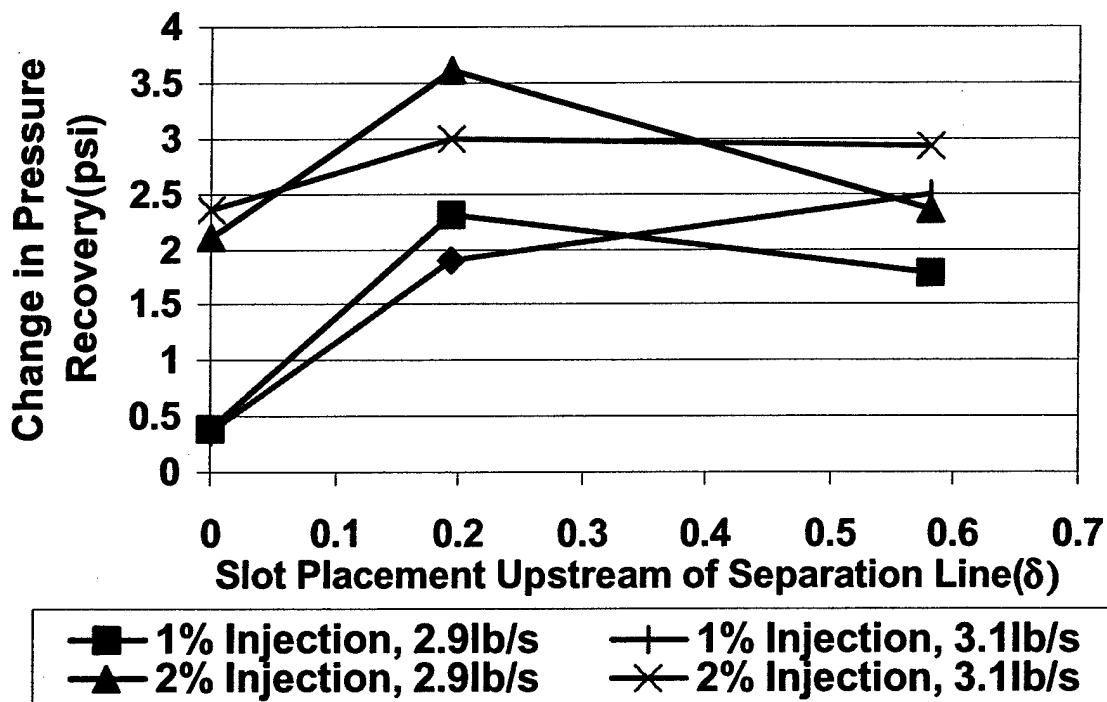
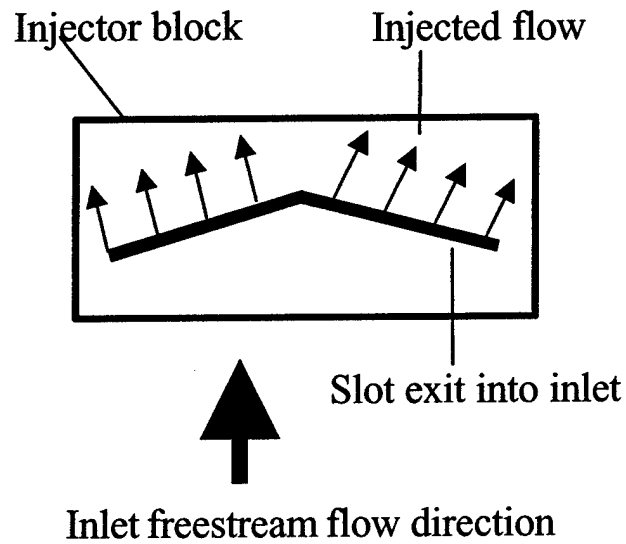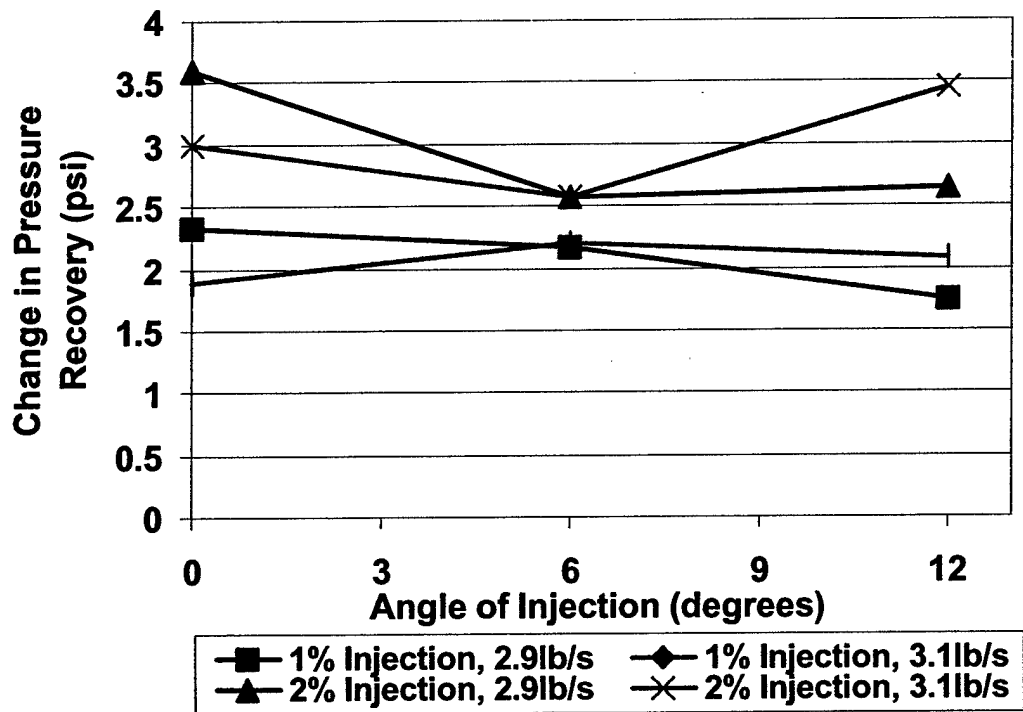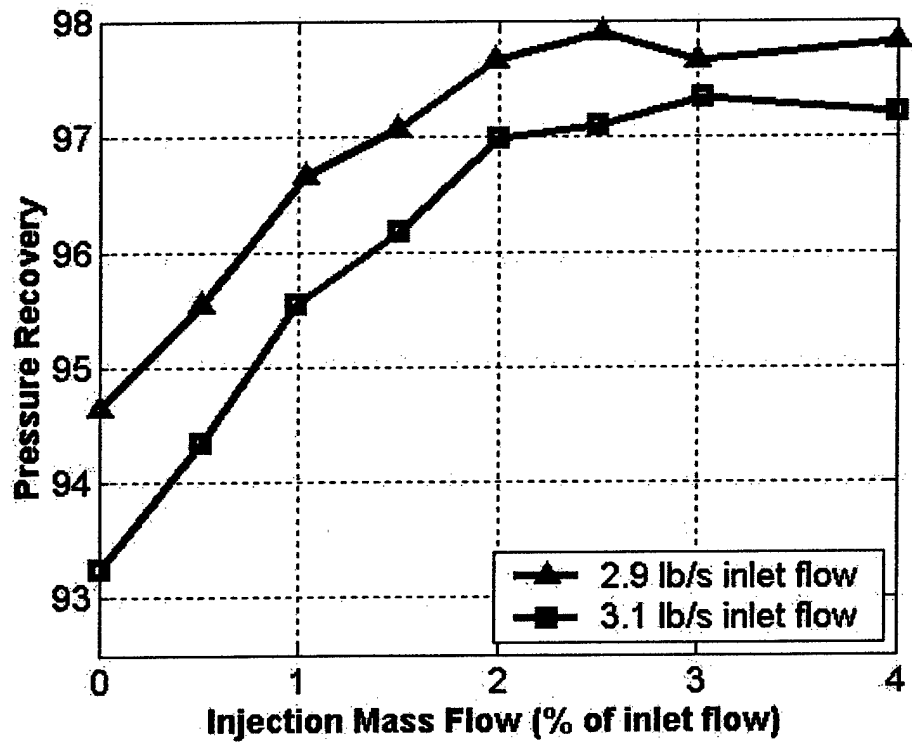### Duct Upper Centerline, CMF=111.5 lbm/sec

Figure 9

Figure 10

Figure 11

Figure 12

Figure 13

Figure 14

0.032 inch slot at Separation Point

No Injection   **2% Injection**

0.015 inch Slot, 0.39δ Upstream of Separation Point

No Injection   **2% Injection**
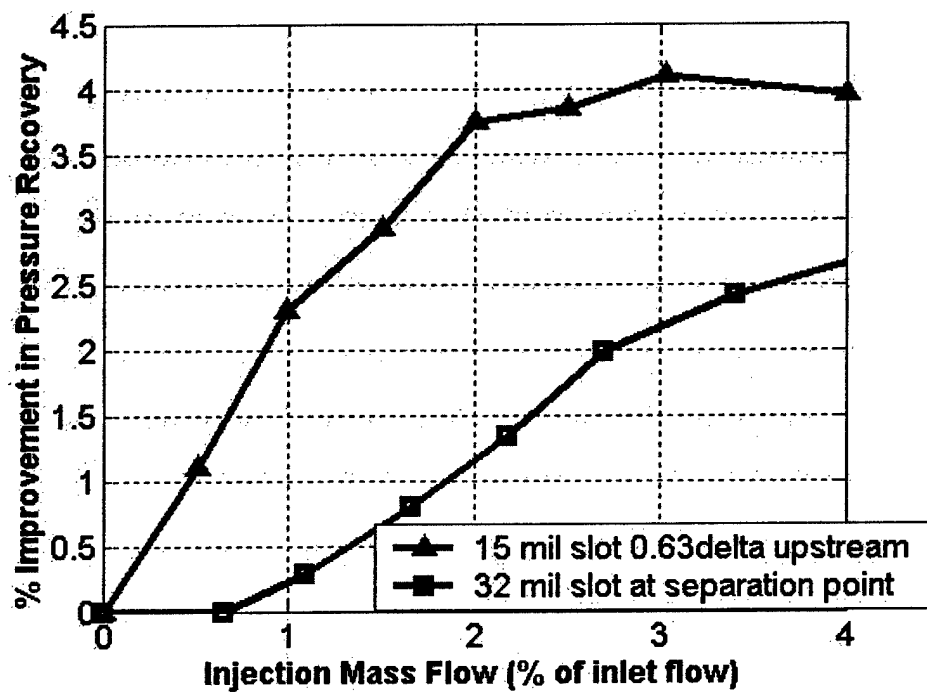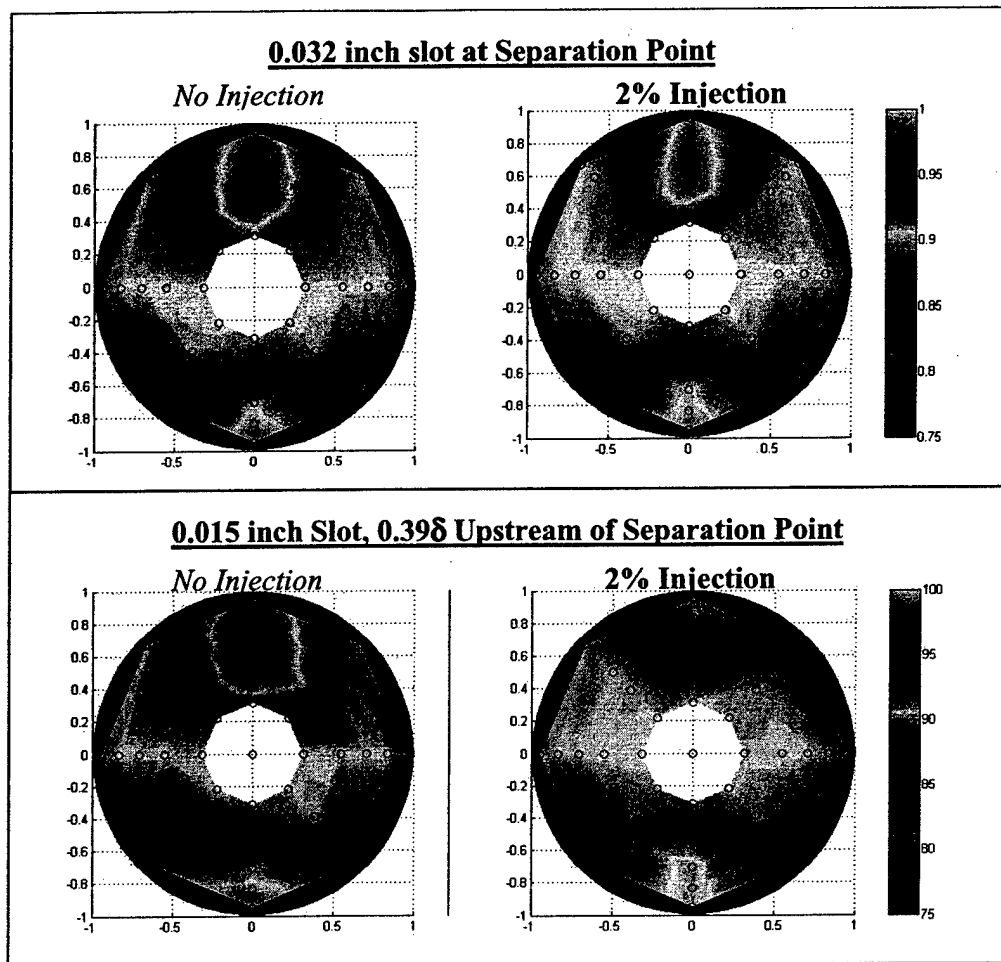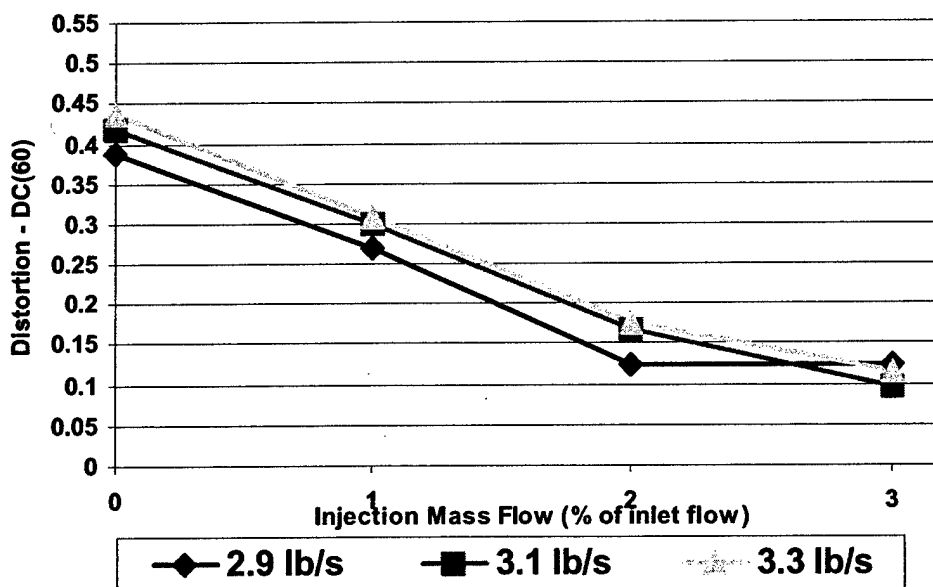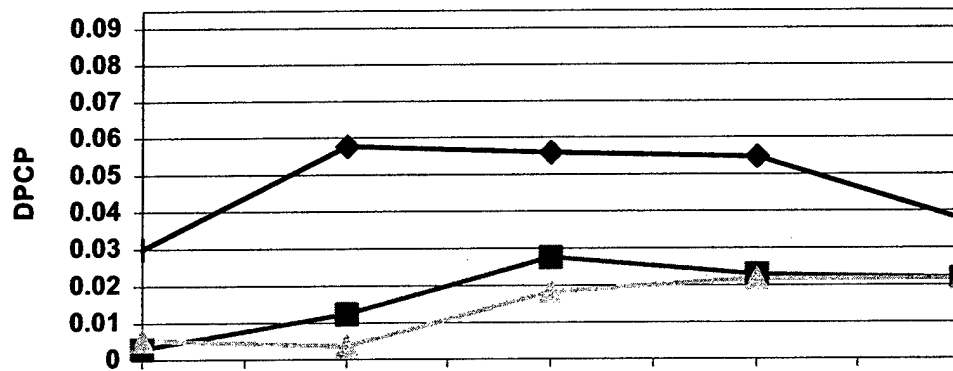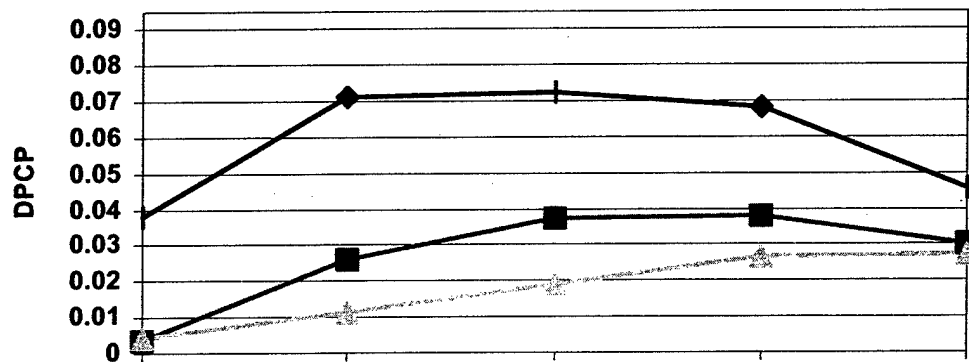
Figure 15

Figure 16

27

2.9 lb/s Inlet Mass Flow

3.1 lb/s Inlet Mass Flow

3.3 lb/s Inlet Mass Flow
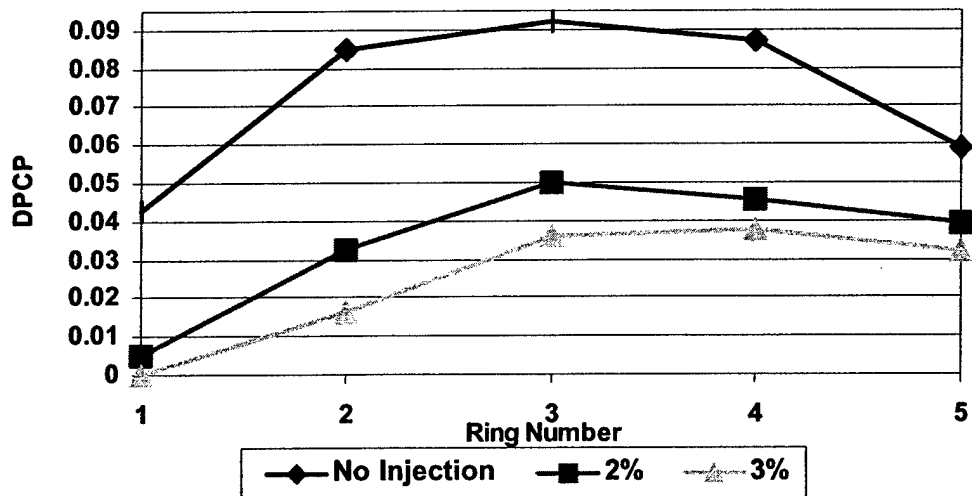

Figure 17

LARGE-SCALE UNSTEADINESS IN A TWO-DIMENSIONAL DIFFUSER: NUMERICAL STUDY TOWARD ACTIVE SEPARATION CONTROL

Takao Suzuki and Tim Colonius [t]

Division of Engineering and Applied Science
California Institute of Technology, Pasadena, California 91125

ABSTRACT

We develop a reduced order model for large-scale unsteadiness (vortex shedding) in a two-dimensional diffuser and study the mechanisms of active flow separation control. This model can estimate the vortex shedding frequency for inviscid flows by accounting for the accumulated vorticity flux in the diffuser. The model can also predict the stagnation pressure loss, which consists of two parts: A steady part corresponds to static pressure loss on the detached area, and an unsteady part is associated with vortex shedding. To validate this model, we perform direct numerical simulation (DNS) of compressible, laminar diffuser flows. The comparison between the model and DNS shows good agreement at various Mach numbers and area ratios of the diffuser in terms of vortex shedding time scale and stagnation pressure loss. To investigate the effects of periodic mass injection near the separation point, we also perform DNS over a wide range of the forcing frequency. The DNS results show that periodic mass injection can pinch off vortices with a smaller size; accordingly, their convective velocity is increased, absorption of circulation from the wall is enhanced, and the extent of the separated region is reduced. As a result, the stagnation pressure recovery, particularly the unsteady part, is substantially improved as predicted by the model.

INTRODUCTION

To achieve high performance in aircraft propulsion systems, it is crucial to reduce stagnation pressure loss across an inlet diffuser. In many situations the length of the diffuser is restricted, e.g. low-observability constraints and rapid area changes are required (c.f. Hamstra, *et al.* 2000; MacMartin, *et al.* 2001). As a result, large adverse pressure

gradients between the throat and compressor face cause boundary layer separation, i.e. stall. Previous experimental studies (e.g. Reneau, Johnston, & Kline 1967) have been used to categorize stall regimes for a planar diffuser geometry. Particularly, in the so-called "transitory stall regime," the boundary layer separation is continuously built up and semi-periodically washed out; thus, the flow pattern looks similar to vortex shedding from a bluff body. Such a pattern has been visualized in experiments (Salmon, Bogar, & Sajben 1983). This phenomenon leads to substantial reduction in stagnation pressure.

In past, a number of studies have demonstrated that the pressure recovery can be improved if large scale vortical disturbances are disrupted. In fact, some experimental studies successfully reduced the stagnation pressure loss, for example, by using splitter vanes (Rao 1971), steady mass injection (Nicoll & Ramaprian 1970; Back & Cuffel 1982; Nishi, Yoshida, & Morimitsu 1998), a star tail-pipe (Welsh 1976), etc. In these studies, however, the optimal design parameters, such as the mass flow rate or the rotation rate of the actuator, were only empirically studied. In this study, we consider periodic mass injection in order to simulate a synthetic jet (c.f. Glezer & Amitay 2002). This technique was initially introduced for airfoil separation control (e.g. Seifert, Darabi, & Wygnanski 1996) and has been recently applied to internal flow separation control (e.g. Narayanan & Banaszuk 2003, and others). These studies have found that periodic separation enhances pressure recovery more than previous active flow control techniques. Thus, the objective of this research is to investigate the large-scale flow unsteadiness intrinsic to transitory stall in a two-dimensional diffuser and to study the mechanisms of the periodic mass injection technique to control flow separation.

We develop a compressible inviscid model to scale the vortex shedding time period by accounting for the accumulated vorticity flux in a diffuser. We also estimate the stagnation pressure loss based on an
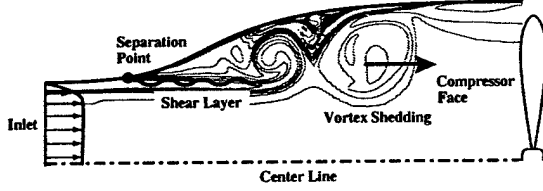
1

Figure 1: Schematic of vortex shedding in a two-dimensional diffuser.

Figure 2: Simple two-dimensional diffuser model.

ideal fluid. This model consists of steady and unsteady parts, the former accounts for static pressure loss on the separated region and the latter for vortex shedding. This model provides implications for reducing stagnation pressure loss. Based on this model, we study the frequency dependence of periodic mass injection near the separation point.

To verify the theoretical analyses, we perform direct numerical simulations (DNS) of two-dimensional laminar diffuser flows at various inflow Mach numbers ($M_1 = 0.2 \sim 0.8$) and the diffuser area ratios ($h_2/h_1 = 1.4 \sim 2.6$): We compare the shedding time period calculated from DNS and the time scale given by the theory. We also compare the stagnation pressure loss between DNS and the incompressible model. To investigate the effects of periodic mass injection, we locally force the boundary layer at several different frequencies and analyze each component of the stagnation pressure loss based on DNS in detail.

The outline of the paper is as follows: In the next section, the vortex shedding model is introduced, and the stagnation pressure loss is estimated in the incompressible limit. Next, the procedures of the numerical simulations are presented. Subsequently, the DNS results are compared with the theories.

THEORETICAL APPROACH

MECHANISM OF VORTEX SHEDDING

To estimate the vortex shedding frequency, we consider a simple two-dimensional symmetric diffuser geometry (see figure 2 for the coordinate system) and assume an inviscid fluid. We take a control volume as shown in figure 2 and calculate the accumulated vorticity flux per unit time. In compressible flows it is appropriate to calculate the flux of ω/ρ (c.f. section 1.5 of Saffman 1992). Recall that Kelvin's circulation theorem ensures that circulation is neither generated nor dissipated in an inviscid (and barotropic) fluid. Of course, some vorticity flux is generated or absorbed through the diffuser wall due to the non-slip boundary condition, but this will be taken into account later.
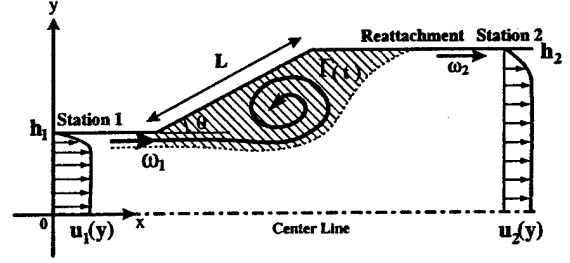
We assume that the inflow velocity and temperature profiles are transversely sheared, denoted by $u_1(y)$ and $T_1(y)$, respectively. The inflow pressure is assumed constant (denoted by p_1); consequently, the density is given from the ideal gas law as $\rho_1(y)$. Furthermore, we assume that in the diffuser the separated boundary layer reattaches before it reaches the out-flow boundary (station 2 in figure 2). The exit conditions are similarly assumed, and they are expressed using the subscript 2 (such as $u_2(y)$ as the exit velocity profile). Consequently, the net circulation (per density) accumulated in the control volume per unit time can be calculated as

$$
\frac{1}{\bar{\rho}}\frac{d\Gamma}{dt} \equiv \int_0^{h_1} \frac{\omega_1(y)}{\rho_1(y)} u_1(y)dy - \int_0^{h_2} \frac{\omega_2(y)}{\rho_2(y)} u_2(y)dy
$$
$$
= \frac{R}{p_1}\int_0^{u_1} T_1(u_1)u_1 du_1 - \frac{R}{p_2}\int_0^{u_2} T_2(u_2)u_2 du_2, \quad (1)
$$

where $\bar{\rho}$ on the left hand side denotes a characteristic density scale, and R the universal gas constant.

To evaluate the temperature profile, we use the Crocco-Busemann relation (c.f. section XV of Schlichting 1960). For an iso-thermal wall, the temperature profile can be calculated as

$$
\frac{T(u)}{T_\infty} = \frac{T_{\text{wall}}}{T_\infty} + \left(1 - \frac{T_{\text{wall}}}{T_\infty} + \frac{u_\infty^2}{2c_p T_\infty}\right)\frac{u}{u_\infty}
$$
$$
- \frac{u_\infty^2}{2c_p T_\infty}\left(\frac{u}{u_\infty}\right)^2, \quad (2)
$$

where c_p represents the specific heat at constant pressure ($\equiv \gamma R/(\gamma - 1)$, γ being the specific heat ratio). In addition, the subscript ∞ denotes the free-stream quantity (i.e. above the boundary layer), which is assumed identical to the center-line quantity, and T_{wall} is the wall temperature, which is assumed constant everywhere. Recall that (2) is derived assuming that the temperature is a function of velocity only and the Prandtl number is unity. Now, substituting (2) into (1) yields

2

$$\frac{1}{\bar{\rho}}\frac{d\Gamma}{dt} = \frac{u_1^2}{2\rho_1}\left[\frac{2}{3} + \frac{1}{3}\frac{T_{\text{wall}}}{T_1} + \frac{(\gamma-1)M_1^2}{12}\right]$$
$$- \frac{u_2^2}{2\rho_2}\left[\frac{2}{3} + \frac{1}{3}\frac{T_{\text{wall}}}{T_2} + \frac{(\gamma-1)M_2^2}{12}\right] . \quad (3)$$

Here, $M_j \equiv u_j/\sqrt{\gamma R T_j}$ ($j = 1$ or 2) is the Mach number, and the quantities without (y) denote the center-line quantities (such as, $u_1 \equiv u_1(0)$). It is important to notice that the net vorticity flux (per unit density) is independent of the velocity profile.

During one period of vortex shedding (referred to as T_{shed}), we assume that the accumulated circulation forms a single vortex in the hatched region in figure 2. In a viscous flow some vorticity flux is absorbed from the wall, and this rate is expressed by λ (which will be formulated in (22) later). Now, we assume that the diameter of the vortex can be scaled as $(h_2 - h_1)$ and its averaged density $\bar{\rho}$ in (3) as ρ_1 (in fact, it is even lower due to compressibility). Using Stokes' theorem, the averaged velocity at the outer radius of this vortex can be estimated as

$$\bar{u} \approx \frac{(1-\lambda)\frac{\rho_1}{\bar{\rho}}\frac{d\Gamma}{dt} \cdot T_{\text{shed}}}{\pi(h_2 - h_1)} . \quad (4)$$

When this velocity exceeds some velocity scaled by the free-stream velocity (denoted by αu_1), we hypothesize that the vortex is pinched off. Note that as the area ratio becomes greater, the vortex formation criterion suggested by Gharib, Rambod, & Shariff (1998) may be applied. Now, the time period of vortex shedding can be then estimated as

$$T_{\text{shed}} \approx \alpha \tau_{\text{shed}} \equiv \frac{\alpha}{1-\lambda}\frac{2\pi h_1\left(\frac{h_2}{h_1} - 1\right)}{u_1 F} , \quad (5)$$

where

$$F(M_1, \frac{h_2}{h_1}, \frac{u_2}{u_1}, \frac{T_2}{T_1}, \frac{T_{\text{wall}}}{T_1})$$
$$\equiv \left[\frac{1}{2} + \frac{1}{3}\frac{T_{\text{wall}}}{T_1} + \frac{1}{6}\left(1 + \frac{\gamma-1}{2}M_1^2\right)\right] - \left(\frac{h_2}{h_1}\right)\left(\frac{u_2}{u_1}\right)^3$$
$$\times \left[\frac{1}{2} + \frac{1}{3}\frac{T_{\text{wall}}}{T_1}\frac{T_1}{T_2} + \frac{1}{6}\left(1 + \frac{\gamma-1}{2}M_1^2\right)\frac{T_1}{T_2}\right] . \quad (6)$$

Here, it is assumed that the effects of the boundary layer are sufficiently small so that the center-line quantities follow the continuity and the energy conservation given from a quasi-one-dimensional analysis. It is also noted that the velocity and temperature ratios are determined from the area ratio assuming the ideal expansion and the quasi-one-dimensionality. This is equivalent to treating a subscript as a cross section average.
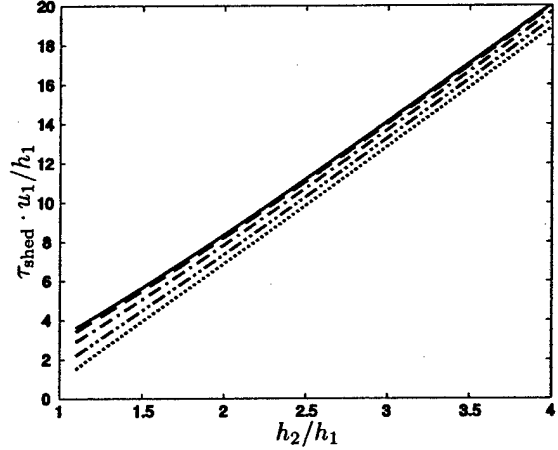

Figure 3: Compressible effect on the vortex shedding time period. The vortex shedding time period versus the area ratio at various inflow Mach numbers are shown: ———, Incompressible limit; — — —, $M_1 = 0.2$; — · — · —, $M_1 = 0.4$; — · · — · · —, $M_1 = 0.6$; · · ·, $M_1 = 0.8$. The absorption of circulation from the wall is neglected ($\lambda = 0$).

Notice that in incompressible flows, (5) yields the following simple expression:

$$T_{\text{shed}} \approx \alpha \tau_{\text{shed}}^{(M\to 0)} \equiv \frac{\alpha}{1-\lambda}\frac{2\pi h_1\left(\frac{h_2}{h_1}\right)^2}{u_1\left(1 + \frac{h_2}{h_1}\right)} , \quad (7)$$

where we assume that $\rho_1 = \rho_2$, $T_1 = T_2 = T_{\text{wall}}$, and $M_1 = 0$. Figure 3 plots the shedding time period as a function of the area ratio at various inflow Mach numbers. Here, p_2/p_1 is calculated based on the ideal expansion, and $T_{\text{wall}} = T_1$ is assumed. It shows that the shedding period becomes longer as the area ratio increases.

STAGNATION PRESSURE LOSS

STEADY PART

In this section we evaluate stagnation pressure loss due to flow separation and large scale flow unsteadiness in an incompressible limit. We start with Crocco's equation:

$$\frac{\partial u_i}{\partial t} + \frac{\partial}{\partial x_i}\left(h + \frac{u_k^2}{2}\right) - T\frac{\partial s}{\partial x_i} = \epsilon_{ijk}u_j\omega_k + \frac{1}{\rho}\frac{\partial \tau_{ij}}{\partial x_j} , \quad (8)$$

where h is enthalpy ($\equiv c_p T$), s is entropy, and τ_{ij} is the viscous stress tensor. Defining stagnation temperature to be $T_t \equiv (h + \frac{u_i^2}{2})/c_p$, and accordingly, stagnation pressure and density to be

$p_t \equiv (T_t/T)^{\frac{\gamma}{\gamma-1}} p$ and $\rho_t \equiv (T_t/T)^{\frac{1}{\gamma-1}} \rho$, respectively, (8) can be rewritten as

$$\frac{\partial p_t}{\partial x_i} = \rho_t \epsilon_{ijk} u_j \omega_k - \rho_t \frac{\partial u_i}{\partial t} + (T - T_t)\rho_t \frac{\partial s}{\partial x_i} + \frac{\rho_t}{\rho} \frac{\partial \tau_{ij}}{\partial x_j} .$$
(9)

Note that entropy is the same between static and stagnation quantities by definition. Now, we evaluate the order of each term in (9). Here, we assume that the compressibility is weak and expand both static and stagnation thermodynamic quantities for small M^2. For example, $p \approx p_\infty + M^2 \tilde{p}_{M^2} + M^4 \tilde{p}_{M^4} + \cdots$, etc. In addition, we assume that the time scale of the fluid motion is proportional to $1/M$, namely $(\frac{\partial}{\partial t})/(\frac{\partial}{\partial x}) \sim O(M)$. The first two terms on the right hand side of (9) then yield $O(M^2)$. The third term can be estimated as $O(M^4/Re)$ referring to the entropy change along the material line (if the flow is not initially homoentropic, its order is $O(M^4)$). Likewise, the last term can be evaluated as $O(M^2/Re)$. Thus, assuming $Re \gg 1$ and neglecting $O(M^4)$ terms, (9) can be approximated as

$$\frac{\partial p_t}{\partial x_i} \approx \rho_t \epsilon_{ijk} u_j \omega_k - \rho_t \frac{\partial u_i}{\partial t} .$$
(10)

Next, we integrate (10) for $i = 1$ (the x direction) inside the control volume defined in figure 2. Using Green's theorem, the left hand side yields the surface integrals. Integrating over the cross section, the second term on the right hand side vanishes for a symmetric vortex, as discussed later. Alternatively, if we take a time average and expand this term as $\overline{(\rho_\infty - \rho)\frac{\partial u}{\partial t}} - \rho_\infty \frac{\partial u}{\partial t}$, it is evaluated as $O(M^4)$. Consequently, the stagnation pressure loss averaged in the vertical direction can be approximated as

$$p_{t1} - p_{t2} \approx (p_{t1} - p_w)\left(1 - \frac{h_1}{h_2}\right) - \frac{\int\int \rho_t v\omega \, dx \, dy}{h_2} ,$$
(11)

where the averaged pressure projected on the wall is defined as $p_w \equiv \int_{h_1}^{h_2} p \, dy/(h_2 - h_1)$. In a fully separated diffuser, $p_w \approx p_1$. As mentioned in the previous section, quantities with a subscript denote the cross section average. Figure 4 shows the error of (11) assuming $p_w = p_1$. Slight under-estimate of pressure on the wall ($\sim 5\%$) causes over-estimate of the stagnation pressure loss. Nonetheless, the time variation of the error in (11) is relatively small (the averaged error during $tu_1/h_1 \in [24, 120]$ in figure 4 is approximately -2.1%). Thus, our strategy to suppress the stagnation pressure loss is to increase p_w and $\int\int \rho_t v\omega \, dx \, dy$.
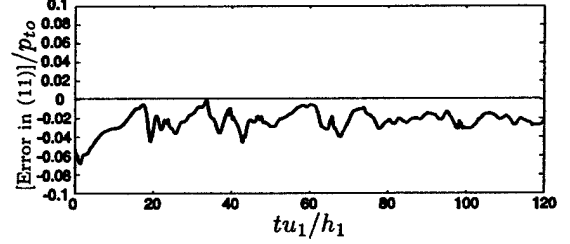

Figure 4: Error in the estimate of stagnation pressure loss. Referring to (11), (L.H.S. − R.H.S.)/p_{to} is plotted, where $p_{to} \equiv (1 + \frac{\gamma-1}{2}M_1^2)^{\frac{\gamma}{\gamma-1}} p_1$. Correction of the projected area noted in table 1 is also taken into account.

Now, the steady part of $\int\int \rho_t v\omega \, dx \, dy$ can be readily evaluated in incompressible flows. Imposing the non-slip boundary conditions on the wall, this term can be expanded as follows:

$$\int\int \rho_t v\omega \, dx \, dy \approx \int\int \rho_\infty v\left(\frac{\partial v}{\partial x} - \frac{\partial u}{\partial y}\right) dx \, dy$$

$$= -\rho_\infty \int\int \frac{\partial(u^2/2)}{\partial x} dx \, dy = \rho_\infty \frac{u_1^2 h_1 - u_2^2 h_2}{2} . \quad (12)$$

Here, continuity is used, and $v_1 = v_2 = 0$ is assumed for the third equality. This relation is nothing but a momentum balance of the control volume. Thus, the steady part of the time averaged stagnation pressure loss can be expressed as

$$(\overline{p_{t1} - p_{t2}})_{\text{steady}}^{M \to 0} \approx \frac{(p_1 - \overline{p_w})(\frac{h_2}{h_1} - 1)}{\frac{h_2}{h_1}} + \frac{\rho u_1^2}{2} \frac{\left(\frac{h_2}{h_1} - 1\right)^2}{\left(\frac{h_2}{h_1}\right)^2} .$$
(13)

UNSTEADY PART

The unsteady part of the $\int\int \rho_t v\omega \, dx \, dy$ term is considered to be the contribution from vortex shedding. To analyze this effect, we consider the Oseen vortex (Oseen 1912) as a model problem, which is a solution to the incompressible Navier-Stokes equations. Again, we consider the leading terms of the incompressible limit. The radial velocity of the Oseen vortex is given by

$$u_r(t, x, y) = \frac{\Gamma}{2\pi\sqrt{(x - x_o)^2 + (y - y_o)^2}}$$
$$\times \left(1 - \exp\left[-\frac{(x-x_o)^2 + (y-y_o)^2}{4\nu t}\right]\right), \quad (14)$$

4

where (x_o, y_o) denotes the center of the vortex, Γ is the total circulation, and ν is the kinematic viscosity. Here, we assume that the time scale of dissipation is much slower than that of vortex convection; accordingly, we define the radius of the vortex to be $R \equiv \sqrt{4\nu t}$ and assume it to be constant. Using this expression and assuming that the effect of blockage due to the wall is weak, we obtain the following quantity after some algebra:

$$\int_{-\infty}^{\infty} \rho_t v\omega dy$$
$$= \frac{\rho_t \Gamma^2}{2\pi R^2} \left(\text{erf}\left[\frac{\sqrt{2}(x-x_o)}{R} \right] - \text{erf}\left[\frac{x-x_o}{R} \right] \right) , \quad (15)$$

where $\text{erf}(z) \equiv \frac{2}{\sqrt{\pi}} \int_0^z e^{-t^2} dt$. Notice that (15) is positive downstream of the vortex center $(x-x_o > 0)$ and negative upstream of it $(x-x_o < 0)$. Therefore, when the Oseen vortex leaves the control volume, a stagnation pressure drop appears at the exit cross section. According to the discussion in the previous section, we estimate the parameters as $\Gamma = \alpha 2\pi R u_1$ and $R \approx (h_2 - h_1)/2$ and express the convective velocity of the vortex to be u_c. Thus, the stagnation pressure loss averaged over the exit cross section is given as a function of time,

$$(\widetilde{p_{t2}})_{\text{shed}}(t) = \frac{1}{h_2} \int_{u_c t}^{\infty} \int_{-\infty}^{\infty} \rho_t v\omega dy dx$$
$$\approx \alpha^2 \pi \rho_\infty u_1^2 \frac{h_2 - h_1}{h_2} \int_{\infty}^{\frac{u_c t}{R}} \left(\text{erf}[\sqrt{2}\chi] - \text{erf}[\chi] \right) d\chi . \quad (16)$$

When the vortex is convected along $y = h_2/2$, the convective velocity can be approximated as $u_c = u_2$. In reality, the vortex is pinched off near the wall and convected above $y = h_2/2$ when $h_2/h_1 < 2$, and *vice versa*. Therefore, the convective velocity is reduced due to the induced velocity. To be precise, the Oseen vortex is no longer the solution because the center of the vortex is convected slower than the mean flow in addition to the distortion due to the wall.

To estimate the induced velocity due to blockage, we assume an ideal fluid and consider a conformal mapping represented by $\zeta = \exp(\frac{\pi}{2h_2}z)$. This function maps an infinitely long channel onto the first quadrant; hence, two pairs of counter-rotating point vortices satisfy the non-penetration boundary condition in the ζ plane. According to the study by Pierrehumbert (1980) based on a pair of counter-rotating vortex 'patches,' convective velocities of distributed vortices can be well approximated by point vortices even if the distance between them is relatively small.

Based on point vortices, the rate of induced velocity can be calculated as (c.f. section 7.2 of Saffman 1992)

$$\kappa(\frac{h_2}{h_1}, \frac{h_3}{h_1}) \equiv -\frac{u_{\text{ind}}}{\alpha u_2} \approx -\frac{\pi}{4}\left(\frac{h_2}{h_1} - 1 \right) \frac{1}{\tan(\pi\frac{h_3}{h_1}\frac{h_1}{h_2})} , \quad (17)$$

where h_3 is the height of the vortex from the bottom, and the convective velocity then becomes $(1-\alpha\kappa)u_2$. For example, when $h_2/h_1 = 2$ and $h_3/h_1 = ((h_1 + h_2)/(2h_1) + h_2/h_1)/2 = 5/4$, κ becomes as high as 0.33 (for reference, if we simply calculate the infinite superposition of the Oseen vortices, κ yields 0.32, which is sufficiently close to the point vortex solution). Thus, the effect of blockage on the convective velocity is not negligible. On the other hand, the error of $\int\int \rho_t v\omega dx dy$ associated with blockage is less than 2%.

Using (16) and knowing that the time period of vortex shedding is estimated by (7), the time averaged stagnation pressure loss associated with vortex shedding can be estimated as

$$(\overline{\widetilde{p_{t2}}})_{\text{shed}}^{M\to 0} = \frac{\int_{-\infty}^{\infty} \widetilde{p_{t2}}(t)dt}{T_{\text{shed}}^{(M\to 0)}}$$
$$\approx -\frac{\alpha(1-\lambda)}{1-\alpha\kappa} \frac{\left(\frac{h_2}{h_1}+1\right)\left(\frac{h_2}{h_1}-1\right)^2}{8\left(\frac{h_2}{h_1}\right)^2} \frac{\rho u_1^2}{2}. \quad (18)$$

This equation shows that the stagnation pressure loss due to vortex shedding is proportional to the dynamic pressure in the incompressible limit. This expression is also valid when we artificially tune α; therefore, by breaking the circulation into smaller vortices, the stagnation pressure loss can be suppressed. Although we have derived (18) based on the Oseen vortex, this dependence is still valid when the vortex is radially symmetric. We define a coefficient relative to the Oseen vortex (i.e. in front of (18)) as β. In fact, β is found to be reasonably close to unity in DNS (see table 3 shown later).

Accordingly, the total stagnation pressure loss is now expressed as

$$(\overline{p_{t1} - p_{t2}})_{\text{total}}^{M\to 0} \approx \frac{(p_1 - \overline{p_w})(\frac{h_2}{h_1} - 1)}{\frac{h_2}{h_1}}$$
$$+ \frac{\rho u_1^2}{2} \frac{\left(\frac{h_2}{h_1} - 1\right)^2}{\left(\frac{h_2}{h_1}\right)^2} \left[1 + \frac{\alpha\beta(1-\lambda)}{1-\alpha\kappa}\frac{\frac{h_2}{h_1}+1}{8} \right] . \quad (19)$$
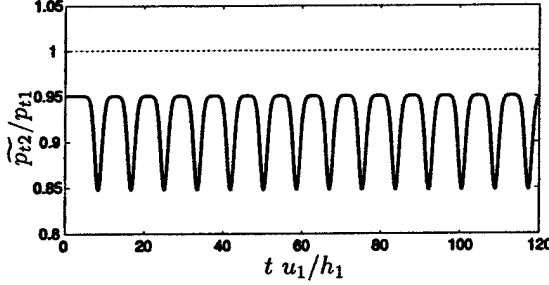
Figure 5: Stagnation pressure profile estimated based on the inviscid and incompressible limit. Parameters are chosen according to Case A ($M_1 = 0.6$ and $h_2/h_1 = 2$), and $\alpha = 1$, $\beta = 1$, $\lambda = 0$, $p_w = p_1$, and $\kappa = 0.33$ are assumed.

The first term and the first part of the second term correspond to the steady loss, and the second part of the second term to the unsteady loss. As discussed later, (19) indicates that the contribution from vortex shedding becomes comparable to the steady part as the induced velocity decelerates the convective velocity. Figure 5 shows an expected pattern of the stagnation pressure profile for a fully separated case. The troughs correspond to the unsteady loss repeated on the top of the steady part. The stagnation pressure drops when the center of the vortex is passing through the exit cross section (approximately 11% drop under the conditions corresponding to Case A defined in table 1). These theoretical predictions are examined using DNS.

VORTICITY ABSORPTION FROM WALL

Now, we consider viscous effects. In a free space, the viscous term simply diffuses the vorticity distribution but does not increase nor decrease net vorticity. Therefore, the dominant part of viscous effects should come from the vorticity flux on the wall. According to the previous discussion, the net accumulated circulation per unit time can be symbolically expressed as

$$\left(\frac{d\Gamma}{dt}\right)_{\text{total}} \approx \int_{\text{inflow}} - \int_{\text{exit}} (\text{vorticity flux}) \, dy$$
$$+ \int_{\text{wall}} (\text{vorticity flux}) \, ds \, . \quad (20)$$

To be precise, in compressible flows we must calculate flux of ω/ρ instead of "vorticity flux" as mentioned before. Thus, we assume that $(\frac{d\Gamma}{dt})$ can be approximated by $(\frac{\rho_1}{\rho}\frac{d\Gamma}{dt})$ as defined in (1). For the second term, vorticity flux coming from the wall can be expressed as (e.g. Koumoutsakos, Leonard, & Pepin 1994)

$$\int_{\text{wall}} (\text{vorticity flux}) \, ds = \int_{\text{wall}} \nu \frac{\partial \omega}{\partial n} ds = -\int_{\text{wall}} \frac{1}{\rho} \frac{\partial p}{\partial s} ds \, ,$$
$$(21)$$

where the positive sign is taken to be production. This expression is valid even in compressible flows when the dynamic viscosity μ ($= \rho\nu$) is constant everywhere. This term produces additional circulation in favorable pressure gradients, while it absorbs circulation in adverse ones.

In incompressible flows, (21) simply yields $(p_1 - p_2)_{\text{wall}}/\rho$. Assuming $(p_1)_{\text{wall}} = p_1$, the rate of absorption introduced in (4) can be expressed as

$$\lambda \equiv -\frac{p_1 - (\overline{p_2})_{\text{wall}}}{\rho\frac{d\Gamma}{dt}} = \frac{(\overline{p_2})_{\text{wall}} - p_1}{\frac{\rho u_1^2}{2}} \frac{\left(\frac{h_2}{h_1}\right)^2}{\left(\frac{h_2}{h_1}\right)^2 - 1} \, ,$$
$$(22)$$

From the previous discussion and Bernoulli's equation, the rate of accumulated circulation per unit time in the control volume is $\frac{d\Gamma}{dt} = \frac{u_1^2 - u_2^2}{2} = \frac{p_2 - p_1}{\rho}$; therefore, if this amount is perfectly absorbed from the wall (i.e. $\lambda = 1$) and the pressure on the wall coincides with the free-stream pressure, no vortex shedding occurs. However, when the flow is fully separated, vorticity is absorbed mainly near the reattachment point and the projection of recovered static pressure in the x direction is reduced.

NUMERICAL PROCEDURES

DIRECT NUMERICAL SIMULATION (DNS)

To numerically investigate diffuser flows, we performed direct numerical simulations (DNS) solving the full compressible Navier-Stokes equations in two-dimensions. For time marching the fourth order Runge-Kutta scheme was used. For spatial derivatives the sixth order Padé scheme (Lele 1992) was used for the interior points. For the inflow and exit boundary points, lower order (third and fourth order) Padé schemes were used. The rest of the boundary treatments are described later in this section.

To generate the computational grid, we used a conformal mapping. The following function gives the two-dimensional diffuser shape used in this study:

$$z = \frac{\frac{h_2}{h_1} + 1}{2}\bar{\zeta} + \frac{1}{c}\frac{\frac{h_2}{h_1} - 1}{2} \log(\cosh(c\bar{\zeta})) \, , \quad (23)$$

where $z = x + iy$ corresponds to the physical domain and $\bar{\zeta} = \bar{\xi} + i\bar{\eta}$ to an intermediate computational domain. Furthermore, this computational domain was

6

Case	M_1	h_2/h_1	$\theta_{\max}$ & c
A	0.6	2.0 (1.843)	18.43°, 0.7576
B	0.2	2.0 (1.843)	18.43°, 0.7576
C	0.4	2.0 (1.843)	18.43°, 0.7576
D	0.8	2.0 (1.843)	18.43°, 0.7576
E	0.6	1.4 (1.346)	10.78°, 0.8440
F	0.6	1.6 (1.514)	14.03°, 0.8110
G	0.6	2.6 (2.320)	22.31°, 0.6992
I~O	0.6	2.0 (1.843)	18.43°, 0.7576

Case	Re	$\delta_{b.l.}/h_1$	(N_x, N_y)	$(\Delta t\, a_2/h_2)$
A	4000	0.10	601, 151	1.0×10^{-3}
B	5000	0.10	601, 151	1.0×10^{-3}
C	4000	0.10	601, 151	1.0×10^{-3}
D	6000	0.10	801, 201	0.8×10^{-3}
E	8000	0.07	721, 181	1.0×10^{-3}
F	6670	0.08	601, 151	1.0×10^{-3}
G	2900	0.13	721, 181	0.727×10^{-3}
I~O	4000	0.10	601, 151	1.0×10^{-3}

Table 1: Flow conditions and diffuser geometries for DNS. The values in parentheses in the h_2/h_1 column denote the actual area ratio between the cross sections at which stagnation pressure profiles were recorded (see figure 6). The Reynolds number is defined as $Re \equiv u_1 h_1/\nu_1$. $\delta_{b.l.}$ denotes the inlet momentum thickness. N_x and N_y denote the numbers of grid points in the x and y directions, respectively, and Δt is the time step.

linearly stretched to efficiently resolve the boundary layer near the wall as well as the region in which vortex stretching becomes intense. Consequently, spatial differentiation was performed in an equally spaced rectangular grid. A typical computational grid is shown in figure 6. Parameters for computation and the flow geometries are all tabulated in table 1.

According to the conformal mapping, initial velocity fields were calculated based on the potential flow solution, and the thermodynamic quantities were given from the compressible Bernoulli's equation. The initial velocity and thermodynamic quantity profiles near the wall were given by solving the Blasius boundary layer equation (c.f. Schlichting 1960) ignoring the curvature of the wall.

For the wall (the upper side of the computational domain), the non-slip boundary conditions were imposed, and the temperature distribution on the wall was calculated assuming the ideal expansion and set constant in time. The bottom line was set as the center-line assuming symmetry. At the inflow and the exit, non-reflecting boundary conditions (Poinsot & Lele 1992) were imposed together
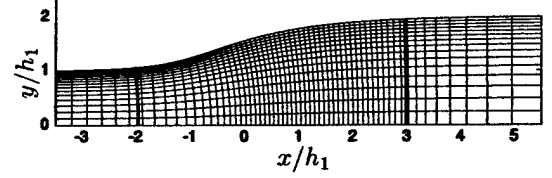

Figure 6: Typical computational grid. Every five grid point is shown for Case **A**. Thicker lines denote the sections where the stagnation pressure profiles were recorded. $\Delta x_{\min}/h_1 = 8.29 \times 10^{-3}$, $\Delta x_{\max}/h_1 = 59.45 \times 10^{-3}$, $\Delta y_{\min}/h_1 = 5.57 \times 10^{-3}$, and $\Delta y_{\max}/h_1 = 25.15 \times 10^{-3}$.
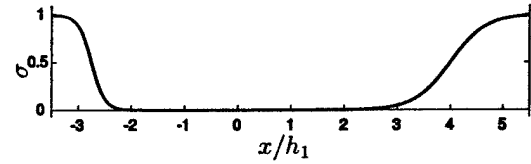

Figure 7: Strength of the sponge term.

with a "sponge" buffer zone (Freund 1997). The coefficient σ corresponding to the strength of the sponge is plotted in figure 7.

PERIODIC MASS INJECTION

To study the effects of a synthetic jet, we artificially forced the right hand side of the Navier-Stokes equations and periodically injected a mass flow near the separation point in the x direction:

$$\frac{\partial \rho}{\partial t} + \frac{\partial(\rho u_j)}{\partial x_j} = F(x_1, x_2)\rho u_s(t), \tag{24}$$

$$\frac{\partial(\rho u_i)}{\partial t} + \frac{\partial(\rho u_i u_j + p\delta_{ij} + \tau_{ij})}{\partial x_j} = F(x_1, x_2)\rho u_s^2(t)\delta_{i1}, \tag{25}$$

$$\frac{\partial[\rho(e+\frac{u_k^2}{2})]}{\partial t} + \frac{\partial[\{\rho(e+\frac{u_k^2}{2})+p\}u_j + \tau_{jk}u_k + q_j]}{\partial x_j}$$
$$= F(x_1, x_2)\rho\left(e + \frac{u_s^2(t)}{2}\right)u_s(t), \tag{26}$$

where

$$F(x,y) = \frac{A_o}{2\pi\sigma_x\sigma_y}\exp\left[-\frac{(x-x_s)^2}{2\sigma_x^2} - \frac{(y-y_s)^2}{2\sigma_y^2}\right], \tag{27}$$

$$u_s(t) = 0.9a_1\frac{1+\tanh\left(\frac{t-t_o}{\sigma_t}\right)}{2}\frac{1+\cos(\omega t)}{2}, \tag{28}$$

and (x_s, y_s) denotes the center of injection (a_1 being the speed of sound at the inlet). Thus, the forcing points were distributed using a compact and smooth function, and the injection was gradually activated so that spurious numerical disturbances can

7

Case	$\omega h_1/u_1$
I	0.5
J	0.75
K	1.0
L	1.25
M	1.5
N	2.0
O	2.5

Table 2: Frequency of mass flow injection in DNS. The base flow conditions are the same as Case **A**; namely, $M_1 = 0.6$, $h_2/h_1 = 2.0$, and $Re = 4000$ (refer to table 1).

be lessened. In actual computations, $x_s = -1.60$, $y_s = 1.04$, $\sigma_x = 0.08$, $\sigma_y = 0.01$, $A_o = 6.0 \times 10^{-3}$, $\sigma_t = 0.2$, and $t_o = 0.5$ were selected. Consequently, the momentum coefficient can be calculated as $C_\mu \equiv (\rho u_s^2 h_s)/(\rho u_1^2 h_1) \approx 0.52\%$, h_s being the corresponding slot width. The order of C_μ is comparable to experiments (e.g. Narayanan & Banaszuk 2003). An attempt was made to minimize the forcing region and to locate it closer to the wall to simulate a slot on the wall.

Seven different forcing frequencies, ω, were examined, and they are tabulated in table 2. The base flow conditions for these runs were the same as Case **A** shown in table 1.

RESULTS AND DISCUSSION

VORTEX SHEDDING FREQUENCY FOR UNFORCED CASES

Figure 8 displays vorticity contours computed from DNS at several instants in time for Case **A** (see table 1). The vorticity flux is accumulated somewhat downstream of the separation point, and a large-scale vortex is formed. While this vortex is pinched off and convected downstream, the next vortex is generated. The curved part of the wall is almost entirely contained within the separated vortex during this process.

Figure 9 depicts the time histories of stagnation pressure. It shows that the flow field has a characteristic time scale; in fact, our model, figure 5, captures such features. Referring to figure 8, it is found that one period of vortex shedding roughly corresponds to an interval between troughs in the stagnation pressure profile: When the center of the vortex passes through the exit cross section, the stagnation pressure drops. Such a trend is consistent with our analysis.
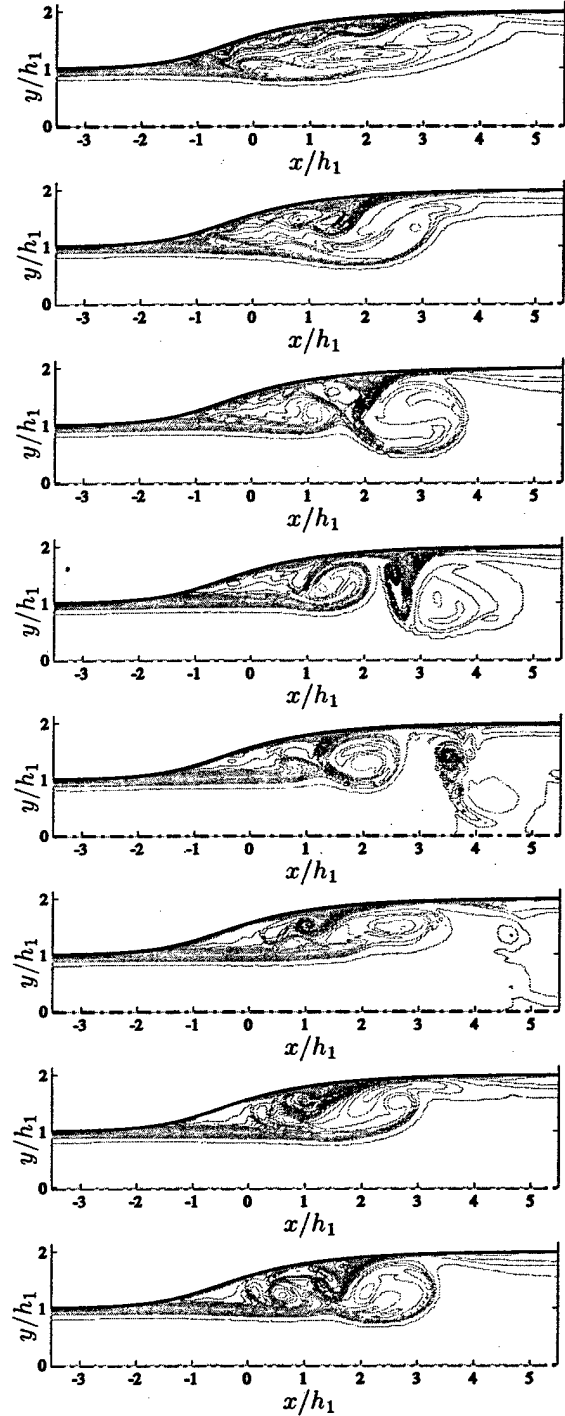

Figure 8: Vorticity evolution in a two-dimensional diffuser (unforced case, Case **A**). Vorticity contours computed from DNS are shown over time: $tu_1/h_1 = 57.6, 60.0, 62.4, 64.8, 67.2, 69.6, 72.0,$ and 74.4 from the top. Contour lines: $\omega_{\min} = -33.3$, $\omega_{\max} = 33.3$, and the interval of $\Delta\omega = 0.833$.

8

To validate the inviscid model for the vortex shedding time period, a total of seven cases (Cases **A** ∼ **G**) was simulated (refer to table 1) at various Mach numbers and area ratios. The time history of stagnation pressure at the exit was Fourier transformed in each case, and the local peak corresponding to the shedding time scale was chosen in the frequency domain. Figures 10 and 11 plot the ratios of the shedding time period from DNS to the predicted time scale given by (5) at different Mach numbers and area ratios, respectively. These figures show that the averaged shedding time periods are within a factor of two of those predicted by the model. The underestimates of the time scale by the model are likely caused by inaccurate estimates of the vortex density and size as well as the induced velocity αu_1 to pinch off vortices. As discussed later, the absorption of circulation from the wall, λ, is relatively small ($\sim 10\%$) in the unforced cases.

STAGNATION PRESSURE LOSS FOR UNFORCED CASES

Next, the averaged stagnation pressure loss obtained from DNS is compared with the incompressible, inviscid ($\lambda = 0$) and fully-separated ($\overline{p_w} = p_1$) model described before. The Mach number and area ratio dependence is shown in figures 12 and 13, respectively. Although the model captures the trend, the deviation is somewhat inconsistent. In DNS we attempted to optimize the computational cost by choosing the minimum Reynolds numbers to generate vortex shedding flow patterns. Therefore, the difference of the Reynolds numbers may affect flow patterns, such as the structure and the convective velocity of vortices. Note that the stagnation pressure loss associated with viscous dissipation is the order of 10^{-3} or less in all cases.

The depths of the stagnation pressure troughs in Case **A** are $4 \sim 10\%$ (figure 9) and somewhat smaller than that of the Oseen vortex model ($\sim 11\%$) in figure 5. On the other hand, the convective velocity of the vortices in DNS is nearly half u_2 (detailed values of the model coefficients will be given in table 3 and discussed later), while that estimated based on the model is $0.67u_2$ (using (17) with $h_2/h_1 = 2$ and $h_3/h_1 = 5/4$). Hence, the troughs in DNS are wider than those predicted by the model. As a result, the unsteady part of the stagnation pressure loss is under-estimated by the model.

As mentioned in (22), the static pressure recovery provides a positive factor (i.e. $\overline{p_w} > p_1$) in the stagnation pressure recovery, which is ignored in the fully separated model. If we include this term, the model would under-estimate the stagnation pressure
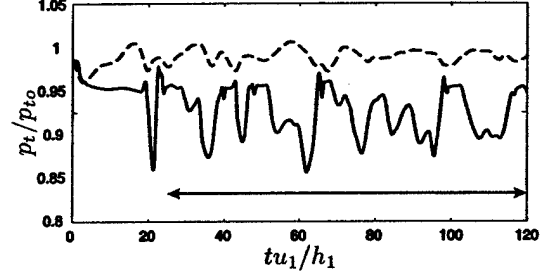

Figure 9: Time histories of stagnation pressure in Case **A**. Stagnation pressure was averaged over the cross section: − − −, inlet stagnation pressure ($x/h_1 = -2.$); ———, exit stagnation pressure ($x/h_1 = 3.$). $p_{to} \equiv (1 + \frac{\gamma-1}{2}M_1^2)^{\gamma/(\gamma-1)}p_1$.
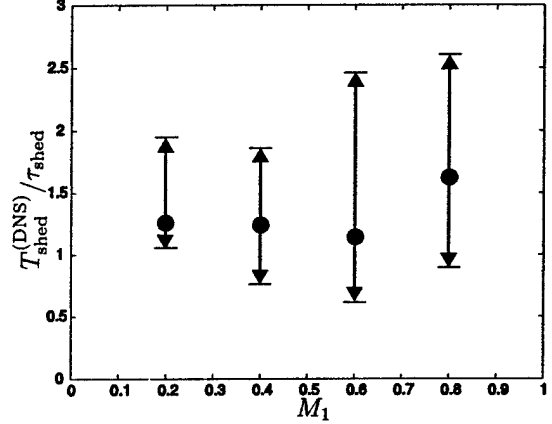

Figure 10: Mach number dependence of the vortex shedding period. Vortex shedding time periods from DNS are normalized by the shedding time scale given by (5). The results of Cases **B**, **C**, **A**, and **D** are plotted from left to right. • denotes the peak time period, and the arrows denote the minimum and maximum time periods measured from intervals between troughs.
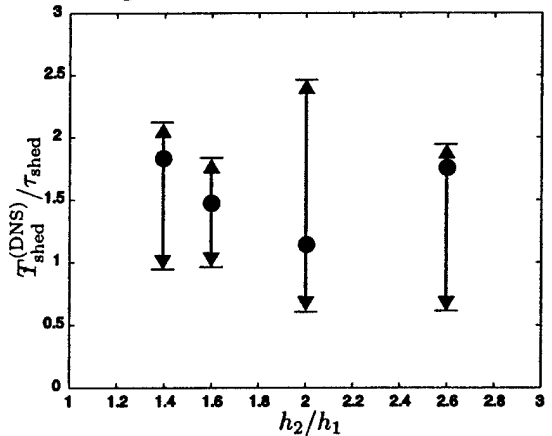

Figure 11: Area ratio dependence of the vortex shedding period. The results of Cases **E**, **F**, **A**, and **G** are plotted from left to right. Notation is the same as figure 10.

9

loss in most cases. In fact, this factor is partially canceled by the under-estimate of the unsteady part mentioned above.

Referring to figures 10 and 11, the stagnation pressure loss tends to exceed the prediction in figures 12 and 13 as the fluctuation of the shedding time period becomes wider (refer to the distances between the arrows in figures 10 and 11). When the accumulated circulation is clearly washed out due to the pinching-off process, the unsteady pattern approaches stationary and stagnation pressure is better restored.

To assess the viscous effect on the wall, we calculated the vorticity flux on the upper wall ($x/h_1 \in [-2, 3]$) for Case **A** and exhibit in figure 14. Referring to figure 8, it is clear that vorticity is mainly absorbed near the leading edge of the vortex. When the vortex convects downstream, the pressure on the wall $(p_2)_{\text{wall}}$ decreases; hence, vorticity is produced at the wall as derived from (22). The net rate of absorption in the time interval denoted in figure 9 is about 11%; thus, the viscous effect is relatively small in the unforced case.

PERIODIC MASS INJECTION

The series of figure 15 shows the evolution of the vorticity contour for a forced case (Case **L**, which corresponds to the optimum forcing frequency as shown later). Compared with the unforced case (figure 8), the size of the vortices is smaller and their convective velocity is higher in this case. Near the separation point, the next vortex is continuously generated and pinched off before it is fully developed. Thus, the periodic mass injection tends to reduce α and κ in (19) and suppresses the unsteady part of stagnation pressure loss.

Figures 16 and 17 compare the averaged static pressure field for the unforced (Case **A**) and forced (Case **L**) cases, respectively. They demonstrate that the reattachment point shifts upstream in the forced case although the apparent separation point does not move in figure 15. This helps static pressure recovery on the wall and lessens the steady part of stagnation pressure loss.

Figure 18 depicts the time histories of stagnation pressure at the inlet and exit for Case **L**. Compared to the unforced case (figure 9), these profiles clearly become periodic at the forcing frequency (i.e. frequency locking). Moreover, the forced case shows sharper stagnation pressure drops and a higher offset; namely, the convective velocity is increased and static pressure on the wall is restored.

Figure 19 compares the stagnation pressure recovery between the unforced and forced cases over a range of frequencies. Periodic mass injection pro-
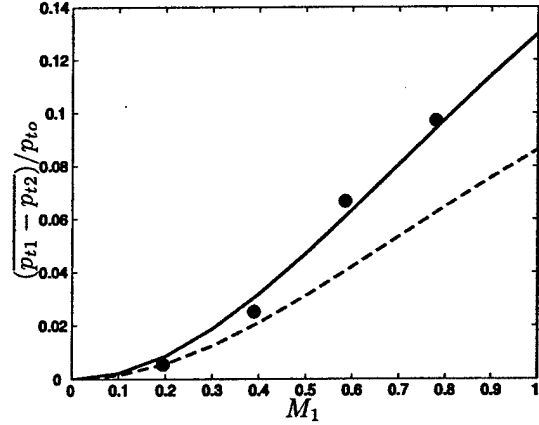

Figure 12: Mach number dependence of the stagnation pressure loss. Time averaged stagnation pressure loss calculated from DNS is compared with the fully separated model in the incompressible limit: ———, total stagnation pressure loss given by (19) ($\alpha = 1$, $\beta = 1$, $\lambda = 0$, $\overline{p_w} = p_1$, and $\kappa = 0.33$ are assumed); – – –, steady part given by (13); •, DNS results (Cases **B**, **C**, **A**, and **D** from left to right). The actual averaged inflow Mach numbers are plotted for DNS.
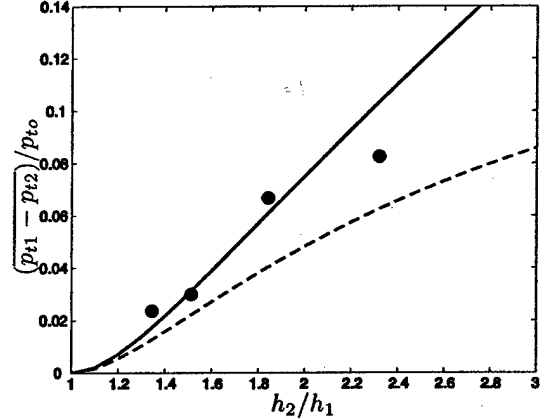

Figure 13: Area ratio dependence of the stagnation pressure loss. Notation is the same as figure 12. DNS results, Cases **E**, **F**, **A**, and **G**, are plotted from left to right. The actual area ratio between the inlet and the exit stations indicated in table 1 is used. $h_3 = \frac{1}{2}(\frac{h_1+h_2}{2} + h_2)$ is assumed to evaluate κ.
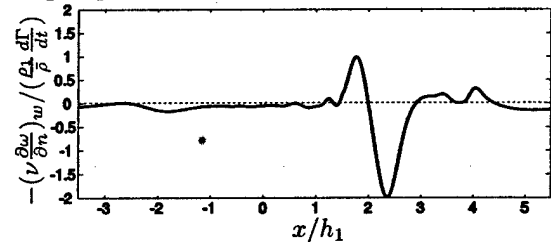

Figure 14: Instantaneous vorticity flux from the wall in Case **A**. Vorticity flux from the upper wall is calculated based on (21) at $tu_1/h_1 = 67.2$ in Case **A** (see figure 8). Production is taken to be positive, and absorption to be negative.
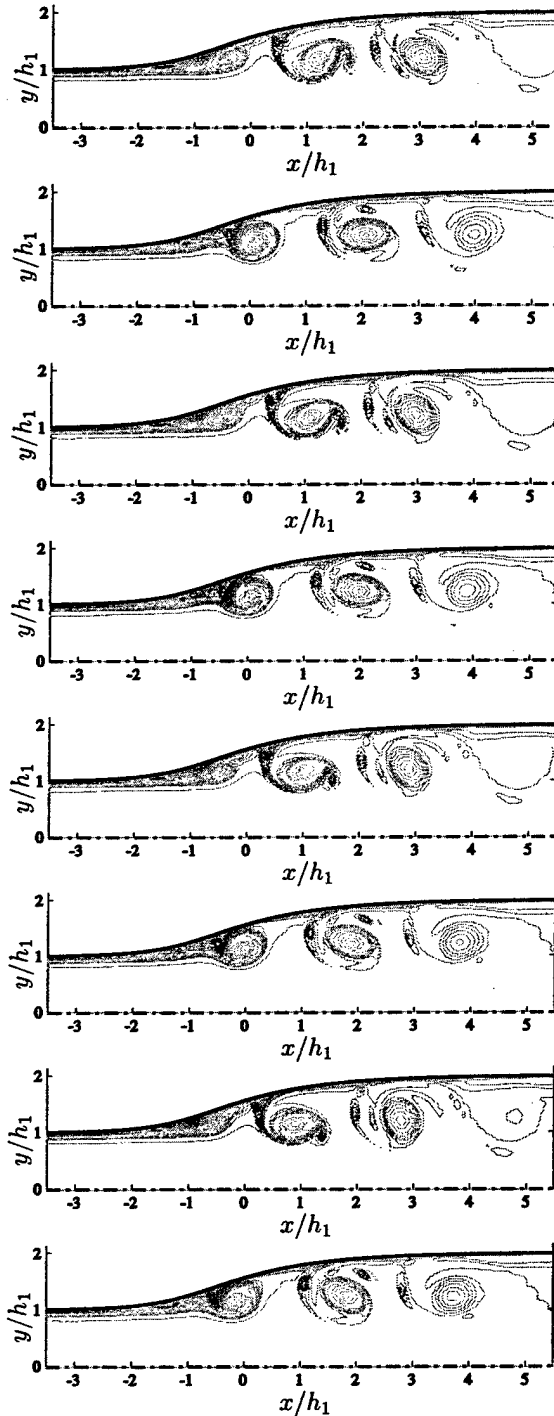
10

Figure 15: Vorticity evolution in a two-dimensional diffuser at the optimum forcing frequency ($\omega h_1/u_1 = 1.25$, Case **L**). Notation is the same as figure 8: $tu_1/h_1 = 57.6, 60.0, 62.4, 64.8, 67.2, 69.6, 72.0,$ and 74.4 from the top.

vides better stagnation pressure recovery to an appreciable degree ($2 \sim 4\%$) in all cases. (Note that the direct increase of stagnation pressure due to mass injection is approximately $\rho u_s^2 h_s/(2p_{to}h_1) \sim 2 \times 10^{-3}$). In particular, frequency locking, which is observed at nearly the natural shedding frequency or somewhat higher, results in the most substantial improvement in stagnation pressure recovery. At even higher frequencies, vortex pairing is observed, and the stagnation pressure recovery is deteriorated. An example of vortex pairing is displayed in figure 20.

The optimum frequency is slightly less than twice the natural shedding frequency. In fact, the order of this frequency agrees with the non-dimensional frequency of $F^+ \equiv fL/u_\infty \sim 1$ (L is a characteristic length and u_∞ the free-stream velocity, which we take here as $(h_2 - h_1)$ and u_1, respectively). This frequency scale is used in various applications (Seifert, Darabi, & Wygnanski 1996). Interestingly, even if the frequency locking occurs, the higher frequency does not necessarily lead to better performance.

These results also agree with the finding that periodic forcing is most effective when the vortex is reduced in size by a factor of one-third to unity as compared with the natural vortex size (Seifert, Darabi, & Wygnanski 1996; Seifert & Pack 1999). However, counter to the interpretation given in previous studies, the forcing mechanism is not directly related to instabilities of the shear layer near the separation point. As shown in figure 19, the most unstable frequency of the shear layer estimated from the linear stability analysis (the mean velocity profile is taken from $x/h_1 = -0.5$ in Case **A**) is found to be several times higher than the optimum frequency. In experiments, the most unstable frequency should be even higher as the boundary layer becomes thinner. Our theoretical discussion also implies that the local shear layer instability does not explicitly govern the forcing mechanism.

Table 3 shows various parameters associated with the model computed from DNS. The correlation between $\overline{p_{t2}}/\overline{p_{t1}}$ and λ demonstrates that the absorption of circulation helps improve stagnation pressure recovery. Even if no frequency locking occurs (Case **I**), the rate of absorption in the forced case is substantially higher than that in the unforced case; similarly, the stagnation pressure recovery is also higher in the forced cases. Recall that the mass injection in this study has always a non-negative momentum flux. In the optimum case (Case **L**), the rate of absorption is as much as 60%. As seen in figures 14, a small vortex generated near the separation point locally creates an adverse pressure gradient (see (21)) and helps absorb vorticity from the wall.
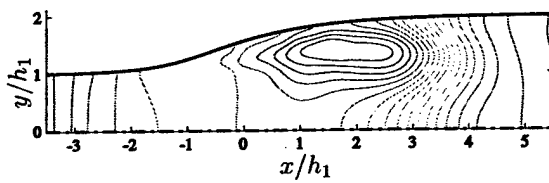
Figure 16: Time averaged pressure contour for the unforced case (Case **A**). Contour level: $\bar{p}_{\min}/p_1 = 1.00$, $\bar{p}_{\max}/p_1 = 1.16$ with the interval of $\Delta\bar{p}/p_1 = 0.01$.
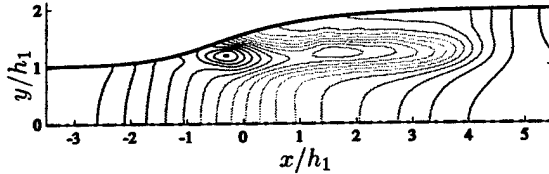

Figure 17: Time averaged pressure contour for the forced case (Case **L**). Notation is the same as figure 16.
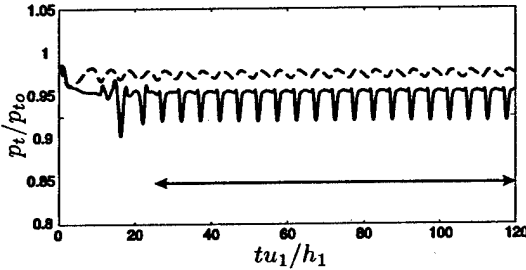

Figure 18: Time histories of stagnation pressure at the optimum forcing frequency ($\omega h_1/u_1 = 1.25$, Case **L**). Notation is the same as figure 9.
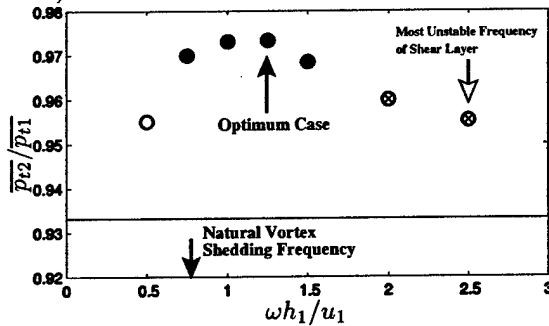

Figure 19: Comparison of the stagnation pressure recovery at different forcing frequencies. The ratios of the averaged stagnation pressures at the exit ($x/h_1 = 3.$) to the inlet ($x/h_1 = -2.$) are plotted (Cases **I** $\sim$ **O** from left to right). The horizontal line denotes the unforced case (Case **A**). ● indicates that frequency locking occurs, and ⊗ indicates that vortex pairing occurs although the vortices are pinched off at the forcing frequency.
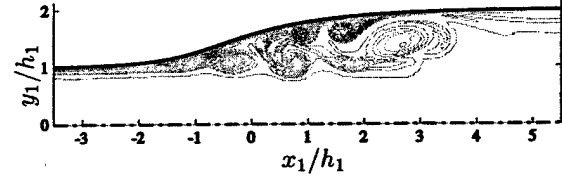

Figure 20: A snapshot of vortex pairing. Vorticity contours are drawn (Case **O**). Notation is the same as figure 8.

Case	$\omega h_1/u_1$	$\overline{p_{t2}}/\overline{p_{t1}}$	$\overline{p_w}/p_1$	λ
A	unforced	0.933	1.049	0.113
I	0.5	0.955	1.055	0.402
J	0.75	0.970	1.065	0.588
K	1.00	0.973	1.070	0.603
L	1.25	0.973	1.074	0.604
M	1.50	0.968	1.075	0.536
N	2.00	0.960	1.071	0.439
O	2.50	0.955	1.065	0.388

Case	α	β	$1 - \alpha\kappa$	h_3/h_1
A	1.154	0.837	0.531	1.325
I	0.920	0.886	0.578	1.180
J	0.690	1.045	0.678	1.097
K	0.547	0.986	0.771	1.163
L	0.452	0.936	0.782	1.237
M	0.378	1.025	0.746	1.271
N	0.519	0.920	0.663	1.301
O	0.664	1.000	0.557	1.252

Table 3: Frequency dependence of each parameter measured from DNS. $\overline{p_w}$ and λ were directly computed on the upper wall (using (21) for λ). α, β, and $(1 - \alpha\kappa)$ were calculated from three samples of vortices passing through the exit cross section ($x_1/h_1 = 3.$) for each case. A single vortex was defined as a simply supported region of the local vorticity up to 2% of the peak vorticity.

Attention should be paid to the rate of absorption, λ, and the convective velocity, $(1 - \alpha\kappa)$, which are lower in Case **M** than Case **L**. When a vortex is pinched off due to forcing, its center stays closer to the wall for a smaller vortex. In fact, h_3/h_1 measured in DNS demonstrates this trend. Hence, the convective velocity is reduced from (17), and the pressure deficit on the wall is enhanced, i.e. the rate of absorption is decreased from (22). This effect seems to provide an upper limit on the diminution of stagnation pressure loss with decreasing α. In the unforced case, vortices tend to be pinched off further downstream, and, in turn, the vortex center is again close to the wall regardless of the size of the vortex.
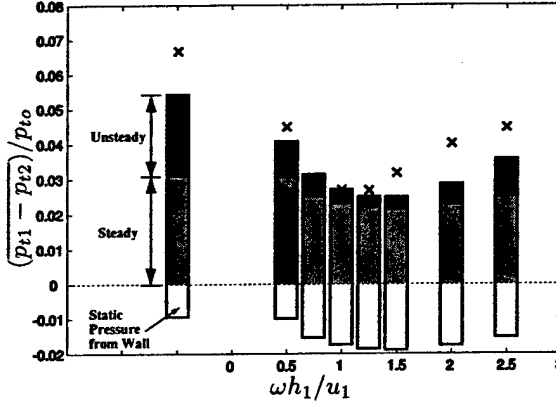
Finally, figure 21 depicts the estimated stagnation

Figure 21: Estimated stagnation pressure loss from each component. Each component of the stagnation pressure loss is displayed in a bar chart. Parameters in table 3 are substituted into (19). The actual total stagnation pressure directly computed from DNS is denoted by ×. The unforced case (Case **A**) is also plotted on the left.

pressure loss from each component in the model. It indicates that the unsteady part of the stagnation pressure loss is substantially reduced near the optimum frequency. As the forcing frequency is further increased (at $\omega h_1/u_1 = 2.0$ in Case **N**), α is nearly doubled due to vortex pairing. Likewise, at $\omega h_1/u_1 = 2.5$ in Case **O**, α is tripled or more due to multiple vortex pairings. Static pressure $\overline{p_w}/p_1$ is restored for smaller circulation of vortices, but this contribution is weaker than the unsteady part.

The under-estimates of the net stagnation pressure loss are presumably caused by the compressible effects as well as the inaccuracy of measurement for α and $(1 - \alpha\kappa)$, particularly when vortex parings occur (Cases **N** and **O**) or the flow pattern becomes fully unsteady (Cases **A** and **I**). In addition, counter-rotating vortices (small ones can be observed in figures 8 and 15), which are ignored in this chart, can deteriorate the stagnation pressure recovery as well.

CONCLUSIONS

A reduced order model which captures the vortex shedding phenomenon and estimates stagnation pressure loss in a diffuser is developed in two-dimensions. DNS is performed at various Mach numbers and area ratios to validate the model. The characteristic frequency of vortex shedding is successfully scaled by accounting for the net vorticity accumulation. Stagnation pressure loss is also estimated fairly well based on an incompressible flow although the unsteady part of the loss tends to be under-estimated compared with the DNS results.

To suppress the stagnation pressure loss, we introduce periodic mass injection to simulate a synthetic jet. Frequency locking occurs at nearly the natural vortex shedding frequency or somewhat higher where the most substantial improvement is achieved in stagnation pressure recovery (3 ~ 4%). Periodic injection continuously generates vortices downstream of the separation point. These vortices locally create an adverse pressure gradient and enhance the absorption of circulation from the wall.

The analyses based on the incompressible model together with the DNS results imply that the key to improve the stagnation pressure recovery is the following: (1) absorb more circulation from the wall (increase λ); (2) reduce circulation of one vortex (decrease α); (3) increase the convective velocity of vortices (decrease κ); (4) increase the static pressure recovery on the wall (increase $\overline{p_w}$). These parameters are not independent; in fact, three parameters, λ, α, and $\overline{p_w}$, tend to simultaneously shift to the preferable direction by increasing the forcing frequency until frequency locking breaks. Although the current model can give a crude estimate of α (and maybe κ), it cannot predict λ and $\overline{p_w}$. To actually estimate these parameters for forced cases, we need to analyze vortex dynamics in each specific flow geometry. Nonetheless, the DNS results show that the optimum frequency occurs at somewhat higher than the natural vortex shedding frequency, which is qualitatively consistent with the experimental facts.

It should be emphasized that this study focuses on the cases in which the separation point barely moves due to the forcing. For some applications the adverse pressure gradient is relatively gentle so that the mass injection can delay the separation point and provide better static pressure recovery. In fact, classical active flow control techniques, such as steady tangential blowing or boundary layer suction, try to attach the boundary layer. In those studies, the slope angle of the diffuser θ is considered to be an important parameter. However, the model developed in this study implies that the area ratio governs the large-scale flow unsteadiness for rapidly expanding diffusers. Furthermore, this study demonstrates that by pinching off vortices more frequently, we can suppress a substantial part of the unsteady stagnation pressure loss. As a result, the stagnation pressure recovery is much improved even though the boundary layer remains separated.

Although we have only simulated laminar diffuser flows, the boundary layer becomes turbulent under practical conditions. However, the model developed in this study is independent of the Reynolds number and boundary layer thickness, except that the rate

13

of absorption can change. This explains the experimental results that the peak frequency varies weakly with Reynolds numbers (Seifert & Pack 1999). We recognize that the model and DNS developed here lack several features of real diffuser flows. The most obvious limitation is the two-dimensionality although the results, particularly the forcing strategies, should still be commonly applicable to three-dimensional diffusers with spanwise coherent vortex shedding (c.f. Kaltenbach, *et al.* 1999).

ACKNOWLEDGMENTS

REFERENCES

Back, L. & Cuffel, R. 1982 Experimental investigation of turbulent wall-jets in the presence of adverse pressure gradients in a rectangular diffuser. Int. J. Heat Mass Transfer, **25**, 871–887.

Freund, J. B. 1997 Proposed inflow/outflow boundary condition for direct computation of aerodynamic sound. AIAA J. **35**, no.4, 740-742.

Gharib, M., Rambod, E., & Shariff, K. 1998 A universal time scale for vortex ring formation. J. Fluid Mech. **360**, 121–140.

Glezer, A. & Amitay, M. 2002 Synthetic jets. Annu. Rev. Fluid Mech. **34**, 503–529.

Hamstra, J. W., Miller, D. N., Truax, P. P., Anderson, B. A., & Wendt, B. J. 2000 Active inlet flow control technology demonstration. in International Congress of the Aeronautical Sciences. ICAS-2000-6.11.2.

Kaltenbach, H.-J., Fatica, M., Mittal, R., Lund, T. S., & Moin, P. 1999 Study of flow in a planar asymmetric diffuser using large-eddy simulation. J. Fluid Mech. **390**, 151–185.

Koumoutsakos, P., Leonard, A., & Pepin, F. 1994 Boundary conditions for viscous vortex methods. J. Comput. Phys. **113**, 52–61.

Lele, S. K. 1992 Compact finite difference schemes with spectral-like resolution. J. Comput. Phys., **103**, no.1, 16-42.

MacMartin, D. G., Murray, R. M., Verma, A., & Paduano, J. D. 2001 Active control of integrated inlet/compression systems: Initial results. ASME Fluid Engng. FEDSM 2001-18275.

Narayanan, S. & Banaszuk, A. 2003 Experimental study of a novel active separation control approach. AIAA paper, AIAA 2003-0060.

Nicoll, W. B. & Ramaprian, B. R. 1970 Performance of conical diffusers with annular injection at inlet. Trans. ASME: J. Basic Engng. **92**, no.4, 827–835.

Nishi, M., Yoshida, K., & Morimitsu, K. 1998 Control of separation in a conical diffuser by vortex generator jets. JSME: Int. J. Series B, **41**, no.1, 233–238.

Oseen, C. W. 1912 Über Wirbelbewegung in einer reibenden Flüssigkeit. Ark. f. Mat. Astron. Fys. **7**, 14.

Pierrehumbert, R. T. 1980 A family of steady, translating vortex pairs with distributed vorticity. J. Fluid Mech. **99**, pt.1, 129–144.

Poinsot, T. J. & Lele, S. K. 1992 Boundary conditions for direct simulations of compressible viscous flows. J. Comput. Phys. **101**, no.1, 104–129.

Rao, D. M. 1971 A method of flow stabilisation with high pressure recovery in short, conical diffusers. J. Roy. Aeronaut. Soc. Technical notes, **75**, 336–339.

Reneau, L. R., Johnston, J. P., & Kline, S. J. 1967 Performance and design of straight, two-dimensional diffusers. Trans. ASME: J. Basic Engng. **89**, no.4, 141–150.

Saffman, P. G. 1992 *Vortex Dynamics*, Cambridge University Press.

Salmon, J. T., Bogar, T. J., & Sajben, M. 1983 Laser Doppler velocimeter measurements in unsteady, separated, transonic diffuser flows. AIAA J. **21**, no.12, 1690–1697.

Seifert, A., Darabi, A., & Wygnanski, I. 1996 Delay of airfoil stall by periodic excitation. J. Aircraft, **33**, no.4, 691–698.

Seifert, A. & Pack, L. G. 1999 Oscillatory control of separation at high Reynolds Numbers. AIAA J. **37**, no.9, 1062–1071.

Schlichting, H. 1960 *Boundary Layer Theory*, 4th ed. (translated by J. Kestin), McGraw-Hill.

Welsh, M. C. 1976 Flow control in wide-angled conical diffusers. Trans. ASME: J. Fluids Engng. **98**, no.4, 728–735.

STALL MARGIN IMPROVEMENT USING FEEDBACK CONTROL TO MITIGATE INLET DISTORTION UNSTEADINESS

Zack Warfield   **James D. Paduano**
Massachusetts Institute of Technology

Douglas G. MacMartin
California Institute of Technology

April 23, 2002

Abstract

Experimental control of unsteadiness due to inlet flow separation is described. The control scheme is presented as part of an overall architecture for integrated inlet/compressor control that attempts to mitigate both the source of separation in serpentine inlets and the effects on compressor operability. Experimental results on unsteadiness reduction at the aero-dynamic interface plane are used as inputs to a compressor model to determine the effect on compressor stability, showing the benefits of such control vis-à-vis steady-state flow reattachment.

1.0 Introduction

In an airplane propulsion system, the inlet and compressor work together to convert the free-stream flow into high pressure, low speed air for combustion. During high-speed flight, the inlet is responsible for decelerating the inlet flow to match the compressor's requirements, and for efficient conversion of the free-stream flow energy (dynamic pressure) into static pressure. New demands are being placed on aircraft inlet designs, which require that they be S-shaped and have much shorter length-to-diameter ratios than ever before (see Figure 1).

These demands are typically in conflict with engine performance, creating a difficult design challenge. If the inlet diffuses the flow too aggressively or the ductwork turns too sharply, separation will result. The requirement for clean deceleration is quantified by the area-averaged total pressure recovery at or near the compressor face. Further requirements derive from the compressor's sensitivity to non-uniformity of the inlet flow; large non-uniformity reduces the stability of the compressor and compromises safe operation of the engine. A competing requirement is the desire to keep the inlet duct as short as possible, both to reduce wetted area and overall vehicle weight.

Figure 1 – Typical serpentine inlet.

The design trade between inlet duct length and overall propulsion system efficiency is especially important in UAV configurations whose overall length is set by the propulsion system length. Studies at Northrop Grumman indicate that reducing the inlet length while retaining it's total pressure recovery properties can allow gross take-off weight to be reduced by up to 13%, significantly reducing life-cycle costs.

In this paper, we perform initial investigations into a concept for integrated flow control of the inlet-compressor combination. The overall goal of control is to provide airframe designers with a way to shorten inlets while retaining or improving the performance and robustness of the inlet-compressor combination. Performance of the inlet-compressor combination is determined by the overall compression efficiency, which is a combination of the total pressure recovery and the compressor pressure ratio and/or efficiency. Robustness is determined by the compressor 'stall margin' that must be maintained to insure that the compressor will not stall when inlet disturbances (gusts, hot gas ingestion, sideslip transients) are introduced in flight. Stall margin is defined in various

1

ways, all of which characterize the distance on the mass-flow/pressure-rise map of the compressor between the operating line of the compressor and the stall/surge line, i.e. the line beyond which the compressor becomes unstable.

Robustness is one of the driving requirements for compression system design, and as such can significantly impact achievable performance. Current design practice roughly doubles the stall/surge margin to insure that distorted inlet flow does not destabilize the compressor[1]. In addition, conditions at the aerodynamic interface plane (AIP, a cross-sectional plane of the inlet duct roughly one radius upstream of the compressor) must meet required levels of both steady-state and unsteady distortion. Exceeding these levels compromises both delivered pressure rise and efficiency (performance) and compressor stability[2].

This description suggests various avenues for application of flow control. One such avenue is to use flow control to maintain attached flow in the inlet beyond the natural stall point, allowing more aggressive curvature and/or diffusion. Such Inlet flow control is being investigated by a variety of researchers[3-5]. Alternatively, the compressor can be made to withstand the higher levels of distortion that result from separation[6-8] (although this approach would not recover the total pressure loss associated with separation). In addition, flow control to either minimize the level of *unsteadiness*, or increase the compressor's tolerance for unsteadiness, would allow the compressor to operate at a lower stall margin, which translates into higher compressor pressure ratio and possibly higher efficiency.

In this paper, an integrated control approach is described, and initial feasibility studies for this approach presented. Figure 2 shows the control system architecture. Flow is injected in an optimized, unsteady manner at strategically located points along the diffuser to delay separation. If implemented properly, this part of the system will convert the compressor-face pressure profile from a circumferential distortion profile to a so-called 'smile' distortion (that is, a combination of circumferential and radial distortion), achieving an inlet pressure recovery level similar to that of less aggressive inlets. Past research indicates that although the steady-state pressure recovery will be good, significant levels of unsteadiness may still remain in the flow. Furthermore, smile distortions can be as detrimental to compressor stability as circumferential distortions. Therefore, a second

flow control component must be integrated into the system. This component consists of compressor face actuation to mitigate unsteadiness and augment the stability of the compressor. Recent research indicates that properly implemented compressor-face actuation can allow a compressor to operate at lower-than-normal stall margin levels with larger perturbations[6-8]. Thus the combined benefit of this integrated control component is expected to be significant.

Figure 2 – Integrated Inlet-Compressor Control System Architecture

A full-scale experimental program is underway to demonstrate the control system architecture described above. The first phase of the program, described in this paper, is aimed at verifying (to the extent possible in our current experiment) the compressor-face actuation portion of the architecture. We will demonstrate that unsteadiness born at the separation point of an aggressive, high-subsonic diffuser can be reduced through actuation at the compressor face location. Furthermore, we will show that the level of reduction achieved is significant from the perspective of its impact on compressor stability.

2.0 Research Scope and Experimental Setup

The scope of this paper is limited by the current experimental setup. Figure 3 shows the scaled inlet being tested. This inlet is part of a Northrop Grumman 1/6th-scale UAV model. In Figure 3, the inlet lip has been removed and replaced with a bellmouth, to allow testing at

2

conditions that mimic up-and-away flight. The highly three-dimensional inlet has severe enough internal curvatures that, at high mass flows, the flow separates from the upper surface.

Also shown in Figure 3 are the actuators that will be used for this study. Due to space limitations in this small-scale apparatus, and because there is no compressor in the setup, compressor-face actuation is emulated by simple mass injection. Four, 400 Hz valves driven by Moog actuators are mounted circumferentially around the downstream cylindrical duct. The total mass flow capability of these valves is 0.35 lb/sec, or 11% of the 3.2 lb/sec mass flow at which experiments for this paper were conducted. Actuators are modulated in parallel (all actuators move simultaneously), so only one-dimensional actuation effects will be studied here. Mass injected at the approximate location of the compressor face has a mass-displacement effect similar to that in transonic compressors with downstream choking; in such compressors any mass added at the compressor face must be accommodated by a mass flow reduction upstream. Therefore a one-dimensional volumetric source accurately represents compressor-face actuation in one dimension.

Unsteady measurements of various kinds were taken to establish the character of the flow unsteadiness. These included hot film measurements near the separation point, unsteady total pressure measurements near the AIP, and wall static pressure. A 40-probe rake was also installed at the compressor face to more fully characterize unsteadiness, but the can in which the rake was mounted was too long to allow control studies while these measurements were being taken. Data acquisition and control was performed by a PC-based DSP system, capable of 100 kHz throughput. In most cases a data rate of 20kHz was used, with 10kHz anti-alias filtering.

One limitation of the small scale testing results from the large size of the actuators relative to the size of the inlet. The acoustic delay between actuation and the AIP is larger than the convection delay between the separation point (where the unsteadiness is created) and the AIP. Thus, in a full scale implementation, hot-film sensors at the separation point could be used to provide feedforward information to the actuation. However, at the smaller scale tested here, this 'advance information' about the unsteadiness is unavailable. Controllability can be demonstrated at this scale using *narrowband* feedback of unsteadiness, but the bandwidth over which reductions are obtained will be limited by the time delay. This bandwidth limit will not be present in a full scale implementation.

3.0 Control Demonstration Development

This section describes the control law development cycle we used to partially demonstrate our active control concept. First, we define a representative output for the system to be controlled; this will be the feedback quantity to be minimized. Next, we establish the dynamical link between the actuator inputs and the sensed output/performance parameter, by performing simple system identification experiments. Finally, a feedback loop will be designed and the behavior of the system under active control will be demonstrated.

3.1 Derivation of representative output to control

Since our primary goal is to reduce that part of inlet flow unsteadiness that impacts compressor stability, and since only a single actuator (1D downstream injection modulation) will be studied, we first desire to establish a single parameter input to the control law. This input can be based on multiple measurements, combined to create a 'bulk parameter' characterizing the signal that the controller should try to minimize.

3

After considering various options, it was decided that the outputs that would be considered for control would be derived from the ARP 1420 guidelines[1] for characterizing inlet distortion at the AIP. These guidelines describe methods to quantify the magnitude, extent, and location of a single-lobed total pressure distortion (the type of distortion that dominates a serpentine inlet). Figure 4 shows the quantities derived from a set of annulus-averaged total pressure probes located at 45 degree intervals around the compressor annulus. The total

sinusoidal excitation testing of the apparatus. These transfer functions, which have been fit with low-order polynomial transfer functions, establish three main facts. First, they show that the system is indeed a controllable input-output system, and that the bulk parameters are suitable parameters to attempt to control. Second, they show that the dynamics are dominated primarily by delays, resulting in a linear phase drop-off as a function of frequency. The experimentally determined values of delay are consistent with the sum of the computational time delay, the
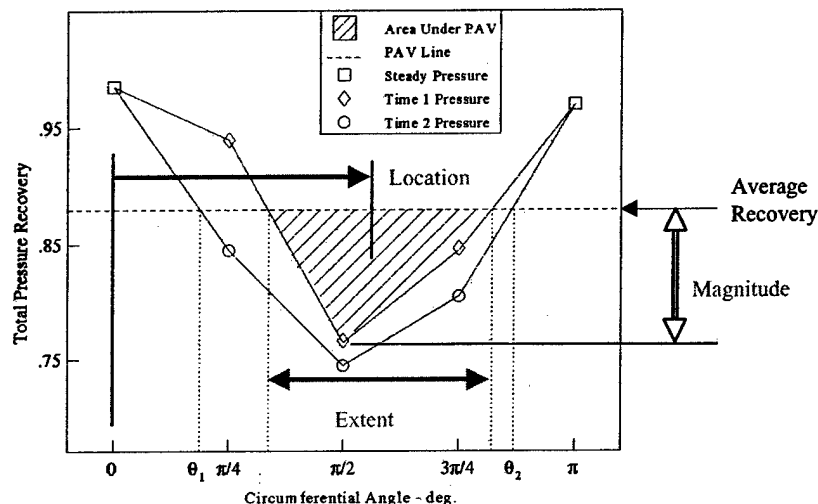

Figure 4 – ARP 1420 parameters characterizing single-lobed inlet distortion

pressure averaged around the circumference serves as the baseline from which the extent, magnitude, and position of the distortion are measured. Our innovation is to use the *unsteady* values of these measurements as feedback quantities for our active control scheme. For this study, we will determine, through compressor stability modeling, the impact of unsteadiness of these parameters on compressor stability. We will use this modeling as a measure of success of our active control implementation, whose goal will be to minimize one or more of the parameters (magnitude, extent, and location).

3.2 Input-Output Properties
Having established our system input (one-dimensional mass flow injection) and various outputs, we proceed to characterize the transfer function from the input to outputs. Figure 5 shows the transfer functions obtained by

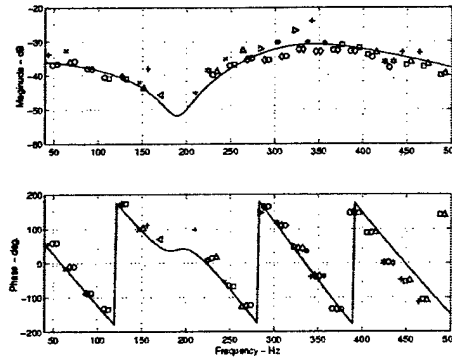servo time delay, and the acoustic time delay

4
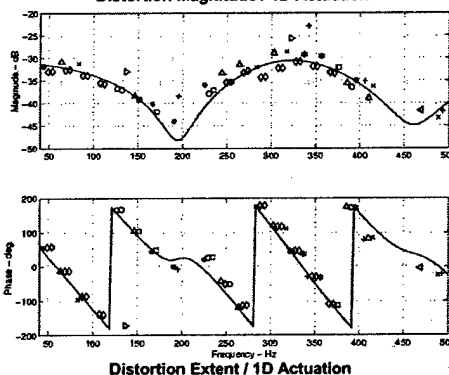
Figure 5 – Transfer Functions from Actuator Command Voltage to Magnitude (Left) and Extent (Right) Bulk Parameters

from the actuators to the sensors. This time delay limits the achievable bandwidth of control in this experiment. Finally, although not shown here, these experiments established that distortion position is not controllable from 1D actuation; therefore it will be dropped as a system output in the remainder of the discussion.

Based on these transfer functions, control laws can be designed that reduce the unsteadiness of the bulk parameters. Because this analysis and control technique relies on a perturbation approach, steady-state reduction of the unsteadiness was not considered feasible. The fact that the actuators primarily launch 1D acoustic waves to have their effect supports this conclusion. Therefore, as we discussed in the introduction, in future work we will rely on actuation local to the separation itself to reduce the steady-state distortion.

It is also important to note that compressor-face actuation, when it is implemented in the ultimate, full-scale system, will have both similarities and differences with the experiment being performed here. The primary difference is that the actuation will affect the compressor's local pressure rise characteristics, so that in addition to launching acoustic waves, it will have the potential to raise or lower the compressor's pressure rise in response to fluctuations in incoming total pressure. This will be a more direct way to reduce the impact of incoming disturbances on compressor stability. The primary similarity between this experiment and the full-scale experiment is that the spatial character of the inputs to the controller will be similar (although perhaps derived from different sensors) and that the ability to absorb or

counteract unsteadiness in this experiment gives us confidence that the ultimate system will have reasonable controllability properties.

3.3 Control law development

The simplest experiment that demonstrates the effectiveness of feedback control to reduce unsteadiness uses a narrow-band, phase-tuned filter to concentrate control effort in a desired frequency range. This narrow-band approach attempts to reduce the unsteadiness of the closed-loop system output over a specified frequency range. This allows us to demonstrate that actuation is effective in various frequency bands, without requiring detailed control law design and experimental tuning. As noted earlier, the full-scale control architecture will include feedforward information from the separation region that will overcome the bandwidth constraint imposed by the time delay.

The compensator used for narrow-band control is a second order transfer function with a lightly damped pole at the frequency of interest. The transfer function can be written as follows:

$$H(s) = \frac{k}{s^2 + 2\xi\omega_0 s + \omega_0^2} e^{-s\tau} \qquad (1)$$

The complex pole pair represented by the above, $s_{1,2} = -\xi\omega_0 \pm j\omega_0\sqrt{1-\xi^2}$, determines the frequency center value and bandwidth over which the actuators will attempt to exert control. The purpose of the pure time delay is to add phase lag to the filter transfer function; this is necessary to properly compensate for input-output phase lag in the transfer functions of Figure 5. The time delay and resonator gain k are experimentally optimized for various values of center frequency. These values have been checked against the theoretical values one would derive from the transfer functions in Figure 5, and found to be consistent[9].

4.0 Experimental Results

Control tests were performed at 100Hz and 300Hz, where the feedback parameter was either distortion magnitude or distortion extent. Gain and time delay of the filter *H(s)* were experimentally optimized, and spectra were taken with control on and control off. Figure 6 shows the results of these experiments. The classic trade-off between attenuation at the center frequency of a notch filter, and excitation of frequencies above and below the notch, can be

5

interpret them in the context of compressor stability, we perform compressor simulations using the experimental
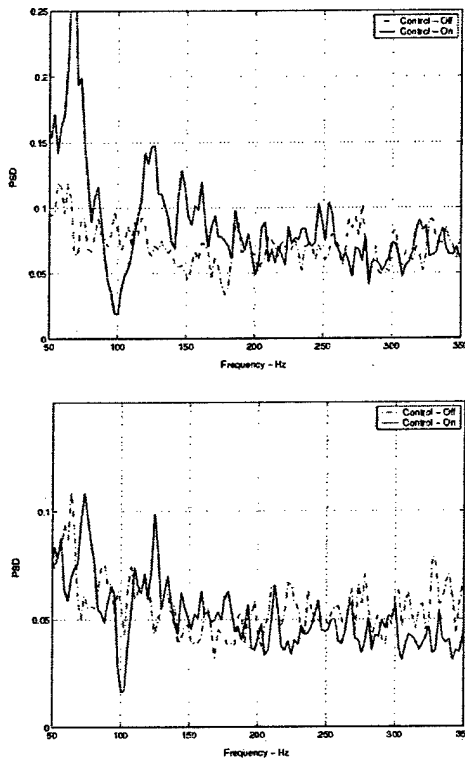

Figure 6a – Narrow-band control results for band-pass frequency of 100 Hz. Top – feedback of distortion magnitude, bottom – feedback of distortion extent
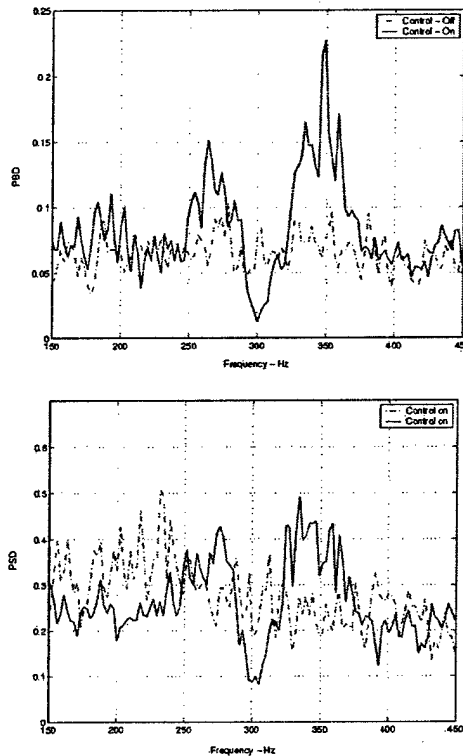

Figure 6b – Narrow-band control results for band-pass frequency of 300 Hz. Top– feedback of distortion magnitude, bottom – feedback of distortion extent

seen in all of these pictures; in some cases the result is so severe as to render the feedback control unacceptable. In all cases the controller was able to reduce distortion unsteadiness at the center frequency by 50% or more.

5.0 Interpretation of Experimental Results via Nonlinear Rotating Stall Simulation

The ability to reduce the distortion unsteadiness in a narrow band, while perhaps exacerbating it at nearby frequencies, is only useful if it results in an increase in compressor stall margin. It is in fact quite likely that this will be the case, as the compressor is most sensitive to perturbations at or near the rotating stall frequency. So, by reducing the unsteadiness in the rotating stall frequency range, we hope to improve compressor stability. To analyze the experimental results and

behavior of the unsteadiness as inputs to the simulation. The compressor operating range with unsteadiness will be determined, and by this means the control effectiveness judged.

The simulation we employ is an implementation of the Moore-Greitzer compression system model[10-12], which captures both rotating stall and surge behavior of compression systems. A significant body of previous work exists on the effect of *steady state* inlet distortion on compressor stability[1,2,13,14], but much less research has been done on the impact of unsteady inlet distortion. However, the nonlinear simulation is entirely capable of capturing the response of the compressor to non-

6

uniform, unsteady inlet total pressure profiles. The primary limitations of this model in the context of distortion modeling are as follows:

1) The model is incompressible, so that Mach number effects are not modeled. Because the primary physics associated with rotating stall are incompressible, this is not considered a major limitation.

2) The model is 2-dimensional, with the axial and circumferential directions being the dimensions modeled. Thus radial distortion is not properly modeled. This is a more severe deficiency that we address here by taking the worst-case radial location from our measurements. Thus our estimates will be somewhat conservative, and do not distinguish between various forms of radial distortion that might be created by actuation.

3) The current implementation does not directly account for implementation of active control at the compressor face. This limitation is addressed through an approximate method outlined below, and will be removed in future studies.

To utilize our compressor simulation to determine the effect of active control, we first consider the relative impact of the measured steady-state and unsteady distortion from the experiments described above. This is accomplished by taking the worst-case radial location from the 40-probe distortion measurements, and determining the mean distortion level at this radial location. This mean distortion level is then subtracted from the raw measurements to form the unsteady part of the distortion. Thus the total pressure profile is decomposed into a time-mean, non-uniform component, and a time-unsteady, circumferentially uniform (in the mean) component:

$$P_t(\theta,t) = \overline{P_t}(\theta) + \delta P(\theta,t), \qquad (2)$$

where the overbar indicates time average, and the time average of δP is zero. Next, for each component and for their sum, the compressor simulation is run with experimental total pressure as an input. Another input to the compressor simulation is throttle position, which determines the compressor operating point. The throttle is commanded to slowly close during the simulation, which causes the compressor operating point to move from the nominal position toward the stall line. The mass flow and pressure rise at which the compressor stalls is

then recorded. This numerical experiment exactly mimics real world compressor operability experiments. This test is run using several data sets, and the results are analyzed statistically.

One additional variable must be varied during these simulations to fully investigate the active control problem. In some experiments, the data acquired exhibits a frequency peak in the 500-600 Hz range. This frequency peak appears to be associated with vortex shedding at the separation point. In the full implementation of the control law, this frequency will most likely be locked to the pulsation frequency of the actuators at the separation point. In either case, the frequency of the spectral peak with respect to the rotating stall natural frequency is an important parameter that governs compressor stability, as we will show presently. To model a range of excitation frequencies using the limited experimental data sets available at the time of this writing, we simply change the time scale in the experimental data. This is equivalent to running the compressor at various rotor RPMs, since time is non-dimensionalized by the rotor frequency in our analysis. The fundamental mode of rotating stall is at about 30-40% of the rotor RPM, so this is the frequency range at which we expect the compressor to be especially sensitive to disturbances.

Figure 7 shows the results for experimental data taken at 3.1 lb/sec. A generic 3-stage compressor is used in this model, to determine the trends and relative importance of the various governing parameters. Figure 7 shows that indeed there is an effect of unsteadiness on compressor stall point, and that the steady and unsteady effects are roughly additive. In this particular example, unsteadiness has a larger impact than steady-state distortion, but this may
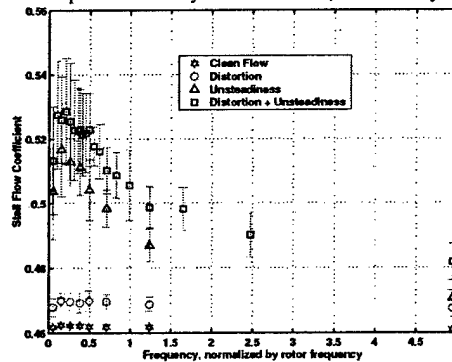
be an artifact of either the particular distortion pattern in the inlet we are considering, or an over-estimation of the unsteady component of the distortion. The higher sensitivity near the rotating stall frequency, on the other hand, is expected to be a generic trend: when the excitation frequency is near the rotating stall frequency, it will excite the least stable rotating stall mode, causing instability to occur at a higher mass flow than usual. The error bars are plus or minus one standard deviation, based on a sample of 16 runs.

The data from Figure 7 can be converted into a stall margin, by assuming that the compressor operating point is at the maximum efficiency point of the compressor. The stall margin is computed as follows, based on standard stall margin computation methods:

**(operating flow coeff. – stall flow coefficient)
+ (stall pressure rise – operating pressure rise)**

Using this convention, Figure 7 can be converted into Figure 8 (the error bars have been removed for clarity.) This figure shows that the loss in stall margin is approximately 35% based on our calculation method. The fact that this is similar to the stall margin typically budgeted for distortion (see for instance ARP 1420[1]) in real compressors gives us confidence that the analysis is exhibiting the right orders of magnitude, as well as the right trends with the parameters being studied.
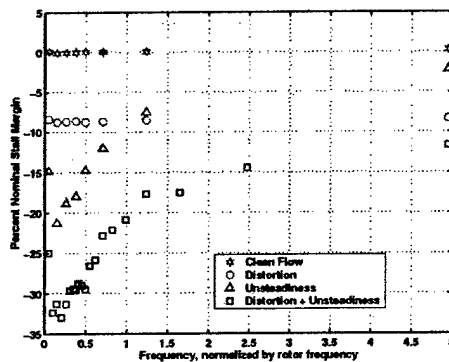
Finally, we consider the effect of control on the compressor stall margin. The same numerical experiments already described were re-executed, with various types of control implemented through the mechanism of filtering the experimental data. Although this is a somewhat artificial method for accounting for the effects of control, it is the quickest way to look at a broad range of conditions. Actual implementation of control laws in the nonlinear simulation will be the next step in our research.

Various levels of control are considered in Figure 9. Open loop results from Figure 8, for combined distortion and unsteadiness, are shown in the plot for reference. The experimentally achieved narrow-band attenuation is next applied, centering the attenuation notch in the region where rotating stall is most strongly excited, that is, a non-dimensional frequency range of 0.3 to 0.4. A typical aeroengine compressor operates in the 50 to 300 Hz frequency range, depending on the size of the engine, so the bandwidth represented by this frequency range is 5 to 30 Hz, consistent with the results obtained in Figures 5 and 6. Both the attenuation and the amplification of signals are modeled by the approach we used.

The triangles in Figure 9 show the results of this notch filter. An average of about 5 percent improvement in stall margin is obtained, enough to increase the compressor operating pressure ratio somewhat, but perhaps not enough to warrant the expense and complexity of an active control system. If the bandwidth of the attenuating filter could be increased to cover the
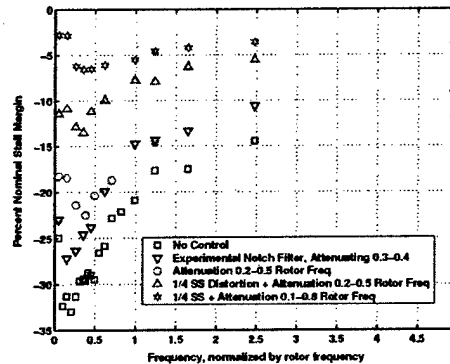

8

Figure 9 – Effect of various levels of control on stall margin

range 0.2 to 0.5 of the rotor frequency, the worst-case stall margin could be improved by about 10%. This is shown by the circles in Figure 9.

If we next assume that separation point actuation is used to reduce the distortion level to 1/4th it's original level, then the performance is further improved, improving the stall margin by approximately 20%. This is shown by the triangles in Figure 9, and perhaps represents a feasible level of distortion tolerance to be obtained by integrated inlet/compression system control.

6.0 Summary and Discussion

This paper reviews a concept for combined inlet-compression system control that is currently being studied. Preliminary experimental results, combined with nonlinear rotating stall simulations, were used to assess the expected effectiveness of the control concept. Narrow-band attenuation of ARP-1420 parameters that affect compressor stability was achieved experimentally, demonstrating that such control is possible. The environment in which these tests were performed was non-ideal, due to the small scale of the test facility, which increased the bandwidth and time delay requirements on the control system. Better performance is expected in full-scale experiments currently being planned, which will use feedforward information from the separation region to overcome time delay issues. The experiments were also approximate because the actuation available was one-dimensional, even though the distortion parameters, and the actuators that will be available on the full-scale experiment, are non-uniformly distributed circumferentially. Therefore, we believe that the experimental performance obtained is a conservative estimate of the improvement that can be obtained in practice.

One conclusion that we have reached by looking at these results is that if the steady-state distortion is not ameliorated to some extent, either by separation point actuation or by steady-state control at the compressor face, unsteadiness reduction alone is probably not sufficient to make the approach viable. Likewise, unsteadiness is a major player in compressor stability, and cannot be ignored when considering the effectiveness of any technique at improving the pressure recovery of an inlet. Finally, we feel that the dynamical modeling method that we used to here to assess the effect of inlet distortion on compressor stability is a more accurate method to assess installation effects than methods currently being used by industry. It is a physics-based approach that takes into account the compressor's dynamical response to distortion, rather than a correlation-based approach. We hope to further validate this approach to inlet-engine matching through full scale testing at NASA Glenn.

8.0 References

1. ARP 1420, "Aerospace recommended practice: Gas turbine engine inlet flow distortion guidelines"
2. Longley, J. P., 1980, "Measured and Predicted Effects of Inlet Distortion on Axial Compressors", ASME Paper 90-GT-214, Proc. 1990 ASME Turbo Expo, June 11-14, Brussels, Belgium.
3. Hamstra, J.W., Miller, D.N., Truax, P. P., Anderson, B. A. and Wendt, B. J., "Active Inlet Flow Control Technology Demonstration", *The Aeronautical Journal*, 2000, pp. 473-479.
4. Ng, W. F. and Burdisso, R. A., "Active Acoustic and Flow Control for Aeropropulsion", *AIAA Aerospace Sciences Conference*, AIAA 2001-0220.
5. MacMartin, D.G., Verma, A. Murray, R.M. and Paduano, J.D., "Active Control of Integrated Inlet/Compression Systems: Initial Results", *ASME Fluids Engineering Division Summer Meeting*, New Orleans, May 2001. ASME FEDSM2001-18275.
6. van Schalkwyk, C. M., Paduano, J. D., Greitzer, E. M., and Epstein, A. H., 1997, "Active Stabilization of Axial Compressors with Circumferential Inlet Distortion," 97-GT-279, ," *ASME J. of Turbomachinery*, July, Vol. 120, No. 3, pp. 431-439.
7. Spakovsky, Z., Weigl, H. J., Van Schalkwyk, C. M., Paduano, J. D., Bright, M. M., Strazisar,

T., and Suder, K., "Rotating Stall Control in a High-Speed Stage with Inlet Distortion Part II: Circumferential Distortion" *Journal of Turbomachinery*, Vol. 121, July 1999.

8. Bright et. al, NASA tests.

9. Warfield, Z. W., "THESIS"

10. Moore, F. K. and Greitzer, E. M., 1986, "A Theory of Post-Stall Transients in Axial Compression Systems, Part I - Development of Equations, and Part II - Application, " ASME J. of Engineering for Gas Turbines and Power, Vol. 108, pp. 68-97.

11. Longley, J. P., 1993, "A Review of Non-Steady Flow Models for Compressor Stability," ASME Paper 93-GT-17, 1993 ASME Turbo Expo, Cincinnati, May 24-27.

12. Paduano, J. D., Greitzer, E. M., and Epstein, A. H., 2001, "Compression System Stability and Active Control," *Annual Review of Fluid Mechanics, Vol. 33, pp491-517*

13. Hynes, T. P. and Greitzer, E. M. 1987, "A Method of Assessing Effects of Circumferential Flow Distortion on Compressor Stability," *ASME J. of Turbomachinery*, Vol. 109, pp. 371-379.

14. Chue, R., Hynes, T. P., Greitzer, E. M., Tan, C. S., and Longley, J. P., 1989, "Calculations of Inlet Distortion Induced Compressor Flow Field Instability," *International J. of Heat & Fluid Flow*, September, Vol. 10, No. 3, pp. 211-223..

Design of an Actively Stabilized Near-Isentropic Supersonic Inlet

Umair Ahsun[*]   Ali Merchant[**]   James D. Paduano[**]   Mark Drela[***]

Department of Aeronautics and Astronautics
Massachusetts Institute of Technology, Cambridge, MA

Abstract

A 2D Mach 2.2 internal compression inlet with 97% total pressure recovery has been designed using viscid-inviscid computational tools. Losses are minimized by careful boundary layer management combined with shape design for weak shocks. The resulting inlet has reduced stability to unstart in the face of atmospheric and engine-born disturbances, necessitating the use of an active stabilization bleed system that recovers the disturbance-rejection capabilities required of modern inlets. Atmospheric disturbances that the inlet may encounter during supersonic flight are characterized. Two separate physical mechanisms for unstart are identified, and active control algorithms to prevent these forms of unstart are designed and demonstrated using 1D and 2D unsteady Euler simulations. The resulting actively stabilized inlet can withstand flight velocity, temperature, and angle of attack perturbations consistent with atmospheric flight.

Introduction and Motivation

An inlet acts as an interface between the free stream and an aircraft propulsion system. The flow is decelerated to a Mach number required at the compressor face, and energy is recovered in the form of increased pressure. Although it is

Figure 1: A 2D Euler calculation of a high recovery internal compression inlet showing shock wave structure.

theoretically possible to design an inlet to achieve virtually isentropic compression of the supersonic flow to sonic conditions, in practice this may be impossible to realize due to flow disturbances and geometric variations in the inlet. Because shock waves contribute to loss in pressure recovery, a more realistic design is one that can achieve near-isentropic internal compression with a number of weak oblique shock waves, and a weak terminal normal shock just behind the throat to decelerate the flow to subsonic conditions. Such a design is shown in Figure 1.

The potential pay-off of such a high recovery inlet is significant. In the case of a typical 100,000 lb supersonic aircraft, such as the Quiet Supersonic Platform, improving the inlet recovery to 97% in cruise could increase the range by approximately 500 nautical miles.[1] In addition, as most supersonic inlets require bleed on the order of 8% of the inlet flow to stabilize the terminal shock and control boundary layer separation, the reduced bleed requirement of the present design, primarily due to the weaker shock waves, may lead to additional gains at the system level.

The price of achieving a high recovery is reduced stability to flow disturbances. These include atmospheric disturbances entering the inlet and engine borne disturbances traveling upstream from the compressor face. These disturbances can cause a normal shock blow out event known as "inlet unstart."[2] Inlet unstart results in a severe increase in drag due to flow spillage and formation of a strong shock wave at the inlet lip. In addition, the accompanying decrease in mass flow through the inlet may also result in engine surge.[2]

We can define the unstart tolerance of the inlet as the magnitude of the disturbance that can be tolerated without unstart. The tradeoff between inlet stability and pressure recovery is primarily a consequence of the strength of the terminal normal shock.[3] Thus, an inlet with a stronger normal shock, achieved by positioning the
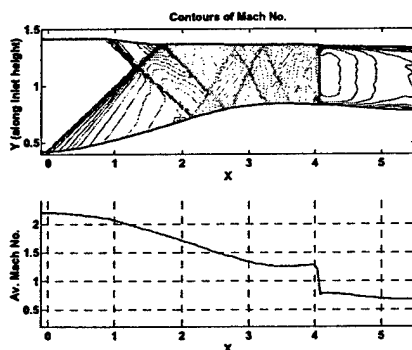
1

normal shock sufficiently downstream of the throat, or alternatively by increasing the throat area ratio, will have a lower pressure recovery, but will be more resistant to unstart under operational perturbations. Similarly, weakening the terminal normal shock will enhance the pressure recovery, but simultaneously make the terminal shock more susceptible to moving under operational perturbations, thus lowering the unstart tolerance of the inlet.

In this paper, the 2D design and performance of an enhanced recovery inlet are presented. This is followed by a detailed discussion on the development of the active stabilization system for the inlet which includes: 1) characterizing and quantifying the atmospheric disturbances, 2) quantifying the dynamic behavior of the inlet subject to atmospheric disturbances for the design and analysis of a control system, and 3) development of the control architecture and control law. Lastly, application of the active stabilization system illustrating its effectiveness in attenuating atmospheric disturbances is presented.

Design of Enhanced Recovery Inlet

A steady inviscid-viscous solver, based on the MISES solver approach, was used to design the 2D profile and study the performance of the inlet.[4] The inviscid flow is represented by the axisymmetric Euler equations that are discretized on a streamline grid in a conservative form. The inviscid equations are strongly coupled with a two-equation integral boundary formulation via the displacement thickness concept. The fully coupled system of non-linear equations is solved simultaneously by a global Newton-Raphson method. A boundary layer suction model developed by Merchant was implemented in the code.[5] Comparison between the predictions of this suction model and experimental data has been carried out for a variety of subsonic and supersonic flows. The model assumes that the suction slot is flush with the inlet surface. Suction is applied by specifying a mass fraction, slot location, and slot width on the inlet geometry.

Inlet Design Approach
The primary consideration in the design of the inlet geometry is the pressure recovery. The losses that are considered in the present design

are due to the oblique shock system in the supersonic portion of the inlet, the terminal normal shock, and the viscous boundary layers. The supersonic portion of the inlet can be made nearly isentropic at design conditions, which implies that the compression of the flow has to be gradual, and the length of the inlet cannot be overly constrained. On the other hand, since the inlet length has an impact on the viscous boundary layer loss, a long inlet may not lead to the best recovery. A shorter inlet will also be lighter and preferable from the airframe-inlet integration point-of-view.

The critical Mach numbers in the inlet are at the throat, just upstream of the terminal normal shock, and at the exit (compressor face). The normal shock Mach number contributes to the loss through the inviscid normal shock loss and through shock-boundary layer interaction. The shock strength as well as inviscid shock loss increases rapidly for shock Mach numbers greater than about 1.3. The choice of shock Mach number constrains the throat Mach number such that

$$1 < M_{throat} < M_{shock}. \qquad (1)$$

Clearly, for stable operation the throat Mach number must be greater than unity for supersonic inflow, and since supersonic flow must accelerate in a diverging duct to obey the area velocity relationship for an isentropic flow, the shock Mach number must be greater than the throat Mach number. The difference between M_{throat} and M_{shock} determines the range of inlet Mach number variation that can be accepted by the inlet in the absence of control for stable operation, and therefore affects the static stability of the inlet. From these considerations, a throat Mach number of 1.25 and shock Mach number of 1.27 were selected to meet the performance requirements while minimizing the bleed requirements.

Based on the inlet Mach numbers for current fan and compressor designs, which typically range between 0.5 to 0.65, an exit Mach number of 0.6 was chosen for the current design study. The inlet shape between the shock location and the exit plane was designed to achieve continuously decreasing pressure gradient in order to minimize the boundary layer growth at the exit plane.

2

Figure 2 shows the 2D profile of the inlet. The length to height ratio of the inlet is 5.5. The ramp angle on the lower surface is 7° and the wedge angle on the upper surface is 4°. The upper surface is staggered with respect to the lower surface in order to cancel the compression waves emanating from these surfaces. The upper wedge angle was included in the design and calculations, since the real inlet is expected to have some finite thickness, and a top-mounted configuration on the aircraft is expected.
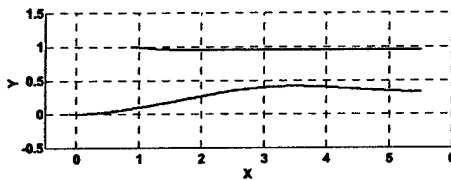
Figure 2: Enhanced recovery internal comp-ression inlet 2D geometry.

Bleed Configuration

The inlet bleed configuration consists of a supersonic control bleed and two normal shock boundary layer control bleeds. The steady value of the supersonic control bleed is 1% of the inlet mass flow, and it is modulated ±1% from its nominal value for active control. The bleed slot is positioned approximately one throat height upstream of the throat in order to meet the minimum time delay requirements of the active control system. This position also coincides with location where the oblique shock from the upper surface wedge impinges on the lower surface. This enables some degree of cancellation of the oblique shock reflection when the bleed is modulated. In addition to the supersonic bleed, two subsonic bleeds are located on the upper and lower surfaces just downstream of the normal shock location. The steady values of the lower and upper bleeds are 1% and 2% of the inlet mass flow. These bleeds serve a two-fold purpose: 1) reducing the boundary layer thick-ness critical for achieving the high pressure recovery, and 2) stabilize the shock in the face of incoming atmospheric and compressor face disturbances. The lower surface bleed is increased up to 2% for active control. The resulting total steady bleed requirement for the inlet is 4% of the inlet mass flow.

Atmospheric Disturbance Characterization

Although mechanisms such as aircraft maneuvers, back pressure perturbations due to engine transients, etc. can cause the inlet to unstart, atmospheric turbulence is the least predictable, and therefore the most important factor in avoiding the inlet unstarts.[3] In order to design an effective control system for the inlet, it is imperative to quantify the range and types of atmospheric disturbances encountered during nominal operation. The detailed derivations of the atmospheric disturbance models are discussed in Tank. [6, 7]

During supersonic flight, the inlet may encounter velocity and temperature perturbations ranging from the macroscale (size greater than few hundred kilometers) through the mesoscale (from few hundred km to tens of km) up to the microscale (tens of km to few cm). The scales imply a horizontal distance over which the disturbance parameter, such as the velocity, changes by its own order of magnitude. For the purpose of quantitatively expressing the disturbances we can treat them as quasi-steady, which means, as the inlet is flying through the disturbances, they are stationery for an observer not moving with respect to the atmosphere. Using the stationarity assumption, the atmospheric disturbances can be described statistically in terms of their power spectral density (PSD) functions. In the micro and meso scales the 3D turbulence is isotropic, and we can use Kolmogorov's spectrum for turbulence as follows:

$$S_t(k) = \alpha_t \varepsilon^{2/3} k^{-5/3} \qquad (2)$$

Here, the subscript t denotes a type of disturbance, ε is the eddy dissipation rate, k is the wave number, and α_t is a constant for each type of disturbance given by:

$\alpha_l = 0.15$ (longitudinal or forward wind velocity gust, dimensionless)
$\alpha_v = 0.2$ (vertical or up wind velocity gust, dimensionless)
$\alpha_T = 0.39$ (temperature disturbance, $°K^2 s^2 m^{-2}$)

Data indicates that the −5/3 law spectral behavior described above extends uninterrupted to an outer scale disturbance wavelength of around 400 km.[6] Thus we see that for a study of the
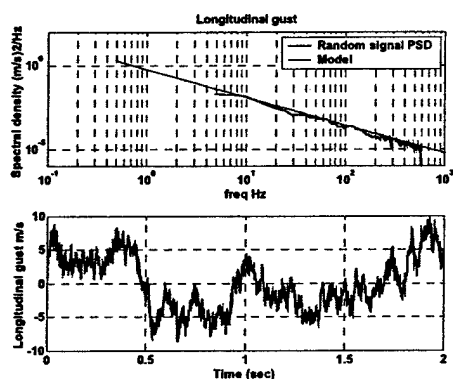
3

Figure 3: Forward velocity gust time history and spectrum for an aircraft flying at Mach 2.2 at altitude of 60000 ft (worst case value of ε).

effect of atmospheric disturbances on inlets only the eddy dissipation rate sets the spectral intensity over the entire frequency range of interest. The eddy dissipation rate is a function of the terrain, altitude, latitude, and time of the year. A typical value for ε is 2.0×10^{-5} m^{2}s^{-3} and can vary as much as a factor of 10.

Using the given model spectra for different atmospheric disturbance, a Fourier series method can be used for the generation of a random time series that has the same spectra as the atmospheric disturbances.[8] A typical output along with the relevant spectrum is shown in Figure 3.

The atmospheric disturbances affecting the inlet can be characterized in terms of four independent components: isothermal longitudinal gust, isothermal vertical gust with and without a forebody, and temperature gust. Angle of attack changes can be expressed to first order in terms of the isothermal vertical gust. Also, for this study only the case with forebody is considered since it is relevant to the aircraft-inlet configuration of interest. These disturbance components are assumed to appear as plane waves at the inlet lip and travel through the inlet in the form of characteristic waves. Using the linearized analysis for a quasi-1D flow through the inlet these waves can be expressed as a superposition of fast acoustic waves $J+$, traveling with a speed of $u+a$, slow acoustic waves $J-$, traveling with a speed of $u-a$, and entropy waves traveling with speed u. These variables are defined as:

$$J^+ = u + \frac{2a}{\gamma - 1} \qquad (3)$$

$$J^- = u - \frac{2a}{\gamma - 1} \qquad (4)$$

$$s = pv^\gamma \qquad (5)$$

Here, u is local flow speed, a is the local speed of sound. s is the entropy, p is the pressure, v is the specific volume, and γ is the ratio of specific heats. The atmospheric disturbances are converted into the characteristic form, since the characteristic or "canonical" forms of the disturbances are directly applicable for the control law design.

Using the definition of characteristic variables and the Prandtl-Meyer wave relation for the expansion waves, we can write the transformation between the atmospheric variables and the canonical variables as:

$$
\begin{bmatrix} \Delta J+ \\ \Delta J- \\ \Delta s \end{bmatrix} =
\begin{bmatrix}
1 & \dfrac{M_\infty - 1}{\sqrt{M_\infty^2 - 1}} & \dfrac{\gamma R}{(\gamma - 1)a_\infty} \\[2ex]
1 & -\dfrac{M_\infty + 1}{\sqrt{M_\infty^2 - 1}} & -\dfrac{\gamma R}{(\gamma - 1)a_\infty} \\[2ex]
0 & 0 & \dfrac{\gamma R}{\rho_\infty^{\gamma - 1}}
\end{bmatrix}
\begin{bmatrix} \Delta u \\ \Delta v \\ \Delta T \end{bmatrix} \qquad (6)
$$

The transformation matrix shows an interesting relation that a temperature perturbation impacts all the three canonical perturbations at the inlet lip.

Modification of disturbance spectra by Mach/velocity hold and ramp-control

Atmospheric disturbances having very large wavelengths in the macroscale regions can exhibit large variations in gust velocities as discussed above. From the point of view of inlet control we can assume that these large-scale disturbances (> 6-20 km or frequencies below 0.03 to 0.1 Hz) will be absorbed by the aircraft velocity hold system. We can also envision a ramp control system in the inlet, which can modify the area properties of the inlet depending on the engine demand and atmospheric turbulence to avoid unstart. The inlet active control system will therefore be subject to the atmospheric disturbance spectra attenuated by the vehicle velocity hold system and the inlet

4

ramp control system. Assuming a slew rate of approximately 60°/sec for the ramp-control system, a cut-off frequency of around 0.33 radians/sec for the Mach/velocity hold system, which are typical values for supersonic aircraft in the same weight class, modified spectra can be obtained for the characteristic perturbations at the inlet lip. An example of a modified spectrum is shown in Figure 4.
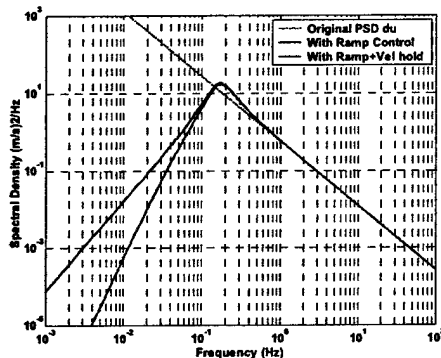

Figure 4: Modified spectrum for a longitudinal velocity gust with ramp control and velocity hold.

The maximum frequency of interest for the inlet disturbance rejection control system can be calculated from this modified spectrum. This is defined as the frequency that gives 99% of the spectral energy. For this particular spectrum, the maximum frequency is approximately 18 Hz. Thus, frequencies up to 18 Hz contribute 99% of the energy in the disturbance while higher frequencies only contribute the remaining 1%. From the point of view of inlet control system, only frequencies up to 20 Hz are considered. On the lower side of the modified spectrum, we can see that frequencies below 0.01 Hz are cut off by the ramp control and velocity hold systems. Thus, the range of frequencies of interest in the study of control system effectiveness is from 0.01 Hz to 20 Hz for the full-scale aircraft. This results in non-dimensional frequencies ranging from 4.4×10^{-5} to 0.1. The frequency is non-dimensionalized by the inlet stagnation speed of sound and the inlet height at the forward lip.

It should be noted that the effective gain of the ramp and velocity/Mach hold systems is not infinity, so for very low frequencies we may not get the roll-off seen in Figure 4. The atmospheric spectra also do not obey the –5/3 law for very low frequencies, but instead overestimate the energy compared to the actual measurements of

the disturbances.[7] Although a flattened spectrum is obtained at very low frequencies, we can safely assume that the disturbance energy is sufficiently attenuated at these low frequencies, and has a negligible impact on the inlet stability.

Inlet Unstart Mechanisms

The inlet can unstart via two distinct mechanisms, 1) motion of the terminal normal shock from a stable position downstream of the throat to an unstable position upstream of the throat, and 2) formation of a new unstable normal shock upstream of the throat.

The first mechanism is initiated by disturbances that directly affect the shock, such as reflection of fast waves from the exit boundary and entropy disturbances. Figure 10a and 10c illustrate the effect of these disturbances on the shock motion. The persistence of these disturbances over time can cause the shock to move upstream of the throat leading to unstart. Such an event is shown in Figure 5.
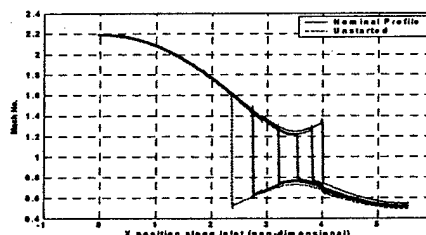

Figure 5: Mach number profiles for different normal shock locations. Shock is moving towards the inlet lip due to an incoming atmospheric disturbance. Unstart due to shock motion.

The second mechanism of unstart is caused by the strong impact of the slow acoustic wave disturbance J^-. This has a much stronger effect on the throat Mach number compared to the shock motion itself. Thus, when a pulse of slow acoustic wave disturbance of a sufficient magnitude reaches the throat, it can unchoke the throat ($M_{throat}<1$) while having virtually no impact on the stable normal shock downstream of the throat. Unchoking the throat therefore results in formation of an unstable shock downstream of the throat leading to unstart. Figure 6 illustrates this unstart mechanism. Formation of an unstable second normal shock is clearly seen in the Mach contours and the averaged Mach number profile.
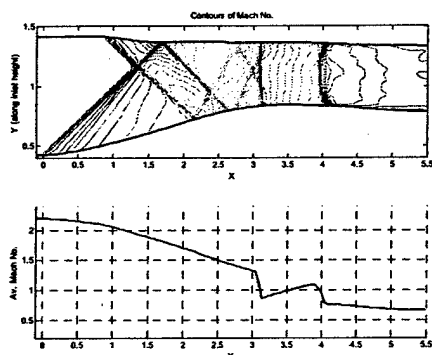
5

Figure 6: Contours of Mach number for the unstarting inlet due to new shock formation at the throat.

Dynamic Characterization of the Inlet

The dynamic behavior of the inlet was analyzed using unsteady quasi-1D and 2D numerical solvers. The solvers utilize a second order accurate finite volume scheme for spatial discretization. Stabilization and shock capturing are enabled using Roe's scheme. A four stage Runge-Kutta method is used to time march the solution. Boundary conditions are applied using Riemann invariants. The inlet boundary conditions were modified to impose the canonical atmospheric disturbances described above. The conservation laws were modified to include the effect of unsteady mass addition or removal in the simulation.

The unsteady numerical codes were embedded in Simulink and integrated into MATLAB to generate routines with the help of which different transfer functions could be generated in order to develop and analyze different control schemes. A block diagram of the Simulink model (called S-function) of the inlet is shown in Figure 7. As shown in Figure 7, the inlet can be excited with canonical atmospheric disturbances, characteristic disturbances, and bleed variations.

Frequency Response Study
Using the Simulink model, a detailed frequency response study was conducted for both quasi-1D and 2D cases. The geometry used for the 2D study was modified with a viscous correction obtained from the steady viscous-inviscid design
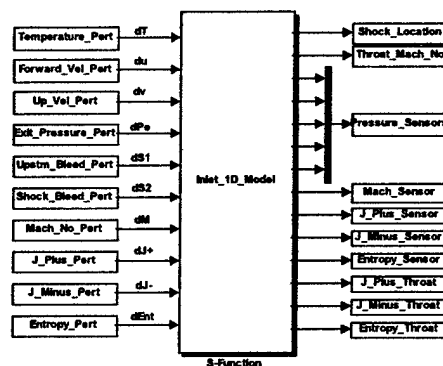

Figure 7: Quasi-1D (and 2D) unsteady Simulink Model of the inlet.

code described above. The area variation for the quasi-1D study was created by matching the area ratio of the 2D geometry at the inlet, the throat, and the exit. These critical areas were blended using cosine shape functions.

Figures 8a, b, and c present a comparison in the amplification of the characteristic disturbances for the quasi-1D and the area averaged 2D cases. This demonstrates that the quasi-1D model, especially in the low frequency range, adequately represents the dynamic behavior of the inlet. Thus, for the purpose of designing the control laws for the inlet, we can utilize quasi-1D unsteady model in the range of the frequencies of interest.

In Figure 8a we can see that the effect of J^+ on the throat Mach number diminishes at higher frequencies. In contrast, Figure 8b and c show that the effect of J^- remains essentially unchanged in the frequency range of interest, and the effect of entropy on the throat Mach number increases with frequency. The implication of these results is that J^- and entropy fluctuations have a greater impact than J^+ on the throat Mach number. Although the throat Mach number amplification of J^+ and roll off at higher frequency might suggest a negligible impact on unstart tolerance, J^+ has a significant impact on the shock motion.
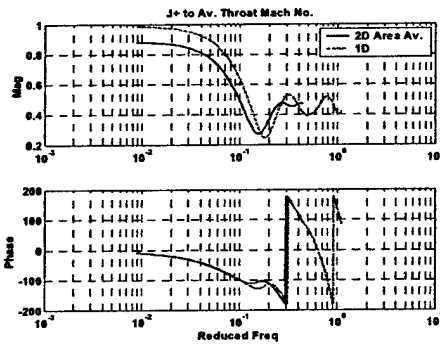
6

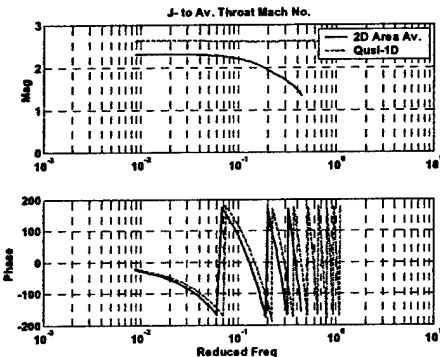**Figure 8a: Frequency response of the throat Mach number to fast acoustic wave J^+ perturbations.**

Figure 8b: Frequency response of the throat Mach number to slow acoustic wave J^- perturbations.
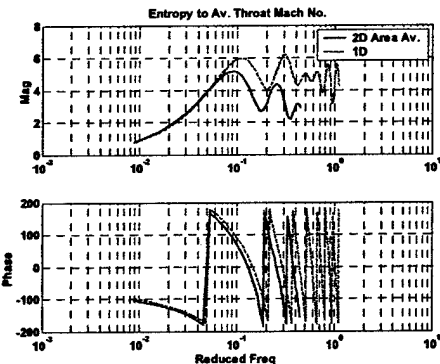

Figure 8c: Frequency response of the throat Mach number to entropy perturbations.

Figure 9 shows that the effect of bleed on the throat Mach number is essentially constant over the frequency range of interest. The effect of bleed primarily isentropic and is composed of J^+ and J^- perturbations.
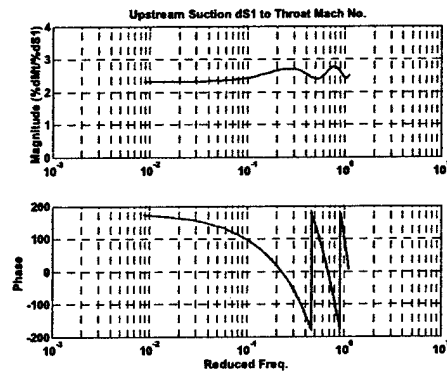

Figure 9: Frequency response of the throat Mach number to upstream bleed perturbations.

Normal shock motion as a function of different parameters have been studied via simplified linearized models that capture the shock dynamics with reasonable accuracy.[9] Analyzing the acoustic reflection and transmission properties of the normal shocks in ducts is crucial to understanding the shock motion.[10, 11] MacMartin has derived an ODE that captures the shock dynamics with reasonable accuracy.[12] The model shows that the transmission coefficient of upstream fast acoustic disturbances, or J^+, is nearly unity. Therefore, J^+ disturbances effectively pass through the shock with negligible effect on shock motion. However, from the large signal transfer function obtained in this study (Figure 10a), we can see that the shock is strongly affected by the J^+ perturbations.
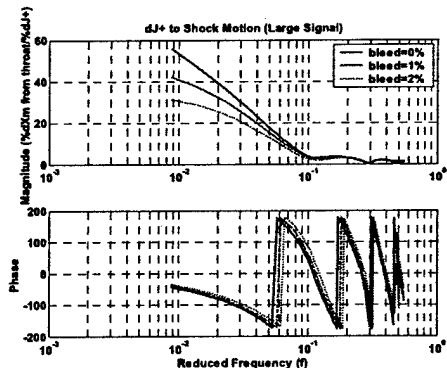

Figure 10a: Shock motion response to fast acoustic wave J^+ perturbations.

In comparison, the response of the shock motion to J^- and entropy perturbations, shown in Figures
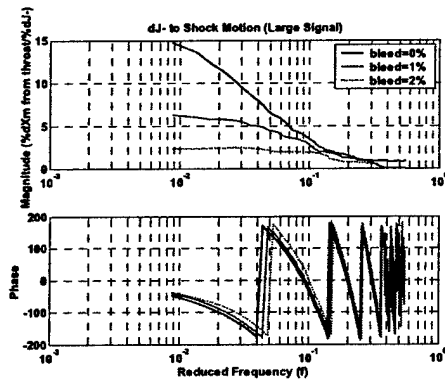
7

Figure 10b: Shock motion response to slow acoustic wave J^- perturbations.
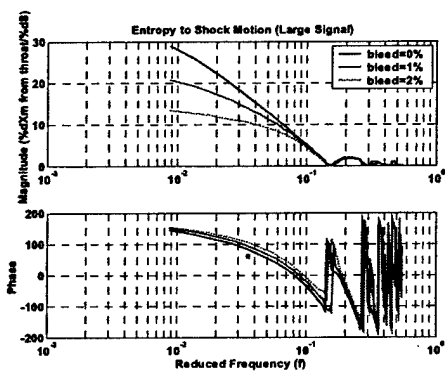

Figure 10c: Shock motion response to slow acoustic wave J^- perturbations.

10b and c is substantially smaller. This can be explained in terms of the exit boundary condition used in the generation of the frequency response plots.

The inlet and compressor are coupled in a real operating environment, and in order to capture the detailed behavior of this inlet-engine interaction, an accurate Compressor-Face Boundary Condition (CFBC) has to be utilized. There have been a number of studies to create simplified models for the prediction of unsteady CFBC.[13,14] Sajben has presented a simplified model for the computation of transmission and reflection coefficients accounting for compressor configuration and Mach number.[14] His results show that for different compressor configurations and Mach numbers the reflection coefficient can vary widely from -1 to 1. The constant exit pressure boundary condition used in the present study corresponds to the worst-case scenario of a reflection coefficient of -1. Since transmission coefficient for the fast wave J^+ through the shock is unity, the disturbance

travels unattenuated to the exit boundary causing a reflection that has a strong effect on the shock position.

Bandwidth Requirements of the Actuator

An important parameter from the point of view of the control system design is the bandwidth requirements of the control system and actuator. It can be seen from the transfer function plots (Figures 8a-c) of the atmospheric disturbances that the inlet has a flat response over reduced frequencies up to 1 for slow waves. The inlet amplifies the entropy perturbations at higher frequencies. Thus, it is clear that the atmospheric perturbation cut-off, rather than the inlet itself, sets the bandwidth requirement. From the previous section it is clear that most of the atmospheric turbulence energy is concentrated at lower frequencies. This suggests that a dimensional frequency of around 25 Hz (corresponding to a non-dimensional frequency of approximately 0.11) is the upper cut-off as far as the atmospheric perturbations are concerned. The bleed actuator must therefore have at least this bandwidth in order to cancel the affects of atmospheric perturbations.

Control Architecture

The dynamic response of the inlet shows that, in the range of the frequencies of interest, the quasi-1D and area averaged 2D transfer functions are almost identical, and in particular, the low frequency response of the inlet is represented to a good approximation by quasi-1D simulation. Motivated by this observation, the control architecture design is based on the quasi-1D simulation results, as it is easier and simpler to design the control laws with the quasi-1D simulation, and then test and verify the control laws in the 2D simulation. The control laws are divided into two distinct parts in order to address the unstart mechanisms discussed in the previous sections, namely the throat Mach number control and shock motion control.

Throat Mach Number Control

The atmospheric disturbances can increase or decrease the throat Mach number significantly. Both the positive and negative variations are undesirable and must be controlled to enhance the stability of the inlet. The upstream bleed actuation is used to control the throat Mach number.
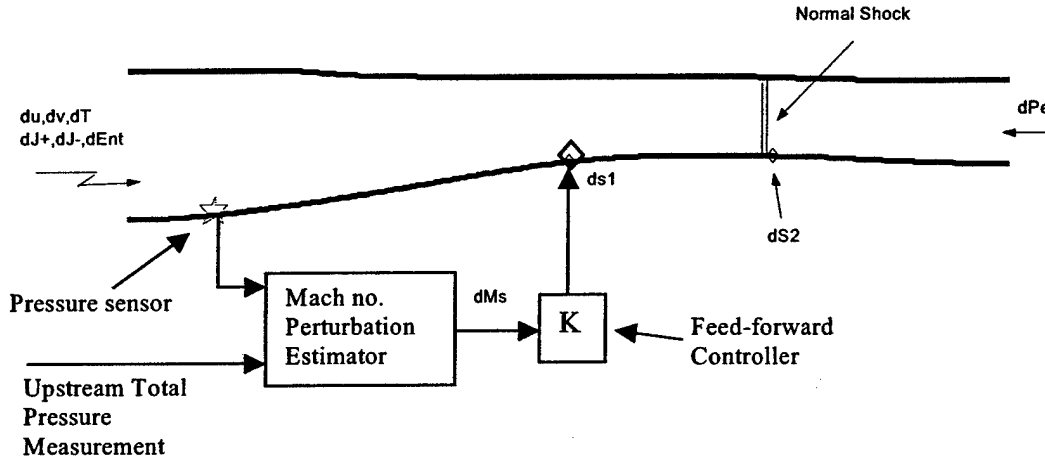
8

Figure 11: Feed-forward control law architecture, for throat mach number control, based on Mach number estimation at the sensor.

Perturbations in the upstream bleed result in mostly slow acoustic waves, and from the speed of propagation of the slow acoustic waves, we can estimate a time delay of approximately 2.0 non-dimensional units for the control perturbations to reach the throat. This implies that we can only use a feedback control of the throat Mach number at very low frequencies. Thus, in order to cover a wider range of frequencies in the incoming disturbance spectrum, we need to use a feed-forward control system. The feed-forward controller presented here is based directly on the atmospheric disturbance quantities, although the canonical disturbances, J^-, J^+, and entropy can also be used.

The longitudinal gust perturbation is comprised of both slow acoustic wave and fast acoustic wave perturbations. By using the longitudinal gust perturbations as our prime disturbance, we can cater for both J^+ and J^- perturbations. A static pressure sensor upstream of the bleed is used to estimate the Mach number perturbations. The feed-forward control architecture is shown in Figure 11.

The change in throat Mach number due to upstream longitudinal al gust perturbation du and upstream bleed perturbation $ds1$ are given as:

$$dM_{th} = G_{Mth\_du}(j\omega)du + G_{Mth\_ds1}(j\omega)ds1 \quad (7)$$

Using the controller gain K we can express

equation (7) as:

$$dM_{th} = G_{Mth\_du}(j\omega)du + \\ G_{Mth\_ds1}(j\omega)KG_{Ms\_du}(j\omega)du \quad (8)$$

The controller gain K for cancellation of the throat Mach number perturbation is:

$$K = -\frac{G_{Mth\_du}(j\omega)}{G_{Mth\_ds1}(j\omega)G_{Ms\_du}(j\omega)} \quad (9)$$

A typical controller frequency response and its synthesis using IIR filter is shown in Figure 12.
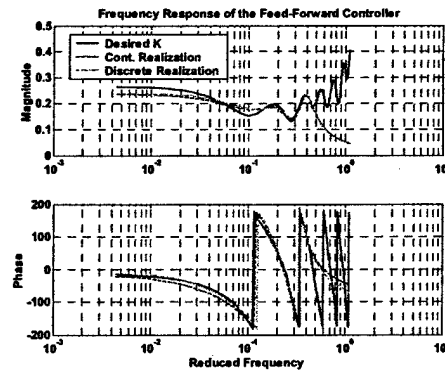

Figure 12: Frequency response of the feed-forward controller and its realizations.

Shock Motion Control

Shock motion can be controlled by sensing the location of the shock by an array of static

9

pressure sensors. Using the location of the shock as feedback a simple proportional controller can be used to drive the shock bleed to keep the shock stable on the face of compressor and atmospheric disturbances. A detailed discussion of shock motion control using this technique can be found in MacMartin.[12]

Results

The control architecture discussed above was tested in the 2D unsteady simulation embedded in Simulink. Figure 13 shows the impact of the controller in attenuating the longitudinal (forward) gust, vertical gust and temperature perturbations. While the temperature perturbations were neglected in the design of the feed-forward controller, Figure 13 shows that over most of the low frequency range of interest, the controller is able to cancel the temperature perturbations.
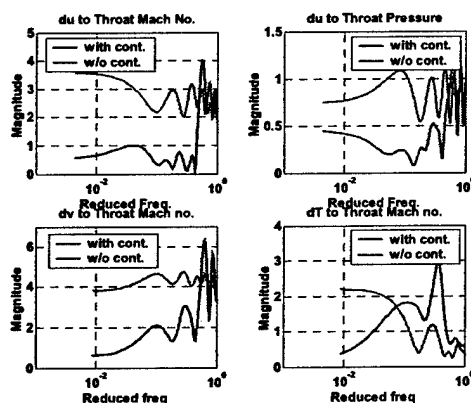

Figure 13: Controller effectiveness for changes in throat mach number and pressure.

The controller effectiveness can also be examined via the spectrum of the atmospheric disturbances at the throat. Figures 14a-c show the spectrum of the atmospheric disturbances and variations in throat Mach number with and without control. Figure 14c shows that, while temperature disturbances above the maximum frequency of interest (0.1) are amplified, the controller is still effective for lower frequency disturbances where the maximum energy is concentrated.

Table 1 shows the RMS values of the throat Mach number variations due to different types of disturbances. A substantial reduction in the RMS

values of the throat Mach number for the various disturbances is achieved with active control.
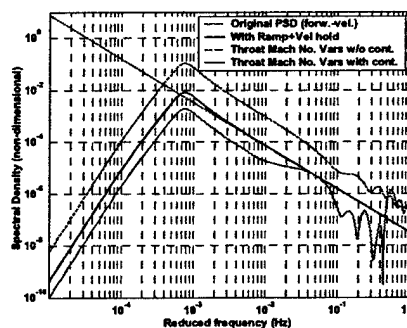
Figure 14a: PSD of throat Mach number variations with and without forward velocity gust control.
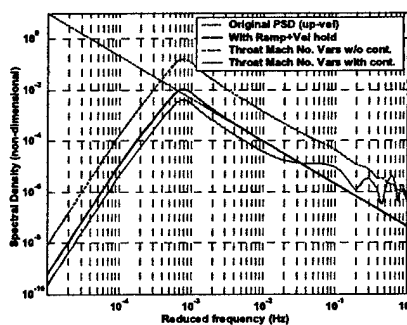
Figure 14b: PSD of throat Mach number variations with and without vertical velocity gust control.

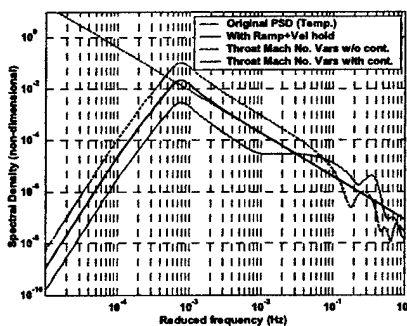Figure 14c: PSD of throat Mach number variations with and without temperature gust control.

It is also apparent that this control architecture is most effective in attenuating slow acoustic waves, and entropy perturbations are mildly amplified by the controller. This is expected since the bleed cancels the slow acoustic perturbations more effectively than the fast acoustic and entropy perturbations.

10

Disturbance Type	RMS M_{throat} w/o control $(\times 10^{-3})$	RMS M_{throat} with control $(\times 10^{-3})$
Horizontal Gust	11.0	1.7
Vertical Gust	13.8	2.7
Temperature	10.8	2.6
J+	16.2	5.2
J-	48.3	6.4
Entropy	8.7	9.7

Table 1: RMS value of throat Mach number variations with control and without control.

Conclusions

The design of a high recovery inlet with reduced stability to unstart has been presented. The low bleed requirement and enhanced recovery can have a substantial impact on propulsion systems for long-range supersonic aircraft. The atmospheric turbulence is studied and characterized in order to develop suitable control laws for the inlet. The dynamic characteristics of the inlet are modeled using quasi-1D and 2D Euler equations. The quasi-1D simulation of the inlet dynamics, which was shown to be in good agreement with the 2D simulation in the range of the frequencies of interest, was used to develop the control algorithm. The stability of the inlet was enhanced using a simple feed forward controller which significantly reduced the RMS values of the throat Mach number perturbations to various incoming disturbance types. Using separate estimators for the slow and fast waves, and designing a controller to cancel these waves, can improve the performance of the present throat Mach number controller.

Acknowledgements

References

[1] Paduano, J., Merchant, A., Drela, M., Lassaux, G., Schuler, B.,"Design and Testing of a High-Recovery, Actively Controlled Supersonic Inlet," MIT Report, January 2002.

[2] Mayer, D.W., Paynter, G.C., "Prediction of Supersonic Inlet Unstart Caused by Free stream Disturbances," AIAA Journal, Vol. 33, No. 2, February, 1995.

[3] Soreide, D., Bogue, R., Seidel, J., Ehernberger, L.J., "The use of a LIDAR Forward-Looking Turbulence Sensor for Mixed-Compression Inlet Unstart Avoidance and Gross Weight Reduction on a High Speed Civil Transport," AIAA Paper, 1997.

[4] Youngren, H.H., Drela, M., "Viscous/Inviscid Method for Preliminary Design of Transonic Cascades," AIAA Paper AIAA-91-2364.

[5] Merchant, A.A., "Design and Analysis of Supercritical Airfoils with Boundary Layer Suction," AIAA 96-2397, June, 1996.

[6] Tank, W.G., Gillis, J., "Atmospheric Disturbance models for linear and nonlinear system response analysis," AIAA 34th Aerospace Sciences Meeting and Exhibit, Reno, NV, January 1996.

[7] Tank, W.G., "Atmospheric Disturbance Environment Definition", NASA report CR-195315, February 1994.

[8] Fairall, C.W., and White, A.B., "A Stochastic Model of Gravity-Wave Induced Clear Air Turbulence," Journal of Atmospheric Sciences, 49, pages 1771-1790, 1991.

[9] Hurrell, H. G., "Analysis of Shock Motion in Ducts During Disturbances in Downstream Pressure," TN 4090, NACA, 1957.

[10] Culick, F. E. C., Rogers, T., "The Response of Normal Shocks in Diffusers." AIAA Journal, Vol. 21, No. 10, pp. 1382-1390, 1983.

[11] Yang, V., Culick, F. E. C., "Analysis of Unsteady Inviscid Diffuser Flow with a Shock Wave," AIAA Journal of Propulsion and Power, Vol. 1, No. 3, pp. 222-228, 1985.

[12] MacMartin, D.G., "Dynamics and Control of Shock Motion in a Near-Isentropic Inlet," AIAA 2002-2943.

[13] Freund, D., Sajben, M., "Experimental Investigation of outflow boundary conditions used in unsteady inlet flow computation," AIAA Aerospace Sciences Meeting & Exhibit, 35th, Rno, NV, Jan. 6-9, 1997.

[14] Sajben, M., Said, H., "Acoustic-Wave/Balde-Row Interactions Establish Boundary Conditions for Unsteady Inlet Flows," Journal of Propulsion and Power, Vol. 17, No. 5, September-October 2001.

DYNAMICS AND CONTROL OF SHOCK MOTION IN A NEAR-ISENTROPIC INLET

Douglas G. MacMartin*

California Institute of Technology
Pasadena, CA 91125

ABSTRACT

Inlet pressure recovery of supersonic aircraft could be improved using a near-isentropic inlet with only a weak normal shock aft of the throat, however, such an inlet is highly susceptible to unstart. Small perturbations can move the shock ahead of the throat, where it is unstable. The dynamics of this problem are analyzed using a low-order model involving a single non-linear differential equation. This model allows parametric exploration of both the potential and limitations of using control to actively stabilize the shock. The shock motion can be controlled using suction either upstream or downstream of the shock, with the latter providing greater authority. With reasonable constraints on actuator authority and bandwidth, simple control laws stabilize the shock motion.

1 INTRODUCTION

Inlets for supersonic aircraft decelerate the incoming flow to the desired subsonic condition, recovering the energy as pressure. Unless the throat Mach number is exactly one, there will be a terminal shock aft of the diffuser throat that introduces losses. While a weak shock would not introduce significant loss, it is more susceptible to disturbances. If the perturbed shock moves ahead of the throat, it becomes unstable, moves forward rapidly, ultimately resulting in a strong external bow shock, with a significant increase in drag and the potential for engine surge; this is known as *unstart*.[1-3] Active stability control could enable a practical, near-isentropic supersonic aircraft inlet, with higher pressure recovery, but without risk of unstart. This paper describes low order modeling of the shock dynamics, and investigates active control based on this model. A schematic of a hypothetical near-isentropic inlet is shown in Figure 1, illustrating the area variation, nominal shock location, and disturbances.

A reasonably accurate description of the inlet dynamics can be obtained through a computational model. A one-dimensional Euler code has been developed by MIT that adequately captures the response of the shock to disturbances and control actions. This model requires on the order of 1000 state variables to describe the flow field. While this model can be executed reasonably rapidly, a very low order model that still captures the key features of the response is invaluable in the development of control strategies. The purpose of the model developed in the next section is to understand stability regions, motivate actuator and sensor placement, and assess control authority and bandwidth requirements, all as a function of design parameters such as the nominal shock location (or strength). While the full one-dimensional simulation captures details of the dynamics that a reduced order model cannot, the extra complexity can mask some of the underlying physics, particularly regarding parametric variations. Simplifying assumptions are required, and the key is ensuring that the fundamental physics are not discarded in the process.

The derivation of the model described herein is based on a linearization approach, similar to that described by Hurrell[4] to investigate shock motion, and by Culick *et al.*[5,6] to analyze the acoustic reflection and transmission properties of a normal shock. In each of these papers, the response to pressure disturbances arriving at the shock is computed by perturbing the shock equations and taking terms to first order. This linearization approach is extended herein by explicitly representing the perturbations as acoustic waves. The model is then used to evaluate the potential for control to actively stabilize the shock location.

The primary assumptions required are that the flow is isentropic in the immediate vicinity of the shock, one-dimensional, and that the perturbations in the flow upstream and downstream of the shock are acoustic. In addition, the model only captures the behaviour of the existing shock, and does not account for the possibility of other shocks being created elsewhere in the inlet. Based on these as-
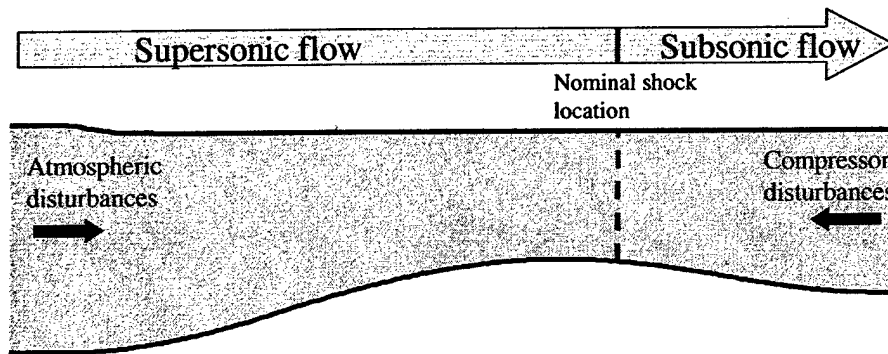
Figure 1: Hypothetical near-isentropic inlet. The system is perturbed both by upstream (atmospheric) and downstream (compressor) disturbances.

sumptions, we can compute the shock motion and the strength of the downstream propagating acoustic wave that result from both upstream and downstream acoustic disturbances. The shock response is captured by a single non-linear ordinary differential equation (ODE), and this simple low order model qualitatively matches the behaviour of the 1-dimensional Euler code mentioned earlier. Figure 7 illustrates the nonlinear response; if the shock is subject to a sinusoidal excitation (not intended to be realistic, but illustrative), then the response includes not only a sinusoidal component, but also a slow bias motion towards the throat that can eventually result in instability.

This paper describes the assumptions and derivation of the dynamics of the shock motion. The following questions are then addressed parametrically:

- The open-loop domain of attraction, as a function of disturbance bandwidth and amplitude, and the qualitative response of the shock to disturbances.

- Actuator and sensor selection.

- Actuator bandwidth and authority requirements.

- The control algorithm; two algorithms are compared that require different sensor information.

A simple controller that uses a single shock location sensor fedback to downstream bleed is sufficient to stabilize the shock.

2 DERIVATION

2.1 Approach and Assumptions

The inlet is conceptually divided into three regions: the supersonic regime upstream of the shock; the subsonic regime downstream; and the shock itself.
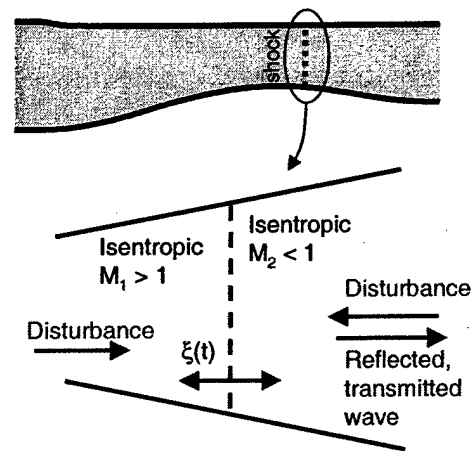

Figure 2: Schematic of reduced order modeling approach. We solve for the shock motion $\xi(t)$ and the reflected/transmitted downstream wave due to upstream and downstream disturbances.

This is illustrated schematically in Figure 2. If we assume that the portion of the inlet upstream and downstream of the shock are isentropic, then we can derive equations for the variation in flow field that the shock encounters as it moves up or downstream. We consider only acoustic disturbances arriving at the shock, and include only time delays for the propagation dynamics. In both the subsonic (downstream) and supersonic (upstream) regime, the disturbances can therefore be written as the sum of two waves propagating at $(1 + M)$ and $(1 - M)$ times the speed of sound. In the subsonic regime, this corresponds to upstream and downstream propagating waves; in the supersonic regime both travel downstream and will be referred to as "fast" and "slow" waves respectively. The shock motion and the amplitude of the downstream propagating wave are computed in response to the upstream propagating wave

and both acoustic waves in the upstream, supersonic region. The assumptions and derivation are similar to those in Culick,[5] except that the disturbances are explicitly represented as acoustic waves rather than as pressure pertubations. This permits more general treatment of the dynamics, and of the reflection and transmission coefficients.

The assumptions, therefore, are as follows:

- Only one-dimensional flow is considered; in particular, there is no communication through the boundary layer, no shock-boundary layer interaction, and actuation is assumed to immediately affect the bulk flow.

- No additional shocks are created in the inlet. Note that there are two possible unstart mechanisms; if the terminal shock moves upstream of the throat, or if the throat Mach number drops below unity and a new shock forms immediately upstream. Atmospheric disturbances typically result in the latter; this assumption therefore restricts this model to capturing unstart due to downstream disturbances.

- The shock satisfies the usual quasi-steady shock equations at each instant of time (see Culick[5]).

- The supersonic and subsonic regimes are isentropic close to the shock location.

- Disturbances are acoustic; entropy perturbations resulting from atmospheric disturbances are not considered.

- The propagation of disturbances within the supersonic and subsonic regimes is not included other than to account for time delays in the control solution. A more accurate description of the acoustic propagation and the reflection off of the downstream boundary condition could be incorporated into the current modeling framework in a straightforward manner.

The resulting equations can be further simplified for a weak shock by taking terms only to first order in $M_1 - 1$.

The derivation follows from three sets of equations: (i) the usual shock equations, in the frame of reference of the moving shock (and thus dependent on the velocity of the shock), (ii) isentropic relationships, which give the variation in the nominal upstream and downstream flow variables as a function of the area variation, which is in turn a function of the shock location, and (iii) the relationships between perturbations in the upstream and downstream flow variables and the upstream and downstream propagating acoustic waves.

2.2 Equations

The upstream variables $(\cdot)_1$ and downstream variables $(\cdot)_2$ are related by the usual shock equations, in the frame of reference of the moving shock:

$$\frac{p_2}{p_1} = 1 + \frac{2\gamma}{\gamma+1}\left(M_1^2 - 1\right) \tag{1}$$

$$\frac{u_2}{u_1} = 1 - \frac{2}{\gamma+1}\left(\frac{M_1^2 - 1}{M_1^2}\right) \tag{2}$$

$$M_2^2 = \frac{2 + (\gamma-1)M_1^2}{2\gamma M_1^2 - (\gamma-1)} \tag{3}$$

Denote the perturbation in the nominal shock location as ξ. In estimating the response of the shock to a perturbation, we need to consider both the perturbation itself, and the change in local conditions caused by fact that the shock has moved. The nominal flow conditions that the shock moves into, denoted by $(\bar{\cdot})$, are assumed to be given by the isentropic relations, from which one can derive:

$$\frac{1}{M^2 - 1}\left(\frac{1}{A}\frac{dA}{dx}\right) = \frac{1}{u}\frac{\partial u}{\partial x} \tag{4}$$

$$= -\frac{1}{\gamma M^2}\left(\frac{1}{p}\frac{\partial p}{\partial x}\right) \tag{5}$$

$$= \frac{2}{(\gamma-1)M^2 + 2}\left(\frac{1}{M}\frac{\partial M}{\partial x}\right) \tag{6}$$

These hold in the inlet frame of reference.

Finally, consider the effect of disturbances. Upstream perturbations in p_1 denote p_u, etc., and downstream denote as p_d. As discussed in the assumptions, the disturbances are represented as propagating acoustic waves. Denote the rightward and leftward (with respect to the flow) propagating waves as having pressure P^+ and P^-, or relative pressure perturbations given by $\delta_{u,d}^{\pm} = P_{u,d}^{\pm}/\bar{p}_{1,2}$ for the four acoustic waves δ_u^+, δ_u^-, δ_d^+ and δ_d^-. The remaining flow perturbations are related to the wave variables by:

$$\frac{p_u}{\bar{p}_1} = \delta_u^+ + \delta_u^- \tag{7}$$

$$\gamma M_1 \frac{u_u}{\bar{u}_1} = \left(\delta_u^+ - \delta_u^-\right) \tag{8}$$

$$\gamma M_u = \left(\delta_u^+ - \delta_u^-\right) - \frac{\gamma-1}{2}M_1\left(\delta_u^+ + \delta_u^-\right) \tag{9}$$

for the upstream variables and with subscripts $(\cdot)_d$ for the downstream perturbations.

2.3 Derivation

Following Culick,[5] the pressure immediately upstream of the shock for small shock motion ξ about

a nominal location x_0 is

$$p_1(x_0 + \xi) = \bar{p}_1(x_0) + p'_1(\xi)$$

where

$$p'_1(\xi) = \frac{\partial \bar{p}_1}{\partial x}\xi + p_u \qquad (10)$$

The perturbation in the Mach number upstream of the shock in the frame of reference of the shock is given by

$$M'_1 = \frac{\partial \bar{M}_1}{\partial x}\xi + M_u - \frac{1}{a_1}\dot{\xi} \qquad (11)$$

Similar equations can be written for perturbations in all of the flow variables upstream and downstream of the shock.

Substituting these equations and the wave relationships into Eq'ns (1) and (2) gives two equations which can be solved for the shock motion ξ and the downstream propagating wave δ_d^+.

2.4 Shock ODE

The shock motion satisfies the ODE:

$$\frac{1}{\bar{a}_1}\dot{\xi} = \alpha(\xi)\xi + \beta_d^- \delta_d^- + \beta_u^+ \delta_u^+ + \beta_u^- \delta_u^- \qquad (12)$$

where

$$\alpha(\xi) = -f_\alpha(M_1) \cdot \left(\frac{1}{A}\frac{dA}{dx}\right) \qquad (13)$$

and $\beta_{u,d}^\pm$ are only a function of M_1. The variables $\delta_{u,d}^\pm$ capture the effects of upstream and downstream perturbations, including both disturbances and control. Equation (12) is of the same form as that derived previously,[4,5] but the dependence on M_1 differs slightly when the dynamics are derived assuming an applied acoustic perturbation, rather than an applied downstream pressure perturbation.

The functional form for f_α is always positive, thus one immediately obtains that the shock is stable in the diverging section, and unstable in the converging section. The response is also non-linear, as dA/dx changes with the shock location (in particular, it is zero at the throat). This dependence of α on ξ introduces the nonlinear behaviour seen in Figure 7.

For notational convenience define

$$\mathcal{M} = 2M_1 + \frac{M_1^2 + 1}{M_1 M_2}$$

Then the function f_α has the form

$$f_\alpha(M_1) =$$

$$= \frac{(\gamma - 1) + (\gamma^2 + 1)M_1^2 + \gamma M_2^{-1}\left((\gamma - 1)M_1^2 + 2\right)}{(\gamma + 1)\mathcal{M}}$$

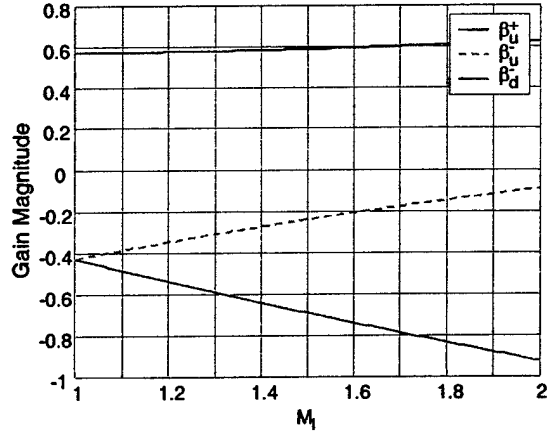$$\simeq \frac{\gamma}{4}(M_1 + 1) \qquad (14)$$

Figure 3: Variation of gains with Mach number. The "fast" upstream wave has opposite sign to the remaining perturbations. Downstream perturbations have higher gain than upstream for $M_1 > 1$.

The functional forms for the gains are:

$$\beta_d^- = -\frac{\gamma + 1}{\gamma \mathcal{M}}\frac{p_2}{p_1} \qquad (15)$$

and

$$\beta_u^\pm = \frac{1}{\gamma \mathcal{M}}\left[\frac{\gamma + 1}{2}\frac{p_2}{p_1}(1 \mp M_2/M_1)\right.$$
$$\left. \pm 2\left(1 \mp \frac{\gamma - 1}{2}M_1\right)\left(M_1 + \frac{1}{M_1^2 M_2}\right)\right] \qquad (16)$$

Since we are interested in the behaviour for a weak shock, these functions can be approximated by keeping terms only to first order in $M_1 - 1$:

$$\alpha(\xi, M_1) = -\frac{\gamma}{2}\left(1 + \frac{M_1 - 1}{2}\right)\left(\frac{1}{A}\frac{dA}{dx}\right) \qquad (17)$$

$$\beta_d^-(M_1) = -\left(\frac{\gamma + 1}{4\gamma} + (M_1 - 1)\frac{3\gamma - 1}{4\gamma}\right) \qquad (18)$$

$$\beta_u^+(M_1) = \frac{3 - \gamma}{2\gamma} \qquad (19)$$

$$\beta_u^-(M_1) = -\frac{\gamma + 1}{4\gamma}(2 - M_1) \qquad (20)$$

One can immediately note that for control using suction, $\delta_{u,d}^\pm$ are all negative, and thus the "fast" upstream acoustic wave δ_u^+ is destabilizing. In the limit of a weak shock, both upstream and downstream forcing δ^- are equally effective, however the downstream gain increases with M_1 while the upstream gain decreases. Thus even for a moderately weak shock where $M_1 = 1.25$, the downstream gain is 50% higher than the upstream (see Figure 3).
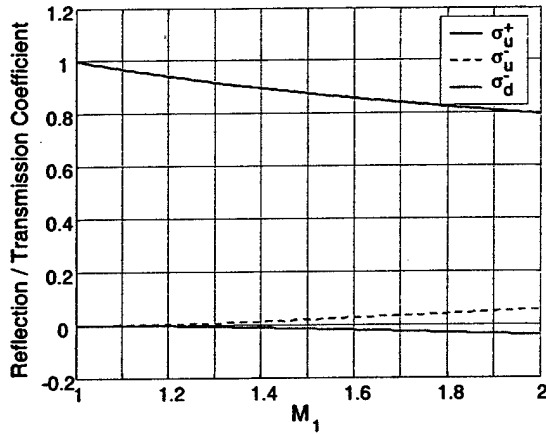
Figure 4: Reflection and transmission coefficients for acoustic waves as a function of Mach number.

To obtain quantitative results from the model above, we need to assume an area variation. Choose

$$\frac{1}{A}\frac{dA}{dx} = \frac{1}{\ell^2}(x_0 + \xi) \qquad (21)$$

Thus x_0 defines the nominal shock location, with the throat at $\xi = -x_0$, and ℓ is the characteristic length. Eq'n (12) for small $M_1 - 1$ can then be written as

$$\frac{1}{a_1}\dot{\xi} = -\frac{\gamma}{2}\frac{1}{\ell^2}(x_0 + \xi)\xi + \frac{\gamma+1}{4\gamma}\delta \qquad (22)$$

where $\delta = \delta_u^- - \delta_d^-$. Equation (22) can be non-dimensionalized using $\ell^* = \ell(2/\gamma)^{1/2}$ as the spatial scaling parameter and $\ell^*/\bar{a}_1$ as the temporal scaling; so $\xi^* = \xi/\ell^*$ and $t^* = t\bar{a}_1/\ell^*$ and $\delta^* = \beta\delta$. Dropping the notation $(\cdot)^*$ for convenience gives the non-dimensionalized shock equation as

$$\dot{\xi} = -(x_0 + \xi)\xi + \delta \qquad (23)$$

2.5 Reflection and Transmission

The amplitude of the downstream propagating acoustic wave δ_d^+ resulting from perturbations is represented using reflection and transmission coefficients σ_d^- and $\sigma_u^\pm$, where

$$\delta_d^+ = \sigma_d^- \delta_d^- + \sigma_u^+ \delta_u^+ + \sigma_u^- \delta_u^-$$

These coefficients are plotted in Figure 4. The reflection coefficient is of the form $\sigma_d^- = (1-s)/(1+s)$ where $s = (M_1^2+1)/(2M_1^2 M_2)$. For $M_1 \to 1$, then the "fast" upstream wave has a transmission coefficient of unity, while the remaining waves result only in shock motion and do not produce any downstream propagating wave. These results are consistent with previous papers[5,6] wherein the reflection coefficient

was shown to be small, while the transmission coefficient (for a pressure disturbance) was greater than unity for $M_1 > 1$. Note that Yang[6] gives the transmission coefficient in terms of pressure ratio. While the transmission coefficient of the fast wave shown in Figure 4 indicates a roughly constant relative wave amplitude with Mach number, the absolute amplitude of the downstream pressure wave increases with p_2/p_1 and can thus become quite large.

2.6 Inlet System Effects

The current model is intended to capture the dynamics of the shock itself; this could be extended to capture the dynamics of the overall inlet system, as shown in Figure 5. In addition to the shock, the full inlet system includes the creation and propagation of the acoustic waves caused by physical disturbances or control inputs, and the compressor or downstream boundary condition. While not included in the control simulations, the effect of these on the shock motion is briefly noted here.

The relative strength of δ^+ and δ^- can readily be evaluated for a given disturbance source; the waves generated by suction satisfy $|1 - M|\delta^- = (1+M)\delta^+$. The duct acoustic propagation involves time delay, amplitude variation, and waveform variation due to nonlinearities.

The downstream boundary condition (the engine compressor or fan) could be modeled simply as a reflection coefficient, or with increased complexity including the compressor dynamics. This boundary condition and its impact on the shock dynamics has been discussed elsewhere.[2,3,7,8] Note that if the reflection from the compressor (or more generally, the downstream boundary condition) is significant, then the direct impact of a given disturbance source on the shock may not capture the complete influence. The disturbance δ_u^+ does not significantly affect the location of a weak shock, but it is transmitted through the shock virtually unchanged, and the returning wave reflected from the compressor may have significant influence on the shock motion. This can be seen in simulations with the Euler code in Figure 9, where the constant pressure downstream boundary condition gives a -1 reflection coefficient.

Also note that the time delay for any disturbance is a function of the current shock location. This can be included by replacing the disturbance term $\delta_d^-(t)$ in the shock equations with $\delta_d^-(t - \tau(\xi))$, and similarly for δ_u^- and δ_u^+. The delay $\tau(\xi)$ is obtained by integrating the inverse of the wave speed $c = \bar{a}_{1,2}(1 \pm \bar{M}_{1,2})$ between the disturbance and the current shock location, this can be approximated by a linear dependence on ξ. Unless the throat Mach

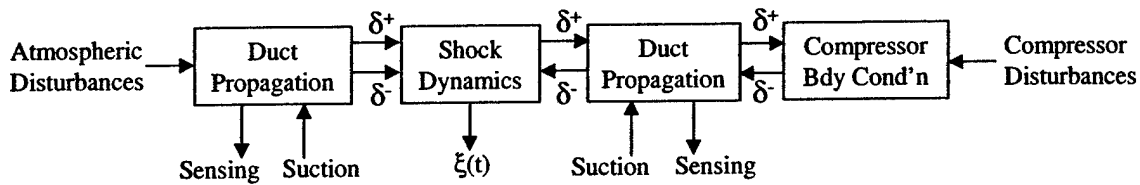American Institute of Aeronautics and Astronautics

Figure 5: Inlet system block diagram including coupling between shock dynamics, duct acoustic propagation, and downstream (compressor) boundary condition.

number is close to unity, the shock velocity will be much slower than the acoustic speed for realistic disturbances. For $M_1 \rightarrow 1$, then the variation in the disturbance wave form with ξ may also be important.

3 OPEN-LOOP DYNAMICS

Based on the low order model, several observations about the uncontrolled dynamics can be made. The most important questions to answer in order to design an active control system are the open loop frequency response, and the relative authority of different disturbance or control mechanisms.

The shock responds more to low frequency disturbances than high frequency, with zero-frequency disturbances being the most destabilizing. For a disturbance pulse that is short compared to the time constant $1/\alpha$, only the total impulse of the pulse matters, and not the detailed shape. The largest disturbance that can be tolerated can be obtained by setting $\dot{\xi} = 0$ in Eq'n (12) and setting $\beta\delta$ equal to the maximum value of $\alpha(\xi)\xi$. For the area variation used in Eq'n (22) then the maximum downstream (compressor) disturbance that can be tolerated is

$$\delta_M = \frac{\gamma^2}{2(\gamma + 1)} \left(\frac{x_0}{\ell}\right)^2 \qquad (24)$$

This is consistent with the largest stable steady disturbance obtained from the MIT Euler code. The largest stable disturbance that can be tolerated as a function of frequency is shown in Figure 6.

For a given inlet geometry $A(x)$, increasing the throat Mach number does not significantly improve shock stability. Increased Mach number does reduce the time delay for any actuator and therefore could improve closed-loop stability. For a shock near the throat, $1/A \cdot dA/dx$ decreases as the shock moves forward and increases as the shock moves aft. Exciting the shock with a sinusoidal disturbance generates a slow movement of the shock towards the throat, superimposed on the sinusoidal motion, with the possibility of eventual unstart. Thus one cannot predict the maximum shock motion by using the value of α at $\xi = 0$. An example illustrating this non-linear
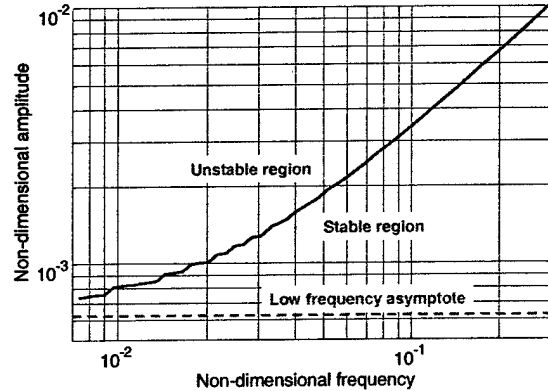

Figure 6: Computed stability boundary as a function of non-dimensional forcing amplitude and frequency. The non-dimensional nominal shock location is 0.05.
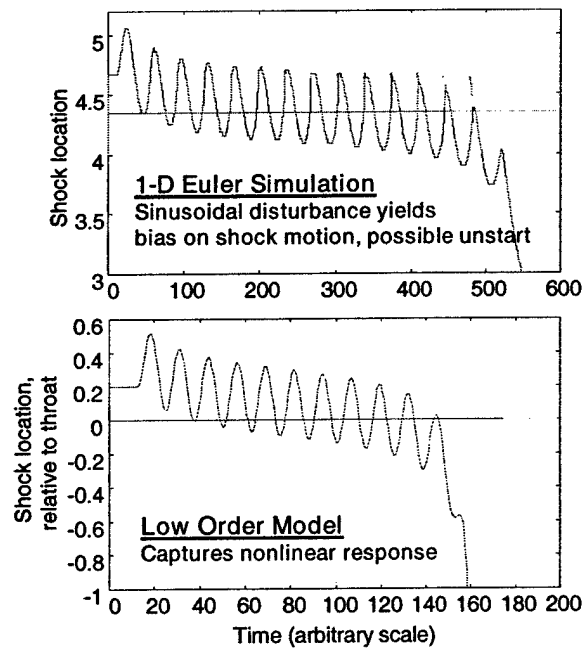

Figure 7: Qualitative comparison of non-linear shock response to a sinusoidal disturbance; from 1-D Euler code (top) and from reduced order model.

6
American Institute of Aeronautics and Astronautics

behaviour is shown in Figure 7, which compares the response of both the low order model and the MIT 1-D Euler code to a sinusoidal disturbance.

The shock location is strongly excited by downstream disturbances, and by the "slow" upstream disturbance δ_u^-, propagating at speed $a_1(1 - M_1)$. The "fast" upstream disturbance δ_u^+ does not have a significant effect on the shock motion. Conversely, the transmission coefficient for the fast wave is much more significant than for the slow wave.

The acoustic behaviour of the inlet, obtained using the 1-D Euler simulation mentioned earlier, is illustrated in Figures 8 and 9. These plot the pressure perturbation for a short duration suction pulse either downstream or upstream of the shock. Both waves δ^+ and δ^- are created, with $\delta^- > \delta^+$ for both upstream and downstream suction. The magnitude of the gains $\beta_{u,d}^{\pm}$ in Eq'ns (18-20) is consistent with the behaviour observed in the Euler code. These figures also validate the small reflection coefficient, small transmission coefficient for δ_u^-, and transmission coefficient near unity for δ_u^+. Note that the Euler code has a constant pressure downstream boundary condition, giving a reflection coefficient of -1. This reflected wave is not necessarily representative of the ultimate application, and has a significant influence on the shock motion.

4 CONTROL

4.1 Actuator and Sensor Selection

There are three possible actuators one can consider for active control of the shock location; downstream suction (as in Fig. 8), upstream suction (Fig. 9), or local area variation at the shock location. This latter approach may ultimately be attractive if it can be implemented using distributed suction, however, mechanical area variation of sufficient authority is likely to be difficult and may lead to separation. Since the "fast" upstream wave does not significantly affect the shock motion, the control action from both upstream and downstream suction results from δ^- traveling at $(1 - M)$ times the sound speed. Therefore for actuation the same distance away from the shock, the time delay is comparable, while the authority is higher for downstream suction ($\beta_d^- > \beta_u^-$). Thus, unless other implementation issues affect the decision, the best actuation for this system is downstream suction.

If the throat Mach number is very close to unity, then the propagation time delay from the actuator to the shock can become quite large. Therefore, while feedback control of the shock motion is essential for robustness, feedforward control based on sensing of

incoming perturbations may be essential to provide sufficient overall time response. The feedback control then only needs to correct for the residual error from the feedforward control.

For downstream (compressor) disturbances, the feedforward control needs any set of sensors that can detect the upstream propagating wave amplitude, and distinguish between it and downstream propagating waves; similarly for upstream (atmospheric) disturbances, the "fast" and "slow" waves need to be sensed and distinguished. The feedforward control law is obtained based on the difference in time delay between the sensing and the actuator locations, and the transfer function between actuation and the wave amplitude that it generates.

The shock location is an obvious choice for feedback. However, in practice this will involve either a distributed array of sensors or a model-based estimation from a subset of sensors. An alternative is to have one or more discrete sensors at locations ξ_i from which one can establish whether $\xi > \xi_i$.

4.2 Authority and Bandwidth

The required actuator authority u_M can be directly estimated from the maximum disturbance amplitude as $u_M > \delta_M$, where both δ_M and u_M are expressed as the amplitude of the wave δ_d^- that arrives at the shock due to the maximum disturbance or control respectively. Thus one must also estimate the change in amplitude with propagation through the duct; this is a function of the area variation.

The minimum time delay for the control, including actuator bandwidth, computational delay, and propagation delay, can also be obtained from the model. Assume that α is small compared to the disturbances that are expected. The worst case disturbance is a step change to the maximum value. The shock therefore moves at $\dot{\xi} \simeq \beta_d^- \delta_M \bar{a}_1$. If $u_M = \delta_M$ then the maximum time lag τ_M for applying u_M is the time it takes the shock to move from its nominal location x_0 to the throat, or

$$\tau_M < \frac{1}{\bar{a}_1 \beta \delta_M} x_0 \qquad (25)$$

This estimate is conservative, and can be refined by including the effects of α. If the actuator has greater authority, then some motion of the shock past the throat is possible, and greater time delay can be tolerated. The estimate is based on an instantaneous step change in the disturbance, and lower disturbance bandwidth will also permit higher time lag. If the time lag is dominated by propagation, then one can obtain a constraint on the actuator injection lo-
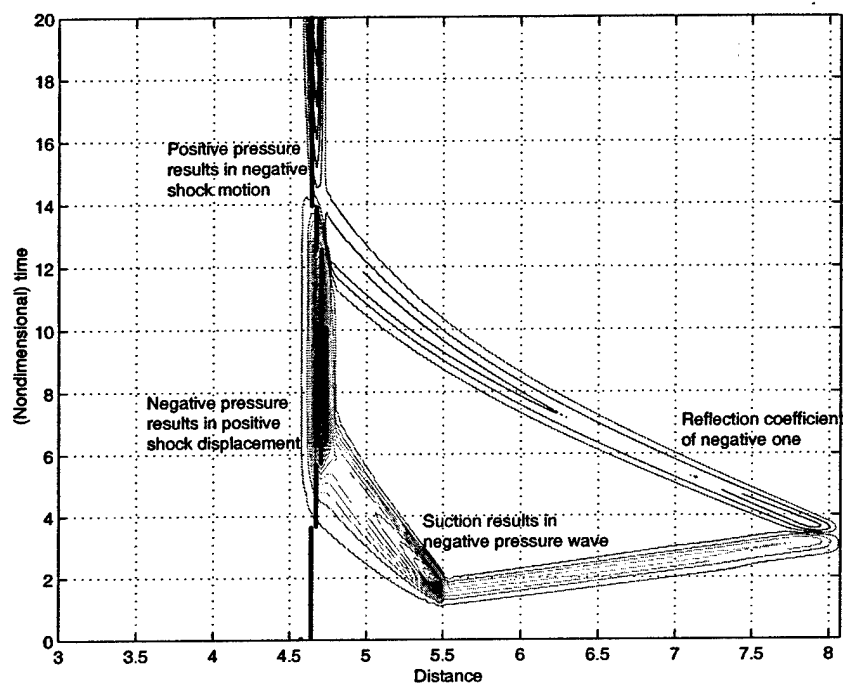
Figure 8: Acoustic wave propagation in inlet for a short duration suction pulse downstream of the shock (from MIT 1-D Euler code). The shock location is shown in solid black.
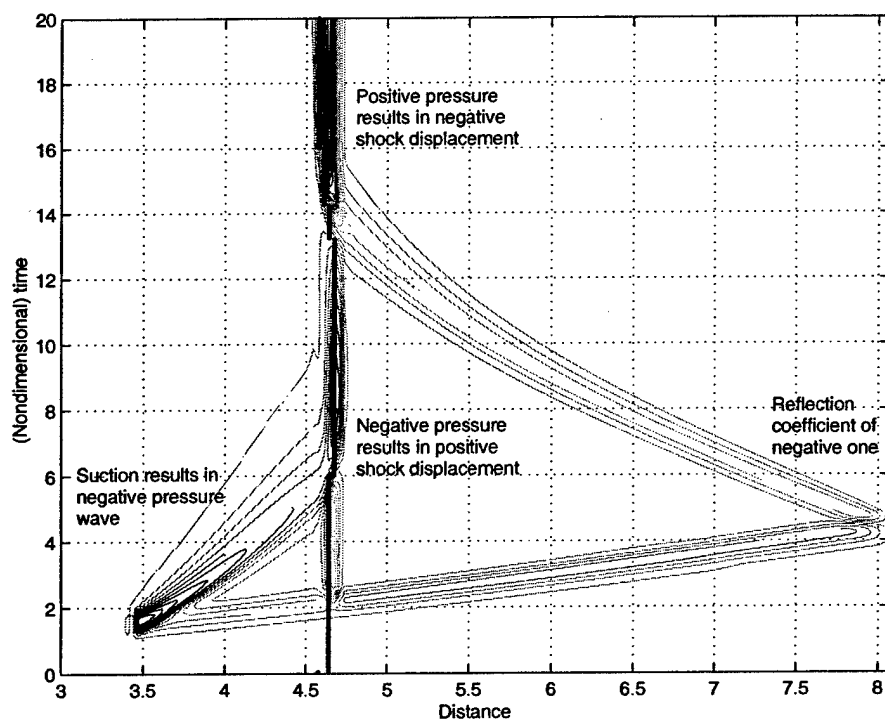

Figure 9: Acoustic wave propagation in inlet for a short duration suction pulse upstream of the shock (from MIT 1-D Euler code). The shock location is shown in solid black; note that the motion due to the wave reflected off of the downstream boundary condition is significant.

American Institute of Aeronautics and Astronautics

cation x_i to satisfy the time delay, as

$$\frac{x_i}{x_0} < \frac{1 - M_2}{\beta \delta_M} \tag{26}$$

where the variation in Mach number has been ignored for simplicity.

4.3 Control Law Analysis

Both the actuator saturation and the time delay must be taken into account in the design of the control law. A proportional control law $u = K\xi$ is close to optimal for this system. Therefore, consider the following two control laws. The first is a proportional controller, with saturation, while the second simplifies the controller and assumes only a single feedback sensor.

$$u_a(\xi) = \begin{cases} 0 & : & \xi > 0 \\ -K\xi & : & 0 > \xi > x_0 \\ u_M & : & \xi < x_0 \end{cases} \tag{27}$$

$$u_b(\xi) = \begin{cases} 0 & : & \xi > \xi_0 \\ u_M & : & \xi < \xi_0 \end{cases} \tag{28}$$

The proportional gain $K = u_M/x_0$ in $u_a(\xi)$ applies between the nominal shock location ($\xi = 0$) and the throat ($\xi = x_0$). If the maximum control authority u_M is exactly the same as the required authority, then this controller will be marginally unstable, but if there is any safety factor at all then the shock will be moving slowly when it reaches the throat and the time delay will not be an issue. The design parameter ξ_0 in $u_b(\xi)$ can be chosen based on the ratio between the actual time delay τ and the maximum value τ_M derived earlier; $\xi_0 = (1 - \tau/\tau_m)x_0$.

The simulated control behaviour is shown in Figure 10, with actuator saturation $u_M = 0.05$, time delay $\tau = \tau_M/1.5$, and disturbance at a frequency and amplitude that would be unstable without control. The response is shown for two cycles of disturbance after the system has reached steady state. Both control laws stabilize the system, with the first control law, $u_a(\xi)$, resulting in a smoother response. Any actuator dynamics would result in some smoothing of the response shown for the simple control law $u_b(\xi)$. The simulation is plotted for two different disturbance amplitudes; the maximum that could be tolerated with either controller of $\delta_M = 0.05$ and half this value. The ultimate performance metric is to retain stability with minimum bleed requirements. Based on this metric, the smooth control law slightly outperforms the simple control law for the worst case disturbance, but is slightly worse for the smaller disturbance. The relative performance of u_a would be worse still for very small disturbances, as the simple controller would not respond at all.

A single sensor and a simple control law are adequate for stabilizing the shock. Since the additional information required by the smooth controller could add significant complexity, any small performance improvements are likely outweighed by extra cost. The use of a second sensor would allow a control law of the form

$$u_c(\xi) = \begin{cases} 0 & : & \xi > \xi_0 \\ u_M/2 & : & \xi_0 > \xi > \xi_1 \\ u_M & : & \xi < \xi_1 \end{cases}$$

which may be an adequate compromise between the simple and smooth controllers.

5 Conclusions

Active stabilization of a weak shock in a near-isentropic inlet would prevent unstart and enable low loss supersonic inlets to be designed. A simple model involving a single non-linear ODE captures the relevant shock dynamics for both upstream and downstream disturbances, and also the acoustic reflection and transmission properties of the shock. This model is useful for parametrically assessing actuator and sensor selection, actuator authority and bandwidth requirements, and for comparing different control strategies. For control actuation, downstream suction is preferable to upstream suction. A simple feedback control law that relies on a single sensor to determine when the shock is upstream of a critical location is sufficient to stabilize the system.

This model could be extended in several ways. The disturbances can be represented more physically by relating the relative amplitude $\delta_{u,d}^{\pm}$ of acoustic perturbations arriving at the shock to suction or atmospheric and compressor disturbances. This would permit explicit computation of the feedforward gains. Including the compressor boundary condition would permit a full inlet system model.

References

[1] Mayer, D. W. and Paynter, G. C., "Prediction of Supersonic Inlet Unstart Caused by Freestream Disturbances," *AIAA Journal*, Vol. 33, No. 2, pp. 266–275, 1995.
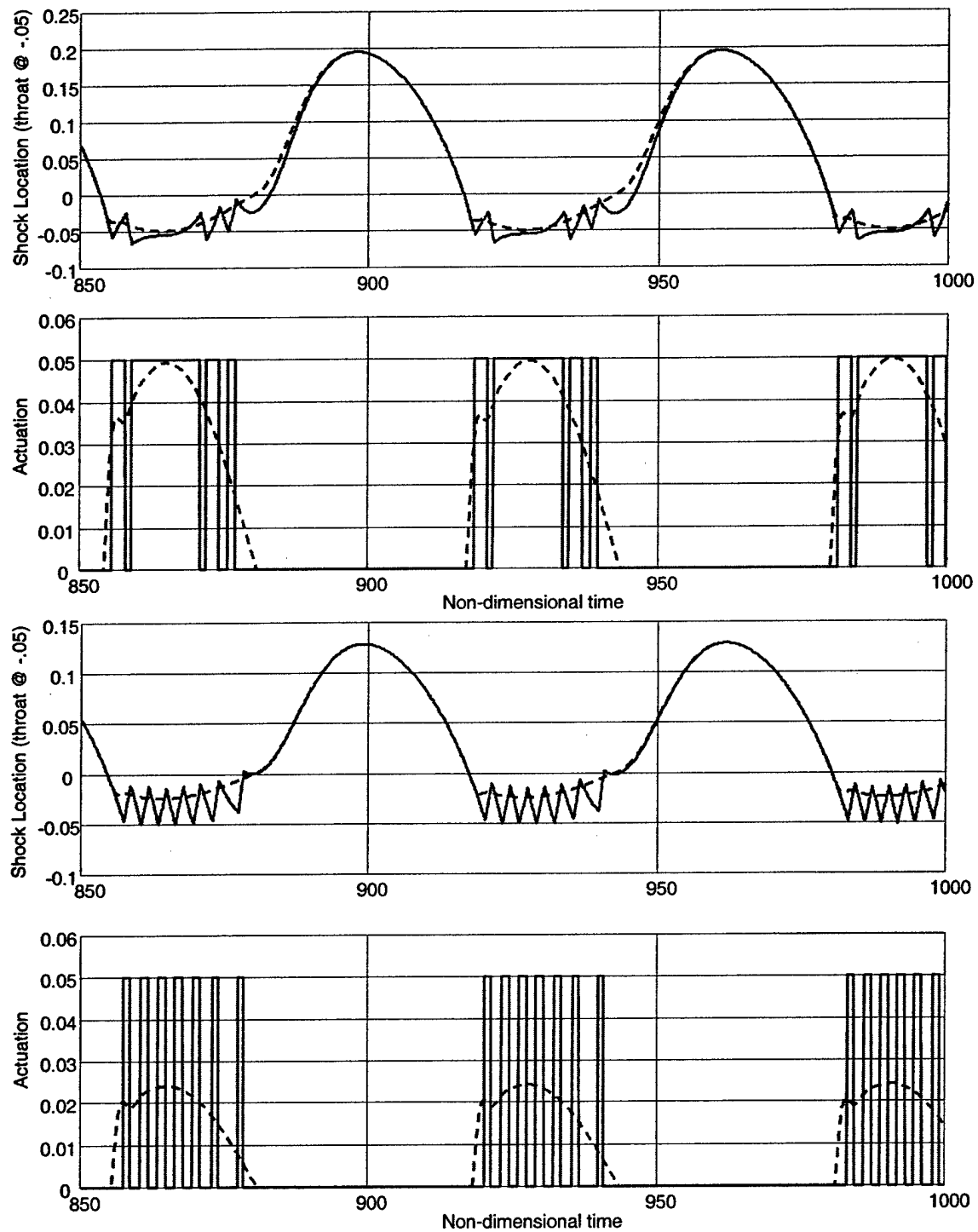
Figure 10: Comparison of control response to perturbation with smooth control law u_a (blue, dashed) and simple control law u_b (red). Upper pair of figures corresponds to a 5% perturbation, lower pair to a 2.5% perturbation. The upper plot in each pair shows the shock location, the lower plot the control.

[2] Numbers, K. and Hamed, A., "Development of a Coupled Inlet-Engine Dynamic Analysis Method," *33rd AIAA/ASME/SAE/ASEE Joint Propulsion Conference*, 1997. AIAA 97-2880.

[3] Giannola, P., Haas, M., Cole, G., and Melcher, K., "Modeling the Dynamics of Supersonic Inlet/Gas-Turbine Engine Systems for Large-Amplitude High-Frequency Disturbances," *36th AIAA/ASME/SAE/ASEE Joint Propulsion Conference*, 2000. AIAA 2000-3594.

[4] Hurrell, H. G., "Analysis of Shock Motion in Ducts During Disturbances in Downstream Pressure," TN 4090, NACA, 1957.

[5] Culick, F. E. C. and Rogers, T., "The Response of Normal Shocks in Diffusers," *AIAA Journal*, Vol. 21, No. 10, pp. 1382–1390, 1983.

[6] Yang, V. and Culick, F. E. C., "Analysis of Unsteady Inviscid Diffuser Flow with a Shock Wave," *AIAA Journal of Propulsion and Power*, Vol. 1, No. 3, pp. 222–228, 1985.

[7] Slater, J. W. and Paynter, G. C., "Implementation of a Compressor Face Boundary Condition Based on Small Disturbances," *ASME J. Turbomachinery*, Vol. 123, pp. 386–391, 2001.

[8] Sajben, M. and Said, H., "Acoustic-Wave/Blade-Row Interactions Establish Boundary Conditions for Unsteady Inlet Flows," *AIAA J. Propulsion and Power*, Vol. 17, No. 5, pp. 1090–1099, 2001.

Low-cost digital visualization and high-speed tracking of supersonic shockwaves

P.J. Bryanston-Cross[a*], A.J. Skeen[a], B.H. Timmerman[a], P. Dunkley[a],
J. Paduano[b], G.R. Guenette, Jr.[b]

[a] Optical Engineering Laboratory, University of Warwick, Coventry CV4 7AL, UK;
[b] Gas Turbine Laboratory, Massachusetts Institute of Technology, Cambridge, MA, USA 02139

ABSTRACT

A low-cost and low-maintenance digital focused shadowgraph flow visualization system has been developed to provide fast diagnostics of rapidly changing phenomena in supersonic flows. The system is particularly designed for tracking shock positions in a supersonic inlet, enabling high-speed active shock control. It is based on a low-cost, high-intensity white LED light source, which can be flashed with microsecond pulses enabling freeze-frame imaging of constant illumination quality. The system features three modes of operation: 1. High-resolution digital still frames and sequences (1280x1024, 2fps), 2. High-resolution digital frames and sequences showing spatial-temporal variation in flow field (1280x1024, 12 fps), 3. Adjustable windowed digital frames at reduced resolution, but at high frame rates (980 fps at 1280x8 pixel viewing area). The three modes of operation allow high-speed tracking of flow features such as moving of shock waves (up to 980 Hz) as well as overall instantaneous views of the flow. Furthermore, it allows direct identification of areas where high-speed changes occur. The positional shock data can be transmitted directly to a shock-stabilizing control system. Results are presented of the unsteady flow generated by an aspirated cone-shaped nozzle in a supersonic flow in the supersonic wind tunnel of the MIT Gas Turbine Laboratory.

Keywords: Shadowgraphy, CMOS, compressible flow, shock-tracking, active shock control.

1. INTRODUCTION

A flow visualization system was designed to provide a fast, low-cost and easy-to-use diagnostic for aerodynamic design concepts to be tested in the supersonic wind tunnel at the Gas Turbine Laboratory at MIT. Besides providing a general flow visualization capability, it is designed specifically for tracking high-speed unsteady events in a supersonic flow.

One of the investigations currently taking place at MIT is the design of an efficient supersonic inlet. One approach to increasing the efficiency of a gas turbine engine is to actively control the position of the intra-passage shock wave. A major design driver for supersonic diffusers is the requirement to prevent unwanted shock formation and shock blow-out (supersonic unstart). As part of the Quiet Supersonic Platform (QSP) program[1] to create a new efficient supersonic vehicle in the business jet size range, efficient supersonic inlets are being designed that rely on feedback control, rather than traditional design methods, to meet the unstart requirement. To aid in the design and to study the dynamics and control of shock formation and movement, high-speed tracking of shocks is needed. This requires a positional shock measurement resolution of better than 5 thousandths of an inch and a data transmission rate in the region of 1kHz to an active flow control device.

A low-cost, robust digital shadowgraphy system was developed that can both give a global visualization as well as perform tracking of shock-wave position in this type of flow. The movement of shock waves can be very fast, requiring recording of the shock wave position at rates up to 1 kHz. Because of the unsteadiness in the flow, individual images need to be recorded at short exposure times (microseconds), in order to 'freeze' the instantaneous events and avoid motion-blurring.

Shadowgraphy, as a well-established technique for compressible flow field visualization[2], especially in visualizing shock waves, was chosen as a basis in order to build a robust system with a minimal number of optical components.

* E-mail: pbc@eng.warwick.ac.uk; phone 44 2476 523131; fax 44 2476 418922

Furthermore, the use of a focused shadowgraphy system allows accurate determination of the actual position of shock waves in the flow.

The direct digital recording of the shadowgraph images allows a direct processing, in this case used for on-line real-time determination of shock wave position. This real-time information can then be used for direct-control feedback, e.g. to change flow settings in order to control the shock formation in a supersonic inlet.

High-speed flow visualization systems have been reported before. However, for a long time, high-frame rates could generally only be achieved by the use of specialized systems such as drum-cameras[3,4]. Direct digital imaging, however, has often been limited to recording only a few images at the high rate[5]. For longer sequences at high resolution, the digital recording rate is generally limited by the 25/30 Hz framing rate of standard cameras, or requires the use of expensive dedicated cameras[6]. Besides being expensive, such cameras have a short technology lifetime. Alternatively, high-speed tracking has been achieved using photodiode systems, however these 1-D systems will only give information on a single point rather than an area in the flow.

In the set-up presented here, CMOS-type cameras are being used. CMOS cameras offer the advantage of being relatively low-cost (compared to CCD-type) while still allowing high-speed tracking to be achieved. The CMOS camera used here does not have a global electronic shutter, which allows a new type of imaging, spatial-temporal streak imaging, giving information on both temporal as well as spatial variation.

The described system shows a direct method not previously explored to provide an active shock control within a transonic test facility. The system is tested on an aspirated cone-shaped nozzle placed in a supersonic wind tunnel flow. By varying the jet flow generated by the nozzle, the bow-shock around the cone is modulated, generating a high-frequency oscillation of the bow shock.

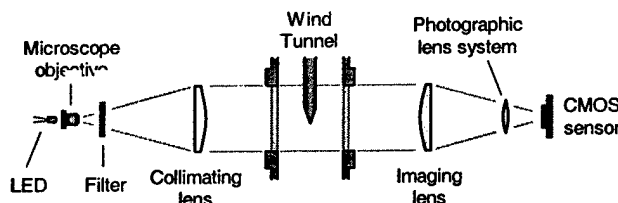## 2. SHADOWGRAPHY SET-UP

2.1 Focused Shadowgraphy

Figure 1: Shadowgraphy set-up

The focused shadowgraphy set-up used in the experiments described here is shown in Figure 1. It essentially consists of a light source, a microscope objective to expand the light beam, a second lens to produce a collimated beam going through the field of interest (e.g. wind tunnel test section) and a similar lens to collect the light directing it into a photographic lens system that is coupled to a CMOS detector. The use of a telescopic lens arrangement on the imaging side allows the focusing plane of the shadowgraphy system to be moved through the depth of the test volume by changing the position of the photographic lens and camera. Thus a sharp image of any object in the viewing area can be obtained. By adjusting the focus of the lens, the sharpness of the shocks as seen by the camera can be easily adjusted; by slightly defocusing, features can be made to show up more clearly.

The projection and imaging optics are mounted on a compact and portable optical breadboard system which can be positioned easily as two separate units on either side of the test facility (here a wind tunnel). The two separate units can be moved away for tunnel maintenance, and easily put back in position, maintaining alignment. The whole arrangement measures 96" from end to end and the collimated beam section is 5¼" in diameter (determined by the diameter of the collimating and imaging lenses).

The camera is mounted at 90 degrees such that the wind tunnel flow was along the horizontal axis of the resulting image.

Illumination System

Rather than using a discharge light source, such as a mercury arc lamp, a white LED is utilized. Unlike discharge sources, the solid-state device provides a stable and repeatable intensity level, with no jittering in its exact light emitting location. LEDs also offer long-life performance (>100,000 hours) in a compact package and can be pulsed quickly – typical rise times being less than 100ns.

The selected LED comprised a blue-emitting chip covered in a yellow-emitting phosphorous layer[7]. To obtain a more even light distribution a yellow filter was placed after the microscope objective in order to block the blue component of the light emitted by such LEDs. This increased monochromaticity of the light furthermore reduces chromatic aberrations in the final image.

Imaging System

The detection sensor used here is a Vitana PixeLINK PL-A653 mega-pixel CMOS camera. The ½" monochrome sensor has a resolution of 1280×1024 pixels with the ability to be sub-windowed down to 32x8 pixels at 8- or 10-bit depth. The maximum framing-rate depends on the size of the chosen window with a full-resolution frame-rate of 12fps at 8-bit image depth. Furthermore it provides a single cable FireWire connection, reading the image data directly into the memory of the host computer (400 Mbits/second).
Notably, the sensor lacks a global electronic shutter. The pixels in the sensor do not capture data at the same time, but rather are exposed pixel-by-pixel, row-by-row. As a consequence, the images that are captured are not instantaneous, but show a time delay between the rows. The start of each pixel's integration is staggered by the inverse of the pixel clock (up to 24MHz). When operating the camera at full-frame resolution this results in adjacent rows depicting events approximately 80 s apart.

2.2 Modes of Operation

By changing the camera settings it is possible to operate the shadowgraphy system in three separate modes, each of which produces a different type of result.

Still View

Without a global electronic shutter the camera is unable to capture an image across the entire sensor instantaneously. Therefore, to achieve such instantaneous snapshots, the camera is set to integrate for a time longer than the readout period of the whole sensor. At the point when all rows are integrating, the LED is flashed for the desired exposure time. Thus, all pixels are exposed during the same 'instant' (the duration of the LED flash) and a freeze-frame still image is obtained. The PL-A653 camera provides TTL-level connections to facilitate the control of external flash and shutter mechanisms, but only down to pulses of ~100 s. Therefore, in the experiments described here, an external triggered pulse generator is used allowing the LED to be pulsed for periods much shorter than the limit imposed by the camera. In the results shown here, the pulses lasted 10 s.

Still view mode therefore provides a live stream of instantaneously captured images. While theoretically limited to half of the normal frame rate, i.e. 6 fps for full-frame images, the implemented system ran at 2fps due to the fact the images had to be stored on hard-disk, rather than in RAM.

Spatial-Temporal Streak View

Running the camera in video mode results in images akin to those from a streak camera, i.e. the time at which the event is captured varies along the rows of the picture. Unlike a streak camera however, the captured image is not a one-dimensional strip but the whole two-dimensional area under investigation, i.e. each pixel in the image represents a different location as well as a different moment in time. The authors have therefore dubbed the result "spatial-temporal streak" images, and have found them to be a useful way to visualize, in real-time, the movement of shock waves that are oscillating at a speed that is otherwise difficult to capture.

With the camera positioned such that the shock waves run primarily along the vertical axis of the image, the shock typically oscillates no more than ±10 pixels side to side. At full-frame resolution, the sensor takes 1.2 s to sample 20 adjacent pixels, meaning that a shock would have to oscillate at over 20kHz before the readout rate causes rows to become motion-blurred by more than 1 pixel. While each row can therefore be considered an instantaneous view, adjacent rows depict the shock position separated by 80 s, the bottom of the picture representing the most recent position. The result is a wobbly image, updated at 12fps, that clearly shows the amplitude and frequency of shock movement.

Tracking View

The CMOS sensors can be set to any subwindow size at any position. For a reduced number of pixels, the frame rate increases. At the maximum horizontal and minimum vertical resolution of 1280×8, the frame rate is typically 980fps, with a read-out period of approximately 640 s. In the results shown here, the subwindow was 1280x8 pixels at a frame rate of 980 fps and for processing only the last 4 rows of this subwindow are considered. By considering only 4 of the rows the acquisition time for the considered pixels becomes (for a negligible exposure period) 320 s, or approximately $\frac{1}{8}$ of a 400Hz oscillation period. A smaller horizontal resolution further reduces the acquisition time, meaning that for the purposes of tracking, the exposure can be considered to be instantaneous.

While running in this high-speed mode, each frame delivered by the camera is processed to find the position of shocks. This is detailed in the following section. The resulting position data was plotted on screen, saved to disk and outputted electronically using an 8-bit D/A converter connected to the PC parallel port.

3. HIGH-SPEED TRACKING

Shadowgraphy is based on the fact that light beams that travel through a medium with a variation in refractive index, as in compressible flows around an object, will be deformed and refracted[2], bending towards the region of higher refractive index. This bending results in light and dark areas on the recording plane (Figure 2). In shadowgraphy of shock waves in a supersonic flow, the shock waves show up as a narrow band consisting of a light and a dark area. When shock waves around an object are studied, imaging the center plane of the object in a focused shadowgraphy system allows determining the shock location as the outer edge of the dark area. This forms the basis of the high-speed shock-tracking algorithm that was developed for this study.
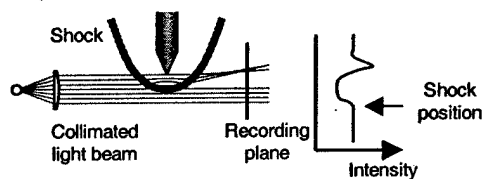

Figure 2: Principle of shadowgraphy

When operated in high-speed tracking mode, only the last 4 rows of any 1280x8 frame delivered by the camera are considered. Given that this typically represents less than 0.5mm in real terms (for the 5¼" viewing windows), the frames are vertically integrated to give a noise-reduced one-dimensional array. This data is then referenced with respect to an integrated strip from the same location in an image taken when there was no shock present. This step eliminates variations in intensity caused by uneven illumination and steady dirt on e.g. the windows of the wind tunnel. Figure 3 shows the integrated raw and referenced intensity data from a typical frame.
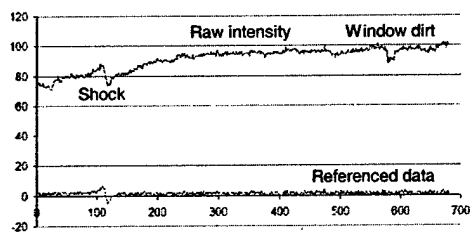

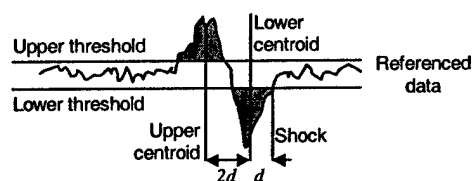
Figure 3: Raw and referenced intensity data

Figure 4: Shock position identification

While ideally the referenced signal should have a value of zero where unaffected by the shock, there is still some resilient noise present in the referenced data. Identification of the shock position was therefore achieved by the application of upper and lower thresholds (Figure 4). To determine these threshold values the referenced data-strip is divided into ten sections containing an equal number of pixels. For each section the minimum and maximum values are then calculated. The values of the third largest maximum and the third smallest minimum are then used as upper and lower thresholds, respectively. The center of the dark and of the bright parts of the shock were calculated as:

$$centroid_{lower} = \frac{\sum_{x \in A} |I_x - t_{lower}| \cdot x}{\sum_{x \in A} |I_x - t_{lower}|}$$

$$centroid_{upper} = \frac{\sum_{x \in B} |I_x - t_{upper}| \cdot x}{\sum_{x \in B} |I_x - t_{upper}|}$$

where I is the referenced intensity, t_{lower} and t_{upper} the threshold values and x the pixel position. In these equations, A is those pixels where $I < t_{lower}$ and B those pixels where $I > t_{upper}$.

The calculated positions of the upper and lower threshold are then used to determine the shock position, which is defined to be a distance d away from the position of the lower centroid ($3d$ from upper centroid), where d is half the distance between the upper and lower centroid (Figure 4):

$$shock\ position = centroid_{lower} + \frac{centroid_{lower} - centroid_{upper}}{2}$$

It can be seen that for a given number of pixels in the area considered to represent a shock, the accuracy of the calculated position is dependent on the intensity and distribution of noise within the referenced intensity data. Assuming the noise is randomly distributed, and the pixel intensities beyond the thresholds form symmetrical distributions, then the error in the calculated position will tend to zero. In the worst case however, where the noise is at its maximum and acting to increase the recorded intensity of one half of the width of the shock, and decrease the intensity on the other half, the error in calculated position is given by:

$$worst\ error = \frac{n \cdot \left(a/_2\right)^2 + n \cdot \left(b/_2\right)^2}{\sum_{x \in A} |I_x - t_{lower}| + \sum_{x \in B} |I_x - t_{upper}|}$$

where n is the maximum noise intensity, and a and b the number of pixels in A and B, respectively. The positional error will therefore lie between $0 \pm$ (worst-case error).

4. FLOW CONFIGURATION

The system was tested on a supersonic 8x8" wind tunnel at the Gas Turbine Laboratory of MIT. An aspirated nozzle, shown in Figure 5, was placed in the center of the vertical test section, pointing downwards, in the opposite direction to the tunnel flow. The nozzle-exit was placed at the level of the center of 5¼" diameter optical access windows.
Air can be blown through the nozzle generating an underexpanded free jet flow. With this configuration in the wind tunnel, different types of flow can be studied. Firstly, the wind tunnel flow around the nozzle, generating steady shock waves; secondly, the free jet flow from the nozzle; thirdly a combination of the two. By varying the pressure of air passing through the nozzle, in the opposite direction to the tunnel flow, the position of the shocks generated by the wind tunnel flow preceding the nozzle can be modulated.
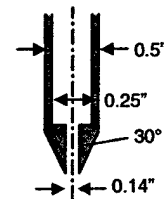
Figure 5: Nozzle design, sizes in inches

The through-nozzle flow is controlled using a simple rotary valve, which enables modulation up to several kHz. The pressure of the resulting flow was varied between approximately 10 and 20psi generating a jet flow at Mach number varying between $M = 1$ and $M = 2$.

The tunnel parameters for the results presented are as follows:

Mach number	2.06
Total pressure	15.3 psi
Static pressure	1.63 psi
Total temperature	100°F

5. RESULTS

Figure 6 shows the still view when there is no flow in the tunnel, but only the underexpanded free jet flow generated by the nozzle at 20psi. The air leaving the nozzle is supersonic and forms a series of shock diamonds, diminishing in strength after approximately 4 nozzle diameters. For increased clarity for all subsequent results shown here, a background image is taken in each case, without a flow present, which is then subtracted from the flow image. This image in turn is then normalized. The result is shown in Figure 7 for the flow in Figure 6. The bright and dark edges that appear on the nozzle after referencing show that the nozzle changes its position when flow is passing either through or past it. All still view results given used an exposure of 10 s.
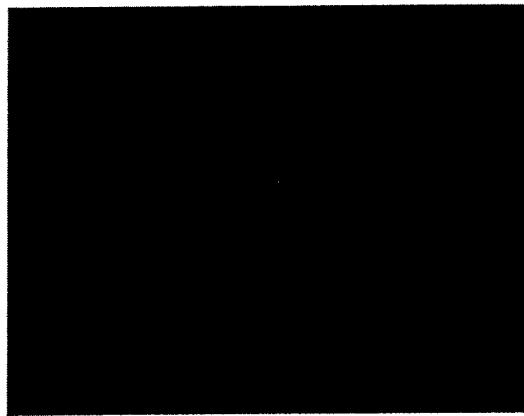

Figure 6: Still view of nozzle flow only. Total pressure: 20 psi   Figure 7: Referenced still view of nozzle flow only (cf. Figure 6)

Figure 8 shows the still view when the tunnel is operating at Mach $M = 2.06$, without a through-nozzle flow. A complex shock pattern is seen. Figure 9 shows the still view with tunnel flow *and* steady through-nozzle flow (at total pressure P_j = 20 psi). The multiple shocks can be seen to reduce to a single strong bow shock at an increased standoff distance from the nozzle, and another shock system with inverted density gradient is seen in front of the nozzle.
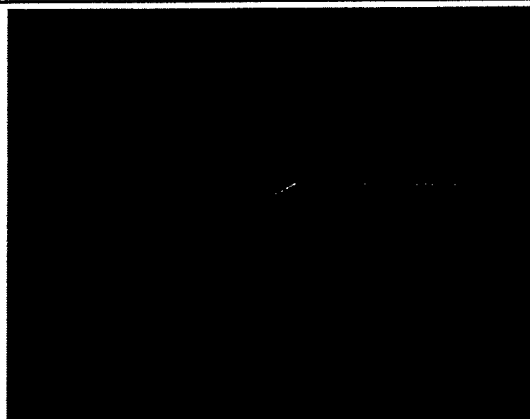
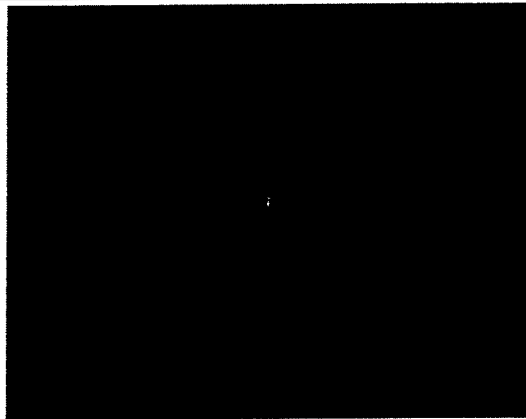Figure 8: Referenced still view of tunnel flow only. $M = 2.06$

Figure 9: Referenced still view tunnel+jet. $M=2.06$, $P_j= 20$ psi

When the through-nozzle flow - and therefore shock position - is steady, the spatial-temporal streak view is identical to the still view. When the through-nozzle jet flow is modulated however, a clear modulation of the shocks is shown in the streak view. Figures 10 and 11 show the spatial-temporal streak view when the through-nozzle flow is modulated between 10 and 20 psi at 80Hz and 550Hz respectively. In both cases the bow-shocks are affected the strongest, as shown by the clear periodicity. The effect also shows up in the shock closest to the bow-shock as well as in the ones originating close to the cone-cylinder transition. The diverging shocks going from the nozzle exit and the vertical shock at their endpoints (Mach-disk) do not show signs of unsteadiness. In Figure 10 about 6-7 oscillations are seen in the bow-shock; at a framing rate of 12 fps this would correspond to a frequency of $[(1/12)/6.5]^{-1}$, i.e. ~78 Hz. For the flow in Figure 11, where about 44 oscillation periods are seen, the estimate is ~530 Hz. Note that the modulation frequency could only be set indirectly, and the resulting frequency could not be determined accurately from the valve motor. From the shock tracking experiments described later it was found that the set frequency was typically about 5% higher than the frequency determined from the tracking measurements. Thus, the number of oscillations in the image gives a reasonable estimate of the oscillation period in the flow based on the framing rate.

Figure 10: Spatial-temporal streak view of 80Hz oscillation

Figure 11: Spatial-temporal streak view of 550Hz oscillation

Increasing the total pressure for the modulated nozzle flow to above 20 psi results in an unstable wavering, as shown in Figure 12. In this case, a clear disturbance is seen not only in the bow-shock ad the hemispherical one closest to it but also in all other shocks. The spatial-temporal streak view clearly depicts the irregular motion of the shock wave compared to those in Figures 10 and 11, whereas an instantaneous view such as Figure 13 offers no such information.

The still images and spatial-temporal streak view images are complementary, suggesting in this case that the bow shock remains smooth and is displaced in its entirety (horizontally in the images), but not at a regular oscillation period.
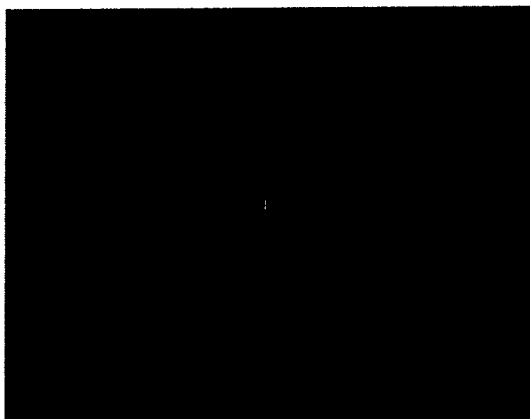

Figure 12: Spatial-temporal streak view of unstable oscillation

Figure 13: Still view of oscillating shock

Running the camera in tracking mode calculates the horizontal displacement of one part of the shock approximately 980 times a second. Figure 14 shows a typical position plot for a regularly oscillating shock, where the position was measured along the central axis of the nozzle. The amplitude of oscillation equates to 16 pixels, which is just under 2mm in real terms, and the FFT analysis presented in Figure 15 shows that it has a frequency of 76Hz.
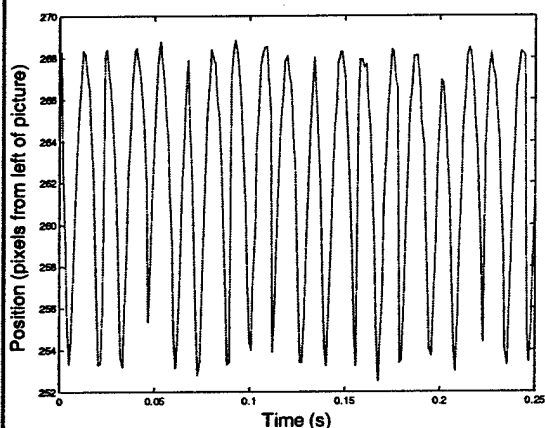

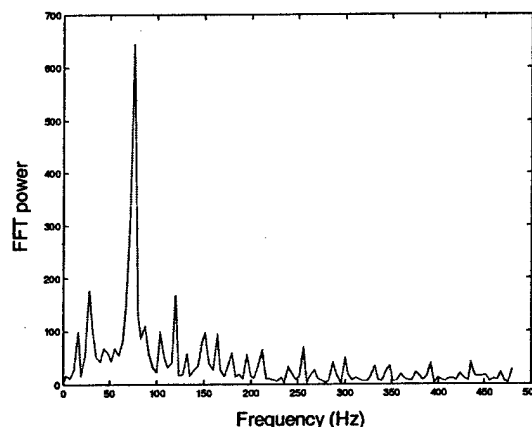Figure 14: Position plot of oscillating shock wave

Figure 15: FFT of shock oscillation

Examination of the pixel intensities at any one instance show that the bright and dark areas that form the shock are very close to being symmetrical distributions, meaning that the worst-case position error may be calculated using the equation described previously. For the data shown, this equates to approximately 0.6 pixels, or 4% of the total oscillation amplitude.

6. SHOCK ANGLE MEASUREMENT

The use of a single camera in tracking mode allows high-speed measurement of shock position, but not of shock angle, which may be useful in the study of unsteady oblique shock waves. To determine the shock angle for a simple straight oblique shock wave, at least two shock positions are required. In order to achieve such measurements, two daisy-chained cameras were run in tracking mode simultaneously. The cameras were mounted either side of a beamsplitter, placed after

the imaging lens, and positioned to view the same area. The gains were adjusted to compensate for the non-equal reflectance/transmittance of the beamsplitter. When running in tracking mode, the sensor subwindow regions were set such that one camera was viewing an area above the other (Figure 16). Calculation of the shock angle from the resulting two positions is a simple matter of trigonometry.

Figure 17 plots the position of the bow shock in the combined nozzle-tunnel flow oscillating at 19Hz, as measured by two cameras, and the resulting shock angle. It can be seen that the angle deviates relatively little from 36° to the horizontal, increasing to 38° only when the shock is in its most right hand position. Although the inability of the FireWire interface to send frames from both cameras instantaneously would produce an apparent change in angle at points of most rapid positional change, the non-sinusoidal shape of the angular plot suggests that the shock angle does indeed change slightly when the shock is further from the nozzle.
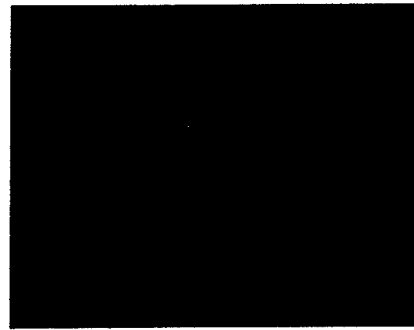

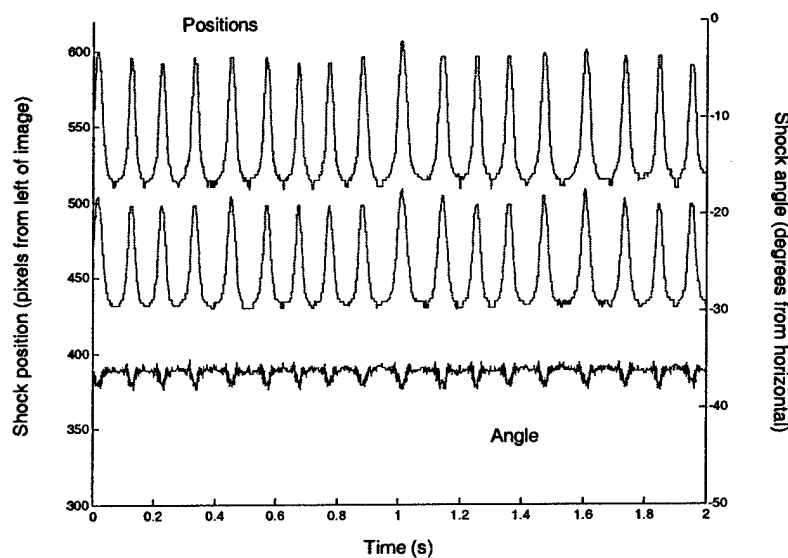Figure 16 Using two cameras to determine shock angle at high frame-rate

Figure 17: Graph showing movement of bow-shock in oscillating nozzle-tunnel flow as measured by two cameras registering shock movement at two different positions (top part). From these two positions, the angle of the bow-shock with respect to the nozzle axis can be calculated (bottom part).

7. CONCLUSIONS

The use of a low-cost CMOS sensor to achieve both full field-of-view mega-pixel flow visualizations as well as high-speed shock position tracking has been demonstrated in a low-cost digital focused shadowgraphy system tested on unsteady supersonic flow fields. The system uses three recent advances in technology: a robust, low-cost white light LED as a light source; a CMOS camera for digital recording, allowing direct control over the size of the captured image, making it possible to trade size of image for image frame-rate; and fire-wire communications technology to transmit the images directly to a computer, which can then be used as input for a shock control system.

The light source can be modulated at high speed to give microsecond flashes, which allows freeze-frame imaging of unsteady events at a constant illumination level. The use of a CMOS camera enables data to be recorded in three basic modes of operation: a still full field-of-view freeze-frame mode, a windowed tracking mode and a continuous full field-of-view mode. This latter mode is based on the fundamental mode of operation of CMOS cameras and allows a new type of visualization to be obtained: spatial-temporal streak imaging. Although the images obtained in this mode are by no means trivial to interpret, they do help in the immediate identification of regions of instability.

Expanding the system with a second identical camera looking at the same flow region using a beam-splitter allows high-speed simultaneous tracking of features at different locations in the flow. Thus, e.g. the local angle of shock waves can be determined and monitored for changes.

As the CMOS camera uses FireWire connection, image processing can be performed immediately in the host computer. Thus, the system presented here can track the position of a flow feature at a rate of 980 Hz (determined by camera frame rate). This position information can be sent directly to a flow control-system, with a delay $<100\mu s$, allowing immediate feedback as input for a flow adjustment and controlling device, e.g. for controlling shock position in a supersonic inlet.

The constructed system can be generalized in several ways. Because of the use of conventional diode technology there is the prospect of making three dimensional shock structure measurements at relatively low cost. This could be achieved e.g. by creating an array of sources and cameras and developing a tomographic approach[8]. This approach has been previously demonstrated on bespoke laboratory systems[8], however, the progress of the available technology now makes a low-cost rugged and digital approach a reality. Equally the challenge is presented of making an intra-passage transonic rotor shock measurement to provide active control within the gas turbine engine itself. The current system, as described, has the potential to be both miniaturized and ruggedized for this purpose.

ACKNOWLEDGEMENTS

REFERENCES

1. DARPA, "Quiet Supersonic Platform (QSP)" (2003), retrieved http://www.darpa.mil/tto/programs/qsp.html.
2. W. Merzkirch, *Flow Visualization*, 2nd ed. (Academic Press, 1987).
3. S. R. Donohoe and W. J. Bannink, "Surface Reflective Visualizations of Shock-Wave/Vortex Interactions Above a Delta Wing," AIAA Journal 35(10), 1568-1573 (1997).
4. B. H. Timmerman, *Holographic Interferometric Tomography for Unsteady Compressible Flows*, PhD Thesis Delft University of Technology (Eburon P&L, Delft, the Netherlands, 1997).
5. A. Ben-Yakar and R. K. Hanson, "Ultra-fast-framing schlieren system for studies of the time evolution of jets in supersonic crossflows," Experiments in Fluids 32, 652-666 (2002).
6. J. R. Gord, C. Tyler, K. D. Grinstead, G. J. Fiechtner, M. J. Cochran, and J. R. Frus, *Imaging strategies for the study of gas turbine spark ignition*, Optical Diagnostics for Fluids/Heat/Combustion and Photomechanics for Solids (SPIE, Denver, Co, USA, 1998), Vol. 3783, pp. 352-361.
7. Brookstone Company Inc., Mexico MO, USA.
8. B. H. Timmerman and D. W. Watt, *Tomographic holographic interferometric study of self-excited compressible jet flows*, Optical Technology in Fluid, Thermal, and Combustion Flow III (SPIE, San Diego, Ca USA, 1997), Vol. 3172, pp. 307-315.

FEDSM2001–18275

ACTIVE CONTROL OF
INTEGRATED INLET / COMPRESSION SYSTEMS:
INITIAL RESULTS

Douglas G. MacMartin[1]
Control and Dynamical Systems
Caltech

Ashish Verma
Aeronautics and Astronautics
MIT

Richard M. Murray
Control and Dynamical Systems
Caltech

James D. Paduano
Aeronautics and Astronautics
MIT

ABSTRACT

Substantial reductions in aircraft size are possible if shorter, more aggressive, serpentine inlet ducts are used for low-observability constrained propulsion installations. To obtain this benefit, both inlet separation and compressor stall dynamics must be controlled. In this paper the integrated control of this coupled inlet/compression system is considered. Initial results are shown using separation point actuation to control both separation and stall dynamics. Calculations show that separation can be substantially reduced with approximately 1.2% core flow, based on scaling previous results. Simulation results using a medium fidelity model show that proportional control of distortion has little effect on stall behavior.

1   INTRODUCTION

The inlet to an aircraft propulsion system must supply flow to the compressor with minimal pressure loss, distortion, or unsteadiness; the former reduces the overall system performance, while the latter effects can result in stall or surge of the compressor. For many military applications, the inlet design is also constrained by low observability requirements. To reduce the radar signature from the compressor face, a serpentine inlet is typically used to block line-of-sight. Similar buried propulsion system installations have also been considered for some configurations of the commercial blended wing body design. While the inlet length that is required to avoid separation and its associated losses may not be a significant design driver for some vehicles, in other configurations (such as uninhabited air vehicles), the inlet may drive the size of the overall vehicle. Therefore,

technologies such as flow control that can enable more aggressive inlets can have significant overall system benefit.

In order to make the vehicle smaller through the use of such technologies, constraints imposed by the compressor dynamics may also need to be considered. Instability of these dynamics is typically avoided by introducing a stall margin; i.e. by operating the compressor at less than the peak pressure rise to allow for inlet distortion, transients, and wear. This requires the use of additional stages to obtain the desired net pressure rise from the compression system, resulting in a heavier engine.

Current aircraft designs typically consider the compressor and inlet as separate sub-systems, where the connection between them is given as a pressure recovery and distortion specification [1, 2] that must be met at the Aerodynamic Interface Plane (AIP). This approach is not entirely adequate for today's aircraft, due to the coupling between the inlet and compressor performance and stability, and it is inadequate if advanced inlet or compressor control approaches are to be designed.

The compressor behavior must be considered together with the inlet for several reasons. First, reducing the amount of stall margin required for stability enables the compressor to operate at higher pressure rise and potentially improved efficiency, allowing reduced engine size and fuel requirements that may be essential in obtaining the reduced vehicle size associated with a shorter inlet. Second, any technology that enables a shorter inlet to retain the same pressure recovery as a current technology inlet would be inadequate if it does not also address distortion and unsteadiness. However, such technology might be very complementary with compressor stability control; rather than requiring the shorter inlet to provide the same distortion as the original inlet, allow a higher distortion and compensate
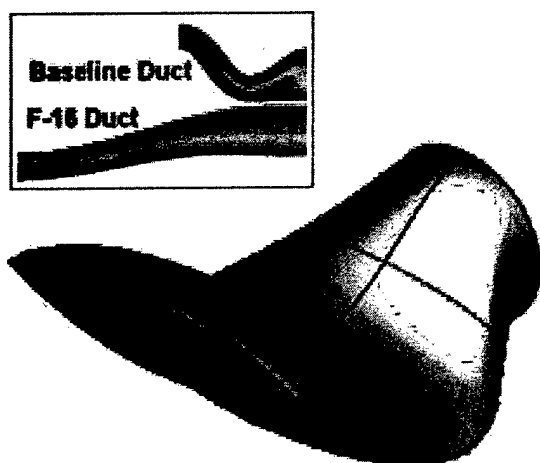

Figure 1: Aggressive L/D 2.5 serpentine inlet duct, and comparison with current F–16 inlet. This compact design involves two turns, diffusion, and change in shape.

Figure 2: Matrix of control options, including both direct, and indirect control paths.

by controlling the compressor. Third, the physical systems are coupled, both in a quasi-steady sense, and through the dynamics, and thus not only must the controllers be designed together, but there is the potential for synergistic control of both physical systems with the same actuators. Thus, an integrated approach must be taken to the control of the inlet and compressor *system*.

A preliminary systems analysis has been conducted by Northrop Grumman for an uninhabited combat air vehicle (UCAV). A typical serpentine inlet for this class of vehicles is shown in Figure 1; the inlet includes turning, diffusion, and a shape change in a compact configuration. The system study indicates the potential for achieving a significant reduction in vehicle TOGW if an inlet with length to diameter ratio (L/D) of 1.5 is used, rather than an L/D 3.0 inlet that is achievable with current technology. The focus of the effort in the program reported on herein is to develop technology that enables the shorter inlet to be viable. The system analysis shows that one must not only retain the pressure recovery of the unseparated inlet, but also control the compressor dynamics to allow a smaller engine to be used, operating closer to the stall boundary, while tolerating any increase in distortion or unsteadiness from the controlled aggressive inlet. The benefits study also indicates that bleed levels up to about 2% of total mass flow could be tolerated and still yield significant system benefit.

Potential actuator locations to control the compressor and separation dynamics include compressor face actuation (CFA), and separation point actuation (SPA). The overall control options for the program are laid out in Figure 2, and the possible architecture shown schematically in Figure 3. Both the control of the compressor through CFA, and of separation through SPA, have been considered previously.
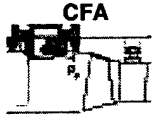
The indirect paths, control of separation using CFA, or control of stall through SPA, have not been examined. These indirect paths provide the potential for synergy if the overall dynamics can be controlled through a single set of actuation hardware. Furthermore, examining controllability also provides a means for assessing the degree of dynamic coupling between the systems. This paper provides initial results on the first row of the matrix in Figure 2, control using separation point actuation. Since prior work exists on control of separation from SPA, more emphasis will be placed on the analysis of controllability of the indirect path, from SPA to stall dynamics.

The use of air injection actuators at the compressor face to stabilize the compressor dynamics has been demonstrated successfully in multiple tests, both with steady injection and with dynamic feedback to modulate unsteady injection [3, 4]. The latter results rely on a good understanding of the compressor dynamics using a Moore-Greitzer approach [3, 5, 6], which this paper will build upon. Air injection alters the blade passage flow properties in the rotor by altering the incidence and momentum in the tip clearance region. Typical experimental results demonstrate at least a 50% reduction in the required compressor stall margin, with a maximum bleed of roughly 1.5% of the overall flow [4, 7].

Several researchers have looked at using flow control to improve the characteristics of aggressive serpentine inlet ducts. Lockheed and NASA [8] used steady injection to simulate vortex generators to modify the secondary flows introduced by turning ducts. Roughly 1% flow bleed was used on a L/D 2.5 inlet. VPI [9] demonstrated boundary layer suction or blowing on a similar geometry. Significant work has also been done using vortex generators (see [8] and references therein). Unsteady flow control techniques have received considerable attention recently and shown to be quite effective in controlling separation over two-dimensional air-
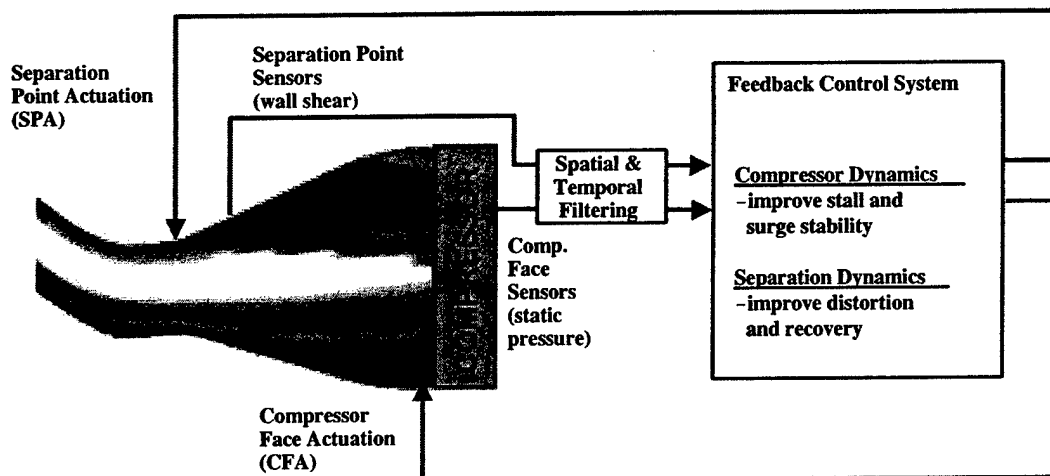
2

Figure 3: Control architecture. Possible actuator locations for control of the coupled inlet/compressor system include the Separation Point (SPA) and at the Compressor Face (CFA).

foils, e.g. [10, 11] and diffusers, e.g. [12, 13]. However, little work has been done using unsteady injection in complex 3-dimensional flow fields.

The remainder of this paper looks briefly at the coupled inlet/compressor dynamics, and provides a preliminary estimate of the actuator authority required to control separation using unsteady excitation at the separation point. The same actuation approach is then considered for controlling the compressor stall dynamics. The influence of separation point control on the compressor is modeled as the ability to dynamically vary the distortion at the compressor face, and this is introduced into existing Moore-Greitzer based compressor models. Analysis of controllability is then considered.

2 PHYSICS

An L/D 2.5 inlet similar to that shown in Figure 1 has been analyzed both computationally and experimentally. The geometry chosen results in some separation at test conditions representative of cruise, and although subsequent design refinement indicates the potential for achieving this inlet length without separation, the flow features of this duct can reasonably be expected to be somewhat characteristic of any more aggressive inlet. Any serpentine inlet will result in strong secondary flows from the turns [14]. The inlet under study also has a significant change in cross-sectional shape, starting from a high aspect ratio rectangular cross-section, and transitioning to circular through the diffuser. The test results indicate that at cruise, the dominant separation is at the entrance to the diffuser. The upper surface, and, to a lesser extent, the lower surface, experience significant adverse pressure gradients due to the diffusion, the cross-sectional shape change, and the turning. As the flow sepa-
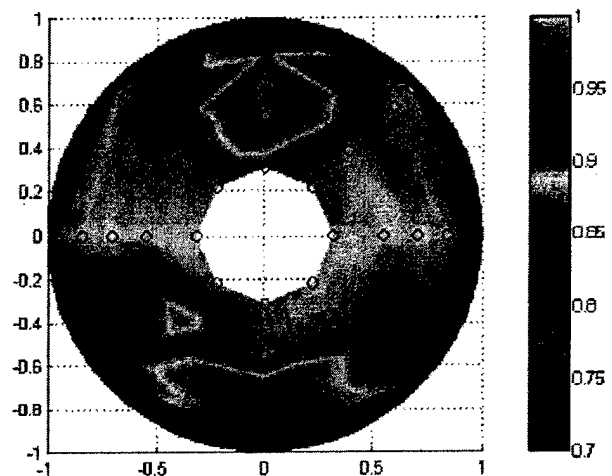
Figure 4: Measured distortion at the Aerodynamic Interface Plane (AIP). The anomolous point in the lower left quadrant is due to a bad pressure sensor.

rates on the upper surface, attached flow rushes in from the side, resulting in a detached pair of streamwise vortices and corresponding pressure distortion that persist down to the AIP, as shown in Figure 4. Thus significant 3-dimensional structures exist both upstream of separation, due to secondary flows, and downstream of the separation, due to the circumferential variation in pressure gradient around the duct.

The primary influence of separation structures on compressor performance is through the total pressure distortion pattern that results. As shown in Figure 4, total pressure at

3

the compressor face is severely nonuniform. The compressor sees this non-uniformity as a circumferential variation in blade incidence[2]. If the compressor has no IGVs, this incidence variation is experienced directly by the rotor as an unsteady forcing function, as the blades rotate through the distorted inlet flow. Even with IGVs, total pressure distortion impacts compressor stability dramatically, by altering the compressor's stall dynamics.

The term 'stall dynamics' refers to the time evolution of perturbations on the steady flow through the compressor [5, 6]. These perturbations take the form of cells of nonuniform axial velocity, which typically rotate at a fraction of the rotor speed. The growth of these cells to very large amplitude results in rotating stall, a debilitating compressor state consisting of a very low flow region rotating around the compressor annulus. In this region the compressor blades are stalled, blade passage blockage is high, and delivered pressure rise is very low. The overall compressor either becomes 'hung' in this violent state, or further degenerates into surge, a one-dimensional oscillation that can damage the engine.

The inlet section of the compressor is a boundary condition on the internal flow in the compressor, both in the steady and the unsteady sense. A steady-state inlet distortion changes the steady operating condition of the compressor, setting up a non-uniform flow field through which stall perturbations propagate [15]. This effect is invariably destabilizing, because inlet distortion is always in the form of local flow deficits. When the inlet flow is itself the result of dynamic events, such as unsteady three-dimensional separation, the *unsteady* interaction between the compressor and inlet becomes important. This interaction is less well understood, and is the subject of ongoing research.

3   CONTROL OF SEPARATION

A preliminary analysis has been done using existing data to estimate the requirements for controlling separation from the separation point for an aggressive, L/D 1.5 inlet. For cruise, the conditions at the separation point will be taken as a Mach number of 0.65, mass flow $\dot{m}_t$ of roughly 50 kg/s and area A approximately 0.25 m^2.

Unsteady excitation is considered rather than steady, in order to minimize authority requirements. Existing data uses a non-dimensionalized momentum coefficient,

$$C_\mu = \frac{\rho_i hl \langle u^2 \rangle}{\rho A_s U_\infty^2} \qquad (1)$$

where ρ_i and ρ are the densities of the injected and free-stream air respectively, h and l are the width and spanwise

[2]Note that, roughly speaking, a total pressure deficit manifests itself as a reduction in axial velocity into the compressor. The incidence of a rotating compressor blade is the vector sum of this velocity and the velocity induced by rotation. As axial velocity is reduced, blade incidence increases; at very low axial flow the blade stalls, much like an aerofoil stalls at high angle of attack.

length of the separation actuator, $\langle u^2 \rangle$ is the mean-square amplitude of the oscillatory component of injected air, A_s is the separated area, and U_∞ is the velocity at the separation point. A reference length can be defined as $x_{ref} = A_s/l$. The non-dimensionalized frequency of excitation is then given by

$$F^+ = \frac{f x_{ref}}{U_\infty} \qquad (2)$$

where the optimum frequency has been shown to be near $F^+ \sim 1$ (see [10] for a thorough discussion of the impact of frequency on both preventing separation and on reattachment). Data taken at UTRC in a two-dimensional diffuser [13, Figure 7] provide a comparison of both a forced aggressive diffuser, and the best unforced diffuser. $C_\mu \sim 0.2\%$ is shown to yield comparable pressure recovery in the aggressive geometry to the pressure recovery of a longer, unseparated diffuser. Thus this authority level will be assumed to enable the more aggressive L/D 1.5 inlet to yield the same pressure recovery as the longer, unseparated, L/D 2.5 inlet. It should be noted, however, that while the pressure recovery is maintained, the distortion and unsteadiness of the unseparated inlet may not be maintained by the controlled aggressive inlet, and therefore additional control of the compressor dynamics may be required to make the overall coupled system viable.

To convert C_μ into a momentum requirement, the expected separated area must be estimated. This is based on the hypothetical L/D 1.5 inlet geometry shown in Figure 5. In the streamwise direction, the boundary layer is assumed to separate at the entrance to the diffuser, as in the current L/D 2.5 inlet, and assumed not to reattach until the AIP, as shown in the shaded region of Figure 5(a). In the spanwise direction, due to the change in shape of the duct, only the upper and lower surfaces experience adverse pressure gradients, and due to the curvature, the gradient on the upper surface is much worse than the lower. Therefore, the upper surface is assumed to separate over the spanwise length that will experience adverse pressure gradient, as shown in the shaded region in Figure 5(b). These are worst case assumptions, and the actual inlet is likely to be better, and thus to require less authority to control.

The resulting estimate of required momentum $\rho_i hl \langle u^2 \rangle$ is 30 kg m/s^2, much larger than in many other applications in the literature. This implies that, although many results have been obtained with zero mean injection (synthetic jet), it is doubtful whether any practical actuator could be built for this application that would have sufficient authority. While modulating steady injection has been shown [16] to be less effective than pure unsteady injection without a bias, its implementation is likely to be sufficiently easier so as to offset any penalty. Compressor bleed is available, and very high unsteady authority can be readily obtained. While the practicality of synthetic jets needs to be verified in an ultimate application, for the preliminary analysis, modulated injection will be assumed, and authority will be converted
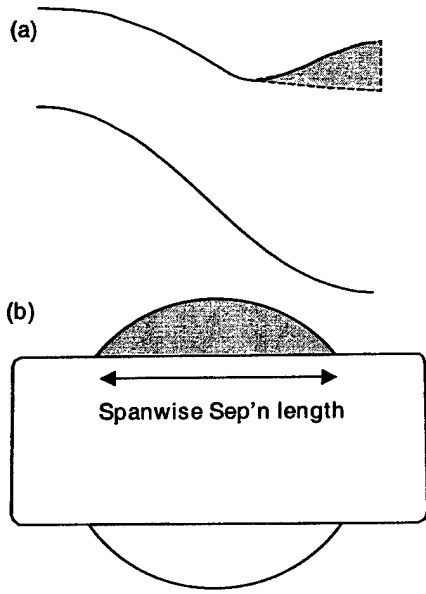
Figure 5: Expected separated area for aggressive, L/D 1.5 inlet. (a) streamwise cross-section, (b) spanwise cross-section at the entrance to the diffuser and at the AIP.

Figure 6: Impact of separation point actuation on compressor via modulation of distortion.

into an equivalent percentage bleed.

To convert the momentum requirement to a mass flow requirement, either the exit velocity of the injected flow, or the actuator slot width h must be specified. If the injected flow velocity varies according to $U_i = kU_\infty (1 + \sin(\omega t))$ for some k, then the momentum coefficient in Eq'n 1 can be expressed in terms of the mean mass flow injected $\dot{m}_i$ and the total inlet mass flow $\dot{m}_t$ as

$$C_\mu = \frac{1}{2} k \left(\frac{\dot{m}_i}{\dot{m}_t} \right) \left(\frac{A}{A_s} \right) \qquad (3)$$

Choosing the mean velocity ratio k so that the peak injected flow is nearly choked at the slot exit yields a bleed requirement of 1.2% of the total duct mass flow through a 2.3 mm wide slot. While this requirement seems high, it should be noted that the L/D 1.5 inlet is extremely aggressive, the assumed separated area is likely conservative, and that with high speed flow, the ratio $\langle u^2 \rangle_i / U_\infty^2$ is constrained to be relatively low.

Existing actuator technology for unsteady flow control includes synthetic jets (demonstrated using piezoelectric [17], electro-magnetic [18], and PVDF actuation), modulated injection (using various types of air valves [19], pulsed combustion [20], or fluidic approaches), and other advanced concepts (e.g. glow discharge). The required momentum for this application is significantly higher than the authority currently obtainable with any single existing synthetic jet actuator. However, existing air valves used in compressor stability control can deliver sufficient authority with rela-
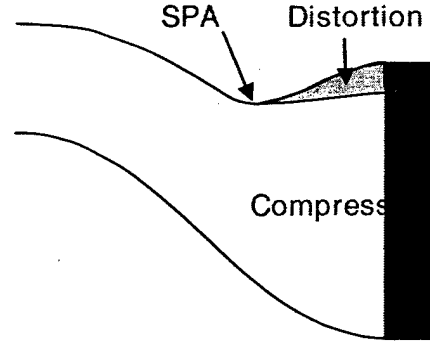
tively few separate devices. The Moog actuators used in [4, 7] can each deliver 13% of the requirement. Therefore, despite the high levels of authority projected by this analysis, it is expected that off the shelf actuation can be used.

The preceding authority analysis indicates that unsteady excitation to control the separation dynamics in the aggressive inlet is likely to be feasible from an actuation perspective. Additional work is required to understand the impact of three-dimensionality of the flow field on the control implementation.

4   MODELING

Forcing and control of the compressor rotating stall dynamics can be affected by various means; in this paper we investigate the feasibility of control from the separation point, via modulation of the inlet distortion. Regardless of how effective any separation control approach may be in the inlet, some residual distortion is likely to exist. Distortion can have a significant impact on stall behavior, and even steady control to vary the azimuthal distortion pattern can significantly improve stall [21]. One means by which control at the separation point can impact the compressor dynamically is by modulating the residual distortion, as indicated schematically in Figure 6. Thus, for analysis, the inlet and separation dynamics will be ignored, and the impact on the compressor dynamics of using feedback to modulate distortion will be assessed. The convective time delay between SPA and distortion at the compressor face in the L/D 1.5 duct is roughly 2 ms, while the time for a rotating stall cell to grow to full amplitude is roughly 2-3 cycles at 150 Hz, or 17 ms [4], hence ignoring the time delay is not critical to the analysis.

Previous work on compressor control has used a Moore-Greitzer approach to model the compressor dynamics [3, 6, 22, 23]. This model, shown schematically in Figure 7, has been proven quite accurate and effective. The system model includes the compressor, inlet and exit duct, and a plenum controlled by a throttle. The compressor is modeled as a
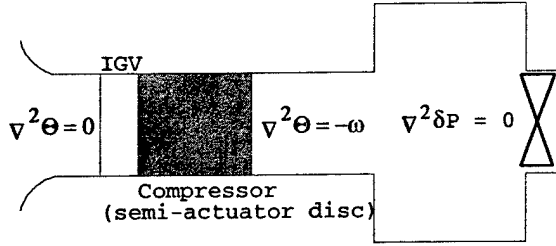
Figure 7: Schematic of Moore-Greitzer model.

semi-actuator disk. The flow upstream of the compressor is assumed to be potential. The plenum is large and acts as a mass storage device and captures the compressibility of the flow. The dynamics of the exit throttle are modeled as a pressure drop across an orifice. The compressor has a non-linear pressure rise map which is a function of the axial flow, the rotor inertia, the circumferential angle and the fluid inertia. Acceleration of the axial flow is driven by pressure rise across the compressor, which is in turn a function of the local flow. The inertial properties of the flow in the blade passages, the impedance properties of the upstream and downstream flow fields, and the inlet distortion together determine the eigenvalues of the system, which are circumferentially propagating waves. Instability of these waves results in rotating stall.

Summing the upstream, compressor, and the downstream dynamics leads to a set of PDE's:

$$\Psi(\theta, \xi) = \Psi_c\left(\Phi + \delta\phi\right) - l_c\frac{d\Phi}{d\xi} - \lambda\frac{\partial\delta\phi}{\partial\theta} - (\mu + m)\frac{\partial\delta\phi}{\partial\xi} \quad (4)$$

where Ψ is the average pressure rise coefficient, Φ is the average flow coefficient, $\delta\phi$ is the perturbation of the flow from the average, Ψ_c is the steady state compressor characteristic, γ is the throttle coefficient, and l_c, λ, m, and μ are parameters that depend on the compression system.

Mansoux et al. [6] proposed a high fidelity model by expressing higher harmonics in terms of the local flow using a discrete Fourier transform. This model takes the form

$$\dot{\phi} = \overline{E}^{-1}\left(-\overline{A}\cdot\phi + \Psi_c(\phi) - T\cdot\Psi\right) \quad (5)$$

$$\dot{\Psi} = \frac{1}{4B^2l_c}\left(S\cdot\phi - \gamma\sqrt{\Psi}\right) \quad (6)$$

where ϕ is the vector of flow coefficients at discrete points around the annulus, $\overline{A}$ and $\overline{E}$ transform ϕ into and out of the Fourier domain, $S = \frac{1}{2N+1}[1\ 1\ldots 1]$, and $T = [1\ 1\ldots 1]^T$. A purely Fourier description in the circumferential direction can also be adopted, although this description is most appropriate when the inlet flow is uniform [6].

To capture some of the realistic considerations, a model for the transient pressure losses across the rotor and stator is added to the collocated model [24, 25]; L_r and L_s are the total pressure loss across rotor and stator, and L_r^{ss} and L_s^{ss} are the steady state losses.

$$\Psi_c = \Psi_c^{qs} = \Psi_c^{isen} - L_r - L_s \quad (7)$$

$$\dot{L}_r = \frac{1}{\tau_r}\left(L_r^{ss} - L_r\right) \quad (8)$$

$$L_r^{ss} = \overline{R}\left(\Psi_c^{isen} - \Psi_c^{qs}\right) \quad (9)$$

$$\dot{L}_s = \frac{1}{\tau_s}\left(L_s^{ss} - L_s\right) \quad (10)$$

$$L_s^{ss} = \left(1 - \overline{R}\right)\left(\Psi_c^{isen} - \Psi_c^{qs}\right) \quad (11)$$

The states of the resulting Moore-Greitzer description are the axial flow at discrete points around the compressor annulus, the pressure in the plenum chamber, and auxiliary states describing time lags in the development of losses within the compressor.

The model has been extended to include the effects of distortion and its control via actuation. The inlet distortion is modeled as a distortion screen in the inlet duct and the resulting pressure loss is governed by the local flow coefficient. The distortion is modeled as an additional pressure loss at the rotor,

$$\Delta L_r^{ss} = \frac{1}{2}C_d\left(\theta\right)\phi(\theta)^2 \quad (12)$$

where $C_d < 0$ is the distortion screen parameter and its θ dependence determines the circumferential extent of the distortion.

To model the effect of SPA control, we assume that we can modulate the pressure loss due to distortion. For simplicity, we model this as a simple pressure addition at the rotor and we require that it never be larger than $C_d(\theta)\phi(\theta)^2/2$.

5 CONTROL OF STALL

Air injection immediately upstream of the compressor face has been demonstrated to be very effective in coupling with the compressor stall dynamics. Modulating the distortion should be expected to be less effective, as it only affects the local mass flow, and not the local angle of attack as air injection does. Modulating distortion should, of course, have some effect, simply because the mean distortion is being reduced. Therefore, to assess whether a dynamic feedback approach is better than simply using the available control authority to quasi-steadily minimize the distortion, the dynamic approach should be compared with the benefit obtained with the same mean, but steady reduction.

The approach taken here is to assume control (distortion reduction) dependent on the magnitude of the local flow perturbation, and to allow for a spatial lead or lag. This is roughly equivalent to varying the phase of the time dependent distortion reduction relative to the stall cell, while keeping the magnitude of the reduction constant. If the
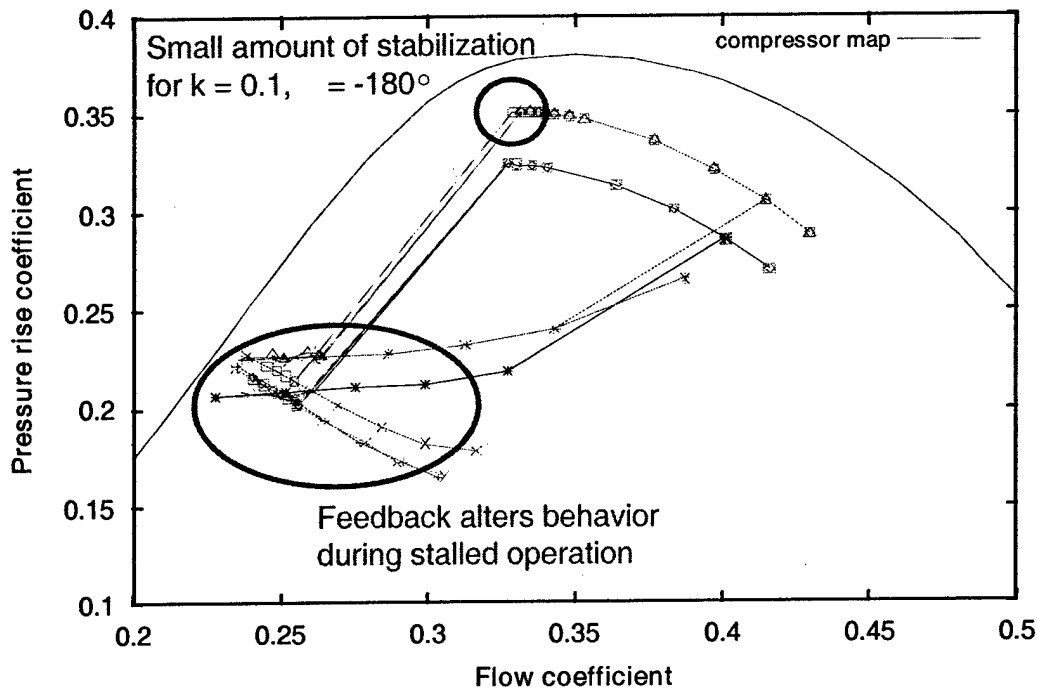
6

Figure 8: Simulation results. Top line shows the undistorted, uncontrolled compressor characteristic. The remaining two families of lines correspond to different control gains. Each line within each family corresponds to a different control phase.

stall margin does not depend on the phase but only on the gain, then clearly only the mean reductions are relevant.

Figure 8 shows the un-distorted compressor characteristic, and two families of controlled compressor characteristics corresponding to different gains. For the smaller gain (lower family of lines), there is roughly a 5% reduction in the mean distortion, for the larger gain (higher family), the mean reduction is roughly 50%. Within each family, the phase is varied between zero and 360°, and the resulting closed loop compressor characteristics are overplotted (not all phases are shown). At the higher gain, a very slight change in the stall point is noted, indicating a very weak dynamic controllability over stall. However, this change is negligible relative to the improvement in stall margin with the mean distortion reduction. There is also some effect on the post stall behavior, however, this effect is not useful.

The preliminary conclusion based on analysis presented herein is that the compressor stall dynamics are from a practical perspective not controllable from the separation point. From a systems perspective, these results imply that a combination of separation point and compressor face actuation may be the most viable option.

6 SUMMARY

An integrated approach for controlling coupled inlet (separation) and compressor (stall) dynamics is required to en-able an optimized system yielding significant aircraft size reductions by reducing the engine inlet length. Preliminary analysis for controlling both separation and compressor stall dynamics using only separation point actuation has been conducted. This study indicates that dynamic controllability of the compressor via SPA is poor. While further work may revisit this conclusion using a low order integrated system model, it appears likely that compressor face actuation will be required as part of the overall control solution.

Control of separation dynamics at the separation point has been assumed to be feasible based on prior work, and a preliminary assessment of actuator authority requirements for an aggressive inlet geometry would suggest that this approach may be viable. However, significant work remains in understanding the separation dynamics, particularly due to the complex three-dimensional nature of the flow field. Furthermore, if CFA will be present to control stall dynamics, it is reasonable to ask whether these actuators could also affect the separation dynamics either by changing the downstream acoustic boundary condition, or by sending acoustic waves upstream to interact with the vorticity shedding at the separation point (as in [26]). This research is in progress.

Overall, it appears likely that by approaching the problem from an integrated perspective, a viable flow control solution can be found that will enable significant reductions in inlet length, and hence vehicle size. The optimal

mix of compressor face and separation point actuation will be experimentally determined based on a trade-off of performance, cost, weight, and system complexity.

Acknowledgements

References

[1] SAE Committee S-16, Turbine Engine Inlet Flow Distortion, "Aerospace recommended practice: Gas turbine engine inlet flow distortion guidelines," tech. rep., Society of Automotive Engineers, June 1977. ARP-1420.

[2] SAE Aerospace Council Division, Technical Committee S-16, "Aerospace information report: Inlet total-pressure-distortion considerations for gas-turbine engines," tech. rep., Society of Automotive Engineers, May 1983. AIR-1419.

[3] R. D'Andrea, R. L. Behnken, and R. M. Murray, "Active control of an axial flow compressor via pulsed air injection," ASME Journal of Turbomachinery, vol. 119, no. 4, pp. 742-752, 1997.

[4] H. J. Weigl, J. D. Paduano, L. G. Frechette, A. H. Epstein, E. M. Greitzer, M. M. Bright, and A. J. Strazisar, "Active stabilization of rotating stall in a transonic single stage compressor," Journal of Turbomachinery, vol. 120, pp. 625-636, 1998.

[5] E. M. Greitzer and F. K. Moore, "A theory of post-stall transients in axial flow compression systems part I: Development of equations, and part II — application," ASME Journal of Engineering for Gas Turbines and Power, vol. 108, pp. 68-97, 1986.

[6] C. A. Mansoux, D. L. Gysling, J. D. Setiawan, and J. D. Paduano, "Distributed nonlinear modeling and stability analysis of axial compressor stall and surge," in American Control Conference, 1994.

[7] K. L. Suder, M. D. Hathaway, S. A. Thorp, A. J. Strazisar, and M. B. Bright, "Compressor stability enhancement using discrete tip injection," in Proceedings of ASME TUR-BOEXPO, 2000. 2000-GT-650.

[8] J. W. Hamstra, D. N. Miller, P. P. Truax, B. A. Anderson, and B. J. Wendt, "Active inlet flow control technology demonstration," The Aeronautical Journal, pp. 473-479, 2000.

[9] W. F. Ng and R. A. Burdisso, "Active acoustic and flow control for aeropropulsion," in AIAA Aerospace Sciences Conference. AIAA 2001-0220.

[10] B. Nishri and I. Wygnanski, "Effects of periodic excitation on turbulent flow separation from a flap," AIAA Journal, vol. 36, no. 4, pp. 547-556, 1998.

[11] D. Greenblatt and I. J. Wygnanski, "The control of flow separation by periodic excitation," Progress in Aerospace Sciences, vol. 36, pp. 487-545, 2000.

[12] M. Amitay, D. Pitt, V. Kibens, D. Parekh, and A. Glezer, "Control of internal flow separation using synthetic jet actuators," AIAA 2000-0903.

[13] D. C. McCormick, "Boundary layer separation control with directed synthetic jets," in AIAA Aerospace Sciences Conference. AIAA 2000-0519.

[14] B. A. Reichart and B. J. Wendt, "Improving diffusing S-duct performance by secondary flow control," in AIAA Aerospace Sciences Conference, 1994. AIAA-94-0365.

[15] T. P. Hynes and E. M. Greitzer, "A method of assessing effects of circumferential flow distortion on compressor stability," ASME Journal of Turbomachinery, vol. 109, pp. 371-379, 1987.

[16] I. Wygnanski, "Some new observations affecting the control of separation by periodic excitation," in Fluids 2000. AIAA 2000-2314.

[17] F.-J. Chen, C. Yao, G. B. Beeler, R. G. Bryant, and R. L. Fox, "Development of synthetic jet actuators for active flow control at NASA Langley," in Fluids 2000. AIAA 2000-2405.

[18] D. C. McCormick, S. A. Lozyniak, D. G. MacMartin, and P. F. Lorber, "Compact, high-power boundary layer separation control actuation development," in ASME Fluids Engineering Division Summer Meeting, 2001. FEDSM2001-18279.

[19] R. G. Berndt, H. J. Weigl, J. D. Paduano, and A. H. Epstein, "Experimental techniques for actuation, sensing, and measurement of rotating stall dynamics in high-speed compressors," in SPIE International Symposium on Aerospace/Defense Sensing and Dual-Use Photonics: Sensing, Actuation, and Control in Aeropropulsion, 1995.

[20] M. Allen and A. Glezer, "Compact combustion-powered actuation for aerodynamic control," in ASME Fluids Engineering Division Summer Meeting, 2001.

[21] J. P. Longley and E. M. Greitzer, "Inlet distortion effects in aircraft propulsion system integration," May 1992. AGARD-LS-183.

[22] J. D. Paduano, L. Valavani, A. H. Epstein, E. M. Greitzer, and G. Guenette, "Modeling for control of rotating stall," Automatica, vol. 30, no. 9, pp. 1357-1373, 1994.

[23] C. M. van Schalkwyk, J. D. Paduano, E. M. Greitzer, and A. H. Epstein, "Active stabilization of axial compressors with circumferential inlet distortion," Journal of Turbomachinery, vol. 120, pp. 431-439, 1998.

[24] J. P. Longley, "A review of non-steady flow models for compressor stability," in International Gas Turbine and Aero-engine Congress and Exposition, 1993. ASME 93-GT-17.

[25] J. M. Haynes, G. J. Hendricks, and A. H. Epstein, "Active stabilization of rotating stall in a three-stage axial compressor," ASME Journal of Turbomachinery, vol. 116, pp. 226-239, 1994.

[26] K. K. Ahuja and R. H. Burrin, "Control of flow separation by sound," in AIAA Aeroacoustics Conference, 1984. AIAA 84-2298.

FEDSM2003-45579

FLOW SEPARATION WITHIN THE ENGINE INLET OF AN UNINHABITED COMBAT AIR VEHICLE (UCAV)

Michael J. Brear
Department of Mechanical and
Manufacturing Engineering,
University of Melbourne, Australia,
mjbrear@unimelb.edu.au

Zachary Warfield
Structures and Configuration Group
Mechanical Engineering Section
Jet Propulsion Laboratory

John F. Mangus
Integrated Systems
Northrop Grumman Corporation

Cpt. Steve Braddom
Department of Civil & Mechanical
Engineering, West Point

James D. Paduano
Gas Turbine Laboratory
Massachusetts Institute of Technology

Jeffry S. Philhower
Integrated Systems
Northrop Grumman Corporation

ABSTRACT

This paper discusses the structure of the flow within the engine inlet of an uninhabited combat air vehicle (UCAV). The UCAV features a top-mounted, serpentine inlet leading to an engine buried within the fuselage. The performance of the inlet is found to depend strongly on a flow separation that occurs within the inlet. Both the time-averaged and the unsteady structure of this separation is studied, and an argument relating the inlet performance to the behaviour of this separation is suggested.

The results presented in this paper also suggest that there are considerable aerodynamic limitations to further shortening or narrowing of the inlet. Since there are substantial, system level benefits from using a smaller inlet, the case for separated flow control therefore appears clear.

INTRODUCTION

The engine inlets of uninhabited combat air vehicles (UCAV's) are often serpentine. Furthermore, the structural weight of UCAV's is minimized by making the inlet as short and as narrow as possible. If it is necessary to maintain the serpentine inlet design, reduced inlet length implies greater flow turning. A narrow inlet requires flow that is close to choking at peak massflow conditions. The combination of aggressive flow tuning and high subsonic Mach numbers makes strong adverse pressure gradients unavoidable. As previous investigations have found, the flow within serpentine inlets therefore often separates, leading to reduced inlet pressure recovery and increased unsteadiness within the inlet [1-3].

Of course, reduced inlet pressure recovery and increased inlet unsteadiness cause a deterioration in the performance of the propulsion system. The mechanisms by which this occurs are numerous and complex. Most obviously, the specific thrust and specific fuel consumption are related to the inlet pressure recovery. However, distortions generated within the inlet also adversely affect the performance of the engine, primarily in terms of reduced compressor efficiency and reduced stall/surge margin [4].

This paper therefore presents a study of the mechanisms that determine reduced pressure recovery and increased unsteadiness within a UCAV inlet during cruise. At this flight condition, the flow entering the inlet has a uniform stagnation pressure and does not experience lip separations and other phenomena characteristic of take-off, landing and maneuvering. As such, any deterioration of the flow that enters the compressor is the result of phenomena that are internal to the inlet. Specifically, the inlet performance is related to the detailed structure of a flow separation. Both the steady and unsteady structure of this separation is studied using experimental and computational methods. From these results, it is then suggested that further shortening of the inlet can only be achieved with the use of separated flow control.

NOMENCLATURE

AIP	aerodynamic interface plane (fan face)
$\dot{m}$	massflow rate (lb/s)
Ma_∞	flight Mach number
P_s	static pressure (Pa)
P_t	stagnation pressure (Pa)
P_∞	freestream stagnation pressure (Pa)
Re_{AIP}	Reynolds number based on AIP diameter
x_{1-3}	cartesian axes
π_d	area averaged inlet pressure recovery

EXPERIMENTAL METHODS

All experiments presented in this paper were performed at the Gas Turbine Laboratory, Massachusetts Institute of Technology. A one sixth scale model of a UCAV inlet formed

the entrance to an open loop system driven by a 1 MW De Laval compressor (Figure 1). A 'bellmouth' contraction was placed upstream of the inlet so that the smooth inlet flow of cruise conditions was simulated on the stationary rig i.e. the lip separations and other phenomena that are characteristic of take-off, landing and maneuvering were avoided. An 'instument can' which contained a rake of 40 stagnation pressure probes (either steady or unsteady) was located downstream of the inlet. The layout of these probes complied with 'ARP 1420' [4] such that an average of the stagnation pressures read by the probes was the area averaged stagnation pressure at the AIP. The location of the probe rake represented the entrance to the engine (the fan face) and is referred to as the aerodynamic interface plane (AIP). The inlet massflow rate was controlled with a translating 'plug' that acted as a throttle. Flight representative inlet Mach numbers were achieved during the experiments (Table 1). Of course, inlet Reynolds number similarity could not be achieved due to the scaling of the inlet. Further details of all experimental methods employed are contained in [5].

case	alt. (kft)	Ma_∞	Re_{AIP} $(.10^6)$	$\dot{m}$ (lb/s)
full scale	35	0.8	7.63	111.5
model scale	0	0.0	1.28	3.13

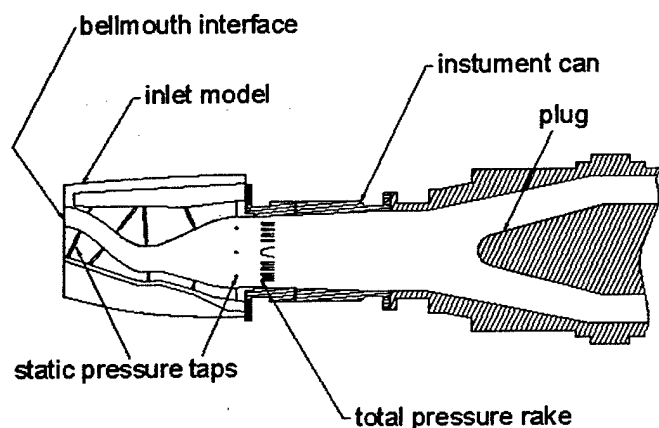**Table 1: Parameters at full scale and model scale**

Figure 1: Cross-section of experimental rig

Steady pressure measurements were taken with static pressure taps and pitot tubes that were connected by pneumatic tubing to a 10 psi Scanivalve differential pressure transducer. Unsteady stagnation pressure measurements at the AIP were performed with 5 psi Kulite unsteady pressure transducers that were connected to strain gauge conditioning amplifiers from Measurements Group, Inc. Figure 9c shows the location of a surface mounted hot film sensor that was placed within the separated region. This was a SENFLEX SF9902 single element shear stress sensor, and was controlled by a DANTEC constant temperature anemometer bridge. Both the unsteady pressure and hot film measurements were logged at a frequency of 20kHz.

Oil and dye flow visualisation was used to produce portraits of the limiting streamline structure within the inlet. This technique used a thick, black mixture of silicon oil and powdered charcoal painted uniformly over the inner surface of the laboratory scale inlet. The model was then run at cruise

representative Mach numbers, and the limiting surface patterns shown in this paper arose after roughly ten minutes of operation. The surface flow visualisation results presented in this paper used an inlet massflow rate of 3.6 lb/s, rather than the design massflow rate of 3.13 lb/s (Table 1). This was because the higher massflow rate gave clearer results within the separated region. It is emphasised, however, that the *structure* of the separated region appeared to be the same at both of these massflow rates.

NUMERICAL METHODS

The numerical predictions presented in this paper used a proprietary version of the NASA CNS program. This solver used a diagonalised Beam Warming solution algorithm with a finite volume spatial discretisation. For the current work, a four block grid system with patched and overset grid boundaries was utilized. The grid was generated for a complete half model of the full scale aircraft and its farfield, and consisted of over one million nodes. The numerical prediction was performed at the full scale cruise condition given in Table 1, meaning that the Reynolds numbers of the predictions were roughly six times the equivalent Reynolds number of the model because of the scale difference. Possible consequences of this are discussed in this paper. The results presented in this paper used an inlet modeled with 462,429 nodes, although higher resolution grids were also used in other cases to establish grid independence. All of the runs utilized local time stepping and a $K - \Omega$ turbulence model.

DISCUSSION

Inlet pressure recovery and flow at the AIP

Figure 2 shows the area averaged inlet pressure recovery versus the inlet massflow rate. The inlet pressure recovery is reasonable at the design massflow rate of 3.13 lb/s (Table 1), although it is roughly two percent below the pressure recovery of current, civil aircraft engine inlets cruising at similar flight conditions [1]. The lower inlet pressure recovery is of course due to the complex, serpentine geometry of the UCAV inlet. Excluding any form of separation within the inlet (which will serve only to further reduce the inlet pressure recovery), its considerable length compared to a typical civil inlet designs will inevitably cause reduced inlet pressure recovery through the losses generated in the inlet boundary layers.

Figure 2 also shows that the inlet pressure recovery decreases as the massflow rate is increased above design conditions. This is not expected to be Reynolds number related since the Reynolds number is increasing with increased massflow rate. In most high Reynolds number flows, increased Reynolds number will tend to reduce the thickness of the boundary layers [6], thereby increasing the inlet pressure recovery. Instead, the decrease in inlet pressure recovery is expected to be a Mach number effect. This is thought to be analogous to the increase in the drag of an airfoil at a fixed angle of attack, but with a subsonic, freestream Mach number increasing towards unity. In such cases, the severity of the adverse pressure gradient downstream of the point of peak velocity typically increases with increased freestream Mach number, causing the boundary layers to thicken and to even separate. Higher levels of aerodynamic loss are therefore created [7]. A similar argument appears reasonable in the present study, since the choking of the inlet must occur at some

massflow rate. Indeed, it is argued that a separation within the inlet is a significant contributor to this fall in the inlet pressure recovery, and this separation occurs immediately downstream of the inlet throat.
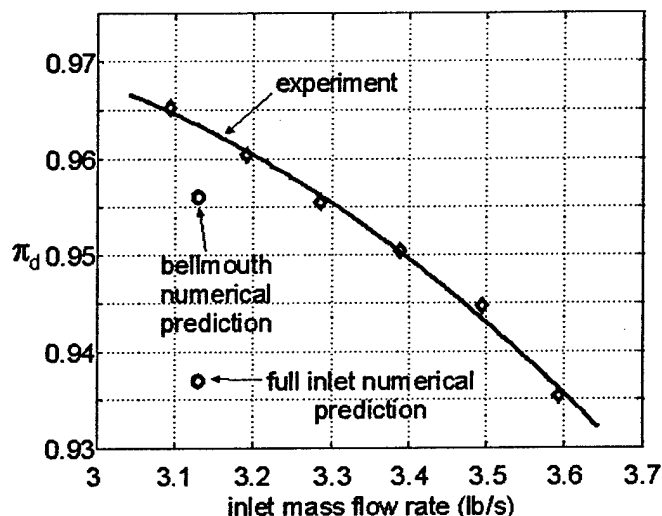

Figure 2: Measured and predicted π_d as a function of the scaled inlet massflow

Further understanding of the origins of the inlet loss can be obtained from contour plots of non-dimensional stagnation pressure at the AIP. As Figure 3a shows, the stagnation pressure contours at low massflow rate are reasonably uniform, although there are relatively minor deficits at the top and bottom of the AIP. However, Figure 3b shows that significant deficits in stagnation pressure occur at the AIP's top and bottom at the higher massflow rate. Massflow rates between those shown in Figure 3a&b give intermediate stagnation pressure portraits. These results show that the stagnation pressure deficits at the top and bottom of the AIP are responsible for the variations in inlet pressure recovery shown in Figure 2.
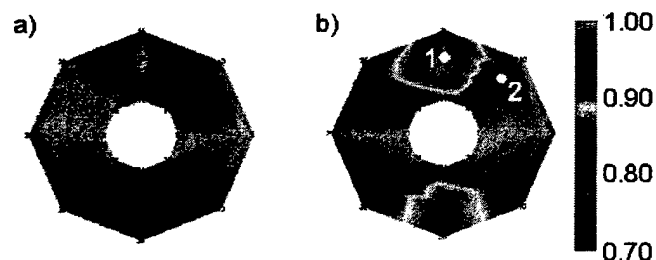

Figure 3: Contours of P_t/P_∞ at the AIP from experiment for a) low massflow rate (2.9 lb/s) and b) design massflow rate (3.6 lb/s), showing the location of the unsteady, stagnation pressure probes 1 and 2

The numerical prediction of the non-dimensional stagnation pressure contours at the AIP appears to compare favorably with experiment, although it is emphasised that the experimental result in Figure 3b is at a higher scaled massflow rate than the predicted result in Figure 4b. Like Figure 3b, Figure 4b also shows the regions of stagnation pressure deficit at the top and bottom of the AIP, although the resolution of the

predicted flow is of course much better since the number of stagnation pressure probes in experiment was limited to 40. Regions of stagnation pressure loss are also evident on the sides of the AIP. These are not seen in the experiments (Figure 3b) because the stagnation pressure probes were not close enough to the inlet walls.
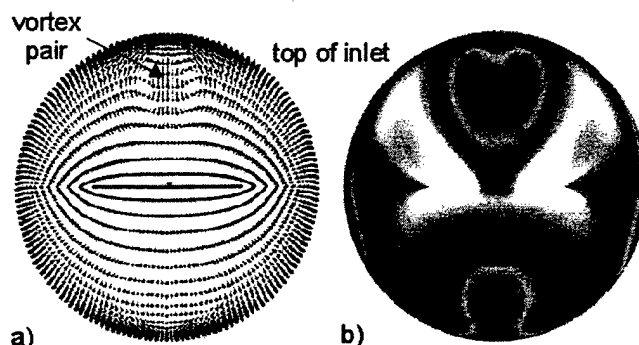

Figure 4: Predicted a) secondary flow vectors and b) contours of P_t/P_∞ (see Figure 3 for scale) at the AIP

The qualitative similarity between the results at different scaled massflow rates in Figure 3b and Figure 4b can be further explained by reference to Figure 2. As stated earlier, the numerical predictions were performed for the full aircraft, whereas experiments used a bellmouth contraction to simulate cruise conditions on a stationary rig. Thus, the predicted stagnation pressure distribution at the AIP includes the boundary layer loss created upstream of the inlet. However, Figure 2 shows that the predicted inlet pressure recovery at the design massflow rate of 3.13lb/s in Figure 4b is very similar to that measured at 3.6lb/s in Figure 3b. Figure 2 also shows that equivalent numerical predictions with the bellmouth inlet resulted in an inlet pressure recovery that is roughly 2% greater than the full aircraft predictions, and these are in better agreement with the experimental results at the same massflow rate. Thus, the similarity in the inlet pressure recoveries in Figure 3b and Figure 4b is partially because the increased massflow condition of Figure 3b gives a similar drop in the pressure recovery to that caused by the inclusion of the upstream boundary layers. The bellmouth and full aircraft predictions in Figure 2 nonetheless revealed the same inlet flow structure. Specifically, the size of a separation on the top surface of the inlet was the same in both sets of numerical predictions.

Figure 4b also shows that the deficit in the stagnation pressure at the top of the inlet has a lobed appearance. Examination of the secondary flow vectors (which are defined as perpendicular to the axial direction) in Figure 4a reveals a related feature. A pair of counter-rotating vortices exist within the region occupied by the stagnation pressure deficit in Figure 4a. It is also noted, however, that the secondary flow associated with the bottom deficit in stagnation pressure does not appear to be as strongly vortical. Nonetheless, close examination of this region also shows a pair of weak, counter-rotating vortices. Later results suggest that the origins of the top and bottom vortex pairs are different.

3

Overall inlet flow

Figure 5 shows an overall view of the predicted flow within the inlet during cruise. The inlet lip is serrated, which was removed in the experiments and replaced with the bellmouth contraction to avoid gross separation at static freestream conditions. However, at the cruise Mach number of 0.8, Figure 5 shows that the streamlines are roughly parallel at the inlet lip. These streamlines have become bundled at the top and bottom of the inlet by the time the flow has reached the AIP. In keeping with Figure 4a, the streamlines at the top of the inlet exhibit a relatively strong swirling motion immediately upstream of the AIP, although this does not appear to be the case further towards the inlet lip. Thus, this vortical flow at the top of the inlet appears confined to the region immediately before the AIP. As is argued in this paper, this motion primarily results from the flow separating within the latter part of the inlet. This separation is caused by a strong adverse pressure gradient that can also be inferred from Figure 5 and is shown more clearly in Figure 6.
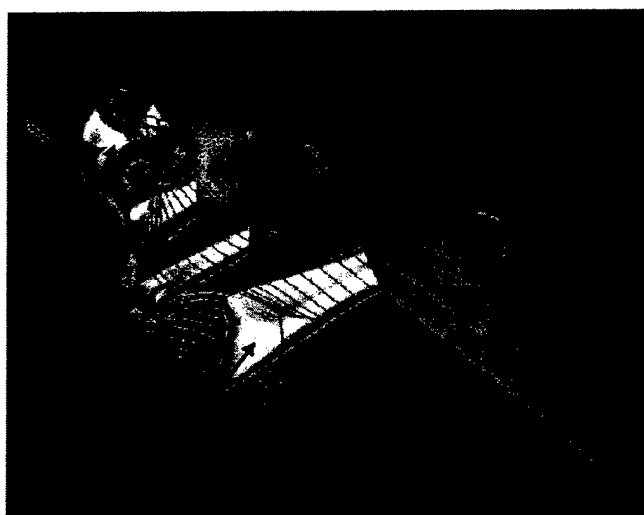

Figure 5: Computed inlet flow showing contours of P_t/P_∞ at fixed axial locations (see Figure 7 for scale) and P_s/P_∞ on the inlet surface

Figure 5 may also suggest that the pair of weak, counter-rotating vortices that occur at the bottom of the AIP originate further towards the inlet lip. Surface flow visualisation of the lower surface of the inlet in Figure 9a supports this result by showing that separation does not occur immediately upstream of the AIP, as is the case for the top surface of the inlet. Instead, this visualisation shows some secondary flow further towards the inlet lip, in keeping with the behaviour of the lower surface streamlines in Figure 5. It is therefore thought that the weak vortex pair at the bottom of the AIP originates from the bottom inlet surface closer to the inlet lip.

Centerplane flow

Figure 6 shows the predicted surface static pressure along the centerline of the inlet's top surface. It is clear that there is a strong favorable pressure gradient along most of the centerline from the inlet lip to roughly halfway along the inlet. The minimum in static pressure represents the inlet throat, downstream of which is a strong adverse pressure gradient and

then two local minima in static pressure. These local minima could most likely be removed with more careful design, although the requirement of compressor inlet Mach numbers of between 0.5 and 0.6 inevitably means that an adverse pressure gradient must exist downstream of the inlet throat if the flow at the throat is close to choking. Since there are strong system level incentives for maximising the inlet throat Mach number, strong adverse pressure gradients within the last part of the inlet are always expected to be the case in practice. As is shown in this paper, the separation of interest exists downstream of the second local minimum in surface static pressure.
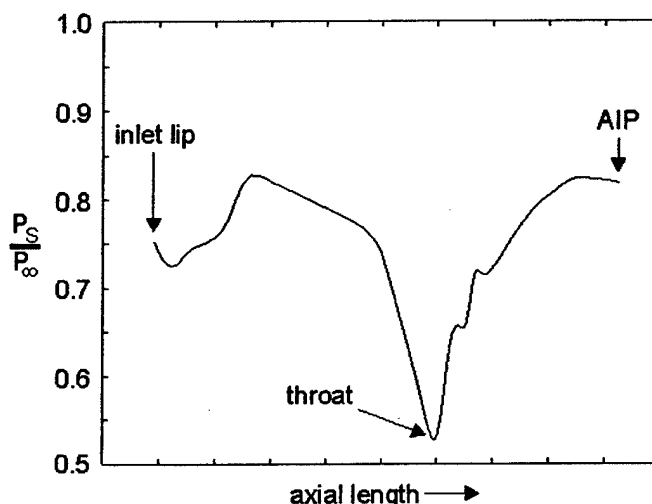

Figure 6: Predicted static pressure along the top surface of the inlet

The centerplane Mach number contours that correspond to this surface static pressure distribution are shown in Figure 7a. The inlet throat is apparent, and appears to be close to choking. Importantly, the Mach number is very low nearer the top and bottom inlet surfaces downstream of the inlet throat, which is the region that the inlet broadens to the AIP diameter. This is particularly marked on the top of the inlet, where flow separation is shown to occur.

Contours of stagnation pressure on the centerplane show the aerodynamic loss associated with this region of low Mach number flow (Figure 7b). Up to the inlet throat, the strongly favorable pressure gradient along the top surface causes the surface flow along the centerplane to be characterised by relatively thin, *attached* boundary layers. However, a large region of low stagnation pressure occurs downstream of the inlet throat. This compares to the loss free flow in the middle of the centerplane, which does not extend to the AIP since the two large lobes of low stagnation pressure shown earlier in Figure 3b and Figure 4b eventually coalescence. It is therefore reasonable to suggest that a significant proportion of the loss observed at the AIP originates within this last section of the inlet, where the adverse pressure gradient has been shown to be strong, and the flow is later shown to separate.

Figure 6 and Figure 7 also suggest that further modifications to the inlet design will have important consequences. The weight and drag of the aircraft can be minimised in two ways: by either shortening the inlet or making the inlet narrower. However, a given engine with a specified inlet Mach number of between 0.5 and 0.6 provides

4   Copyright © 2003 by ASME

the downstream boundary condition to the inlet flow. If it is necessary to maintain a serpentine inlet design, reduced inlet length necessarily implies more aggressive flow turning. Once again invoking the analogy with a single airfoil at a now constant freestream Mach number but with an increasing angle of attack, increased flow turning will increase the peak Mach numbers within the inlet. Similarly, continuity requires that peak inlet Mach numbers will be increased if the inlet is made narrower. Thus, shortening or narrowing the inlet have the same qualitative effect. Both will increase the peak Mach numbers within the inlet, whilst a given choice of engine will require that the flow at the AIP is maintained at roughly the same Mach number. The intensity of the adverse pressure gradient downstream of the inlet throat will therefore inevitably be increased, causing reduced inlet pressure recovery and, as is suggested in the present case, stronger separation and higher levels of its associated inlet unsteadiness.
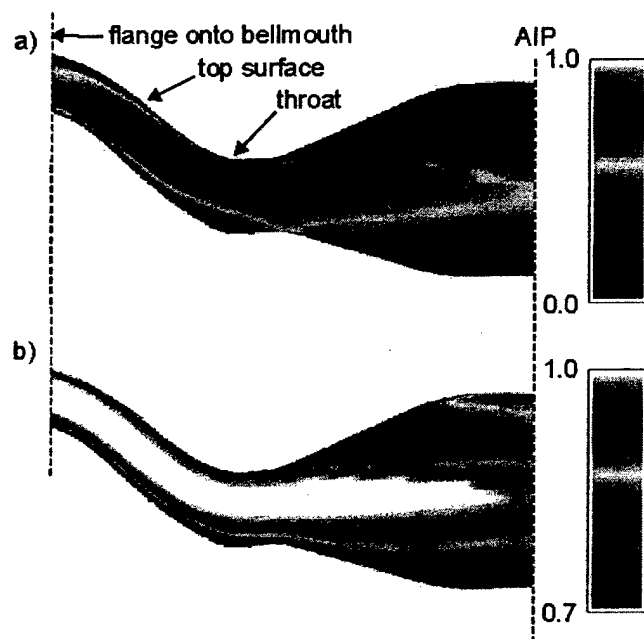

Figure 7: Predicted contours of a) Mach number and b) P_t/P_∞ along the center-plane of the inlet

Separated flow structure
The predicted velocity vectors within the last section of the inlet reveal the structure of the separation. Figure 8a shows a region of reversed flow near the top wall on the centerplane, with the estimated dividing streamlines shown in red. Figure 8b shows the limiting surface flow on the top surface of the inlet. Four stagnation points are visible: two foci (F) and two saddles (S). The dashed lines originating from the two foci represent the approximate location of two vortices that extend away from the surface and downstream to the AIP. As discussed earlier, the swirling streamlines associated with these vortices are visible near the top of the inlet in Figure 5.

Figure 9b&c shows that the numerical predictions and experiments give the same flow topology along the top of the inlet, even though the size of the separation is significantly larger in experiment. Experiments show that the flow along the entire top surface is attached up to the inlet throat. However,

just downstream of the inlet throat the flow becomes strongly three dimensional and, in keeping with the limiting streamline pattern shown in Figure 8b, the inferred surface topology in Figure 9b also shows two foci and two saddles. Perry & Chong [8] call a separation with this limiting streamline topology an 'owl face of the first kind'. Similar *predicted* flow structures in serpentine engine inlets have been reported in Seddon and Goldsmith [1] and Anderson et al [2], although this paper is thought to be the first that verifies the existence of this structure experimentally.
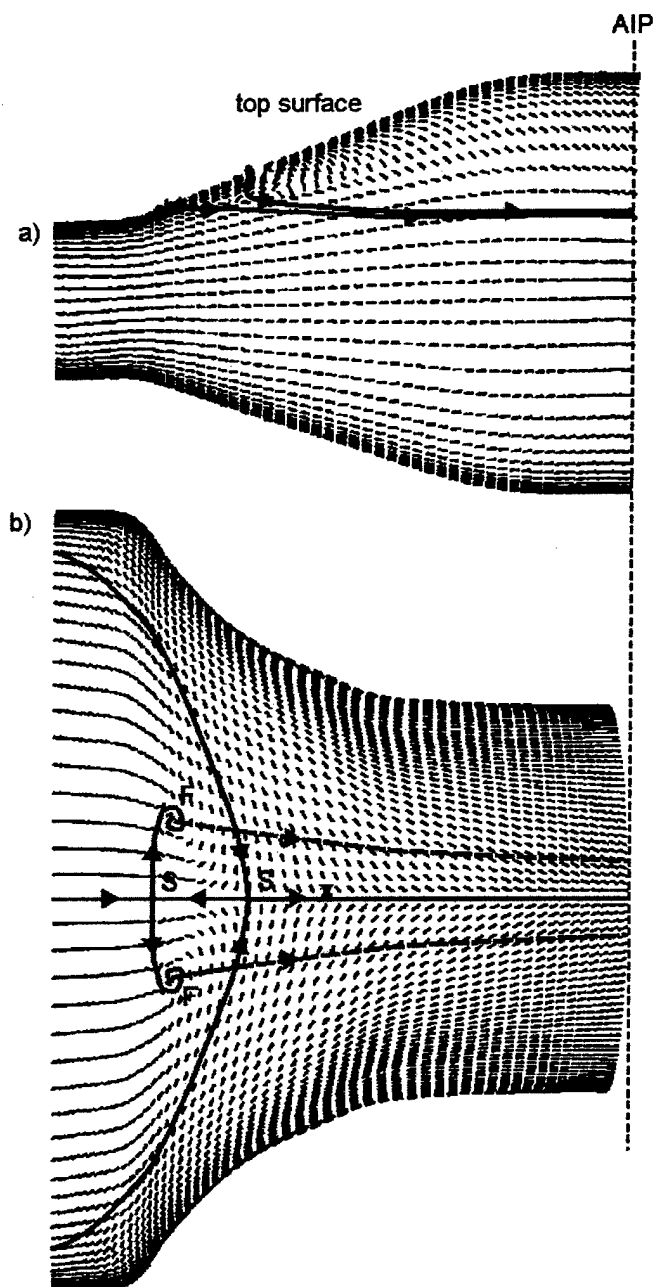

Figure 8: Predicted velocity vectors and inferred flow topology a) along the inlet center-plane and b) near the top surface of the inlet
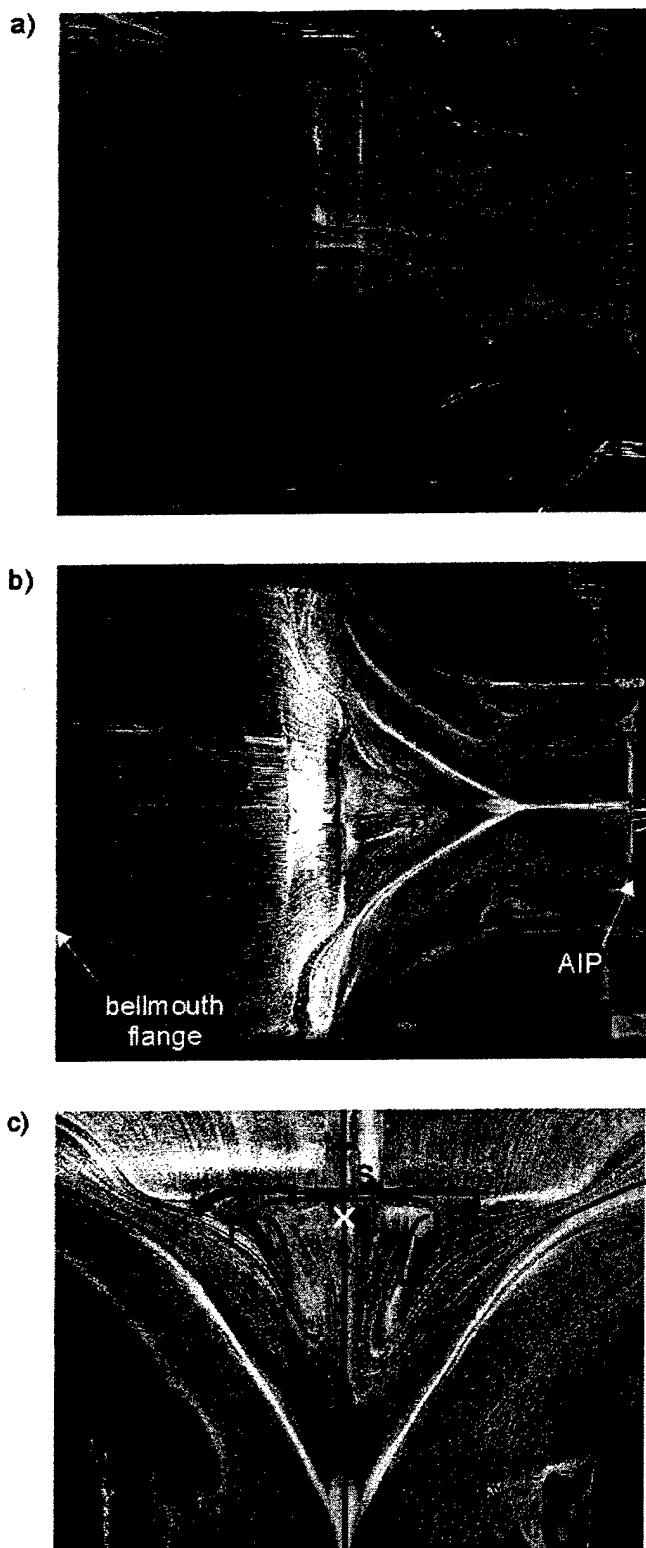
Figure 9: Experimental surface flow visualisation showing a) the bottom and b) the top surfaces of the inlet and c) the top surface's separated region with inferred flow topology (lines) and the location of the hot-film sensor (white cross)

A clearer picture of this basic separation structure is shown in Figure 10, where the vortex pair that extends downstream is seen to originate at the two foci. Thus, the two vortices that are observed at the top of the AIP in Figure 4a appear to originate at the two foci within the separated region. This is consistent with the swirling streamline patterns near the top surface in the last section of the inlet in Figure 5. It is emphasized that this structure is not a typical 'separation bubble' such as that classified by Horton [9]: it is not characterized by a reattachment point and recirculating flow. Nonetheless, the mean, surface normal velocity profiles throughout the separated region must be inflectional. In keeping with the many other inviscidly unstable shear layers such as mixing layers and more usual 'separation bubbles', it is therefore expected that the separation will be strongly unsteady and may respond to freestream disturbances [10].
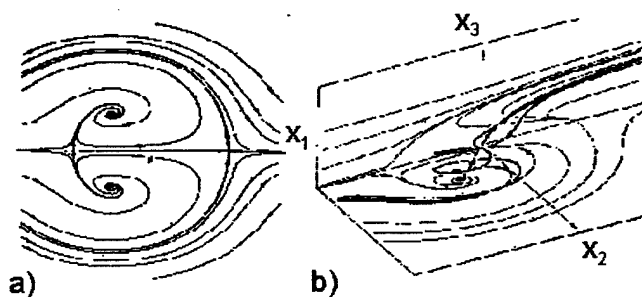

Figure 10: An 'owl-face of the first kind' [8]

The differing size of the separated regions in experiment and the numerical prediction is not surprising. The numerical prediction was performed at a higher Reynolds number and lower Mach number than the experimental flow visualisations in Figure 9, and the numerical prediction is a steady, Reynolds averaged solution of what is expected to be a strongly unsteady flow. Reynolds averaged turbulence models should not be expected to produce accurate predictions of separated flows but, despite this lack of rigour, they can give reasonable results [11]. The present set of results bears this out.

Importantly, the similarity between the predicted and experimental separated flow structures, and their pressure recoveries (Figure 2), suggests that the separation has a significant impact on the inlet pressure recovery. A comparison of Figure 8a and Figure 7b shows that the separation is also a region of considerable deficit in stagnation pressure. This compares to the attached boundary layers upstream of the separation in Figure 7b, where the stagnation pressure is significantly higher. Thus, large stagnation pressure losses appear to be produced within the separated region, and this 'high loss' fluid should then convect to the AIP.

The creation of low stagnation pressure within separated regions is often observed in steady, Reynolds averaged numerical predictions of separated flows [12]. As was found in the present numerical prediction, the turbulence model can predict levels of turbulent viscosity within the separated region that can be several orders of magnitude greater than the laminar viscosity. As Brear et al [12] show, the entropy generation rate per unit volume is directly proportional to the turbulent viscosity, and the turbulence model is therefore predicting that the primary sources of loss generation within the separation are the Reynolds stresses. Laminar stresses are less significant.

6   Copyright © 2003 by ASME

Because the numerical prediction is steady, increased entropy is manifested as reduced stagnation pressure. Furthermore, Brear [13] showed that the Reynolds stresses within numerous separated flows can be an order of magnitude higher than those that occur in attached boundary layers. Thus, the numerical prediction of very high turbulent viscosity is physical, even though the absolute values of predicted turbulent viscosity are not expected to be accurate. It is therefore perhaps surprising that the predicted and measured inlet pressure recoveries agree as closely as they do (Figure 2), and this serves to further the utility of steady, Reynolds averaged numerical predictions despite the lack of rigour of applying them to separated flows.

Large Reynolds stresses within separated flows are not surprising, given that such flows can feature large, coherent structures that often have some periodicity [10,11,14]. These structures can be long-lived and convect downstream for a considerable distance [15]. Whilst the Reynolds stresses within the separated region were not measured in the present investigation, coherent structures that either pass through the separation or are created within it are observed to convect to the AIP. As Figure 11a shows, there is significant cross correlation between the surface mounted, shear stress sensor within the separated region (Figure 9c) and the unsteady stagnation pressure sensor 1 located close to the center of the stagnation pressure deficit at the AIP (Figure 3b). Figure 11a shows that there is a lag of approximately 1ms between events occurring at probe 1 at the AIP and those occurring within the separation. This lag is similar to the calculated convection time from the separation point to the AIP of 0.75ms [5, 16] and, since the shear stress sensor cannot measure acoustic fluctuations, this correlation must involve some form of flow structure. Futhermore, Figure 11a also shows that this structure has a dominant frequency of approximately 500Hz. Figure 11b also shows this characteristic frequency, as well as showing that the structures arriving at the AIP have significant spatial extent because there is no lag between probes 1 and 2. Figure 11 is therefore strong evidence for suggesting that the separation has characteristics that are typical of separated flows. It appears that the separation creates large structures with a characteristic frequency, and that these structures convect downstream to the AIP.

CONCLUSIONS

This paper presented an experimental and computational study of the engine inlet on an uninhabited combat air vehicle (UCAV) operating at cruise conditions. At this flight condition, the flow entering the inlet had a uniform stagnation pressure and did not experience lip separations and other phenomena that are characteristic of take-off, landing and maneuvering. As such, any deterioration of the flow that enters the compressor is the result of phenomena that are internal to the inlet.

A separation on the top surface of the inlet appeared to be a significant contributor to reduced inlet pressure recovery and increased inlet unsteadiness. The time-averaged structure of this separation was identified by reference to a more fundamental study, and featured two vortices that extended downstream to the fan face. Furthermore, measurements suggested that the separation created large, unsteady structures that were observed at the fan face. The numerical predictions also indirectly suggested that this unsteady phenomenon caused large Reynolds stresses within the separated region that in turn

generated significant loss. Thus, the separation seemed to be the single cause of both a reduction in inlet pressure recovery and an increase in inlet unsteadiness by the same basic mechanism.
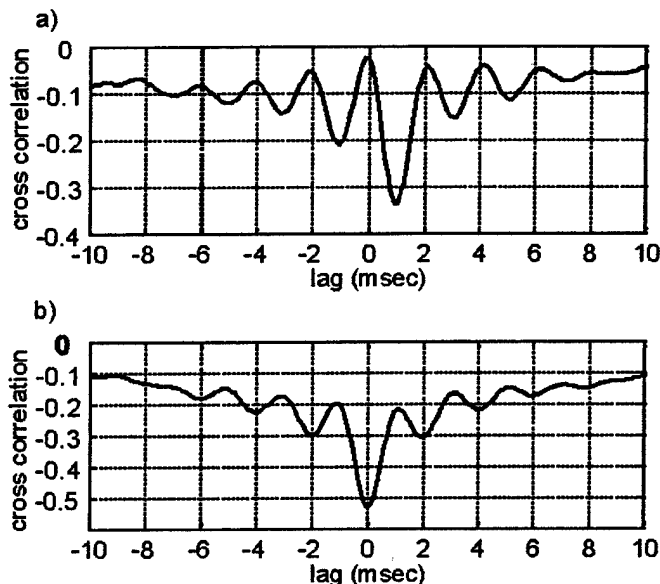
a)

b)

Figure 11: Cross correlations at design massflow rate between a) the unsteady stagnation pressure probe 1 at the AIP in Figure 3b and the hot-film sensor located at X in Figure 9 and b) the two unsteady stagnation pressure probes at the AIP in Figure 3b

This unsteady behaviour of the separation has important consequences for inlet design. An increase in the inlet Mach number or a reduction in the length of the inlet should increase the intensity of the adverse pressure gradients within the inlet. Stronger adverse pressure gradients cause stronger separations, which should therefore lead to reduced pressure recovery and increased inlet unsteadiness. Thus, further reductions in the inlet length or width either requires that the designer accepts the reduced performance, or finds some means of decoupling the inlet performance from changes in the geometry. Since both the unsteadiness and the pressure recovery appear to be the result of phenomena that originate from a contained region, this inlet is therefore a clear candidate for the application of separated flow control.

REFERENCES
1. Seddon, J. & Goldsmith, E.L., 1999, "Intake aerodynamics", 2nd edition, AIAA education series, AIAA
2. Anderson, B.H., Miller, D.N., Yagle, P.J. & Truax, P.P., 1999, "A study of MEMS flow control for the management of engine face distortion in compact inlet systems", Proc. 3rd ASME/JSME Conference, San Francisco, ASME paper no. FEDSM99-6920
3. Ng, W. & Burdisso, R.A., 2001, "Active acoustic and flow control for aeropropulsion", 39th AIAA Aerospace

Sciences Meeting & Exhibit, Reno, AIAA paper no. AIAA 2001-0220

4. SAE Committee S-16, 1977, "ARP 1420 – Gas turbine engine inlet flow distortion guidelines"

5. Wafield, Z., 2001, "Active control of separation induced distortion in a scaled tactical aircraft inlet", M.S. Thesis, Massachusetts Institute of Technology

6. Schlichting, H., 1979, "Boundary layer theory", McGraw-Hill, New York

7. Abbott, I.H. & von Doenhoff, A.E., 1959, "Theory of wing sections", Dover, New York

8. Perry, A.E. & Chong, M.S., 1986, "A series expansion study of the Navier-Stokes equations with applications to three-dimensional separation patterns", Journal of Fluid Mechanics, vol. 173, pg. 207-223

9. Horton, H.P., 1969, "A semi-empirial theory for the growth and bursting of laminar separation bubbles", ARC current papers, no. 1073

10. Gad-el-Hak, M., 1990, "Control of low speed aerodynamics", AIAA Journal, vol. 28, no. 9, pg. 1537-1552

11. Lubcke, H., Schmidt, St., Rung, T., Thiele, F., 2001, "Comparison of LES and RANS in bluff-body flows", Journal of Wind Engineering and Industrial Aerodynamics, vol. 89, pg. 1471-1485

12. Brear, M.J., Hodson, H.P. & Harvey, N.W., 2002, "Pressure surface separations in low pressure turbines - part 2: interactions with the secondary flow", ASME Journal of Turbomachinery, vol. 124, pg. 402-409

13. Brear, M.J., 2000, "Pressure surface separations in low pressure turbines", Ph. D dissertation, Cambridge University

14. Brear, M.J., Hodson, H.P. & Harvey, N.W., 2002, "Pressure surface separations in low pressure turbines - part 1: midspan results", ASME Journal of Turbomachinery, vol. 124, pg. 393-401

15. Castro, I.P. & Epik, E., 1998, "Boundary layer development after a separated region", Journal of Fluid Mechanics, vol. 374, pg. 91-116

16. Braddom, S., 2002, "Design and Characterization of Robust Hot Film Sensors for Tactical Aircraft Inlets", M.S. Thesis, Massachusetts Institute of Technology